Limits of Permissible Damage in Strong-Post W-Beam Guardrail

Carolyn Elizabeth Hampton

Thesis submitted to the faculty of the Virginia Polytechnic Institute and State University in partial fulfillment of the requirements for the degree of

Master of Science
In
Biomedical Engineering

Hampton C. Gabler, Chair
Stefan M. Duma
Warren N. Hardy

April 24, 2009
Blacksburg, Virginia

Keywords: Strong-post, w-beam guardrail, simulation, LS-DYNA

Limits of Permissible Damage in
Strong-Post W-Beam Guardrail

Carolyn Elizabeth Hampton

Abstract

Crash tests of strong-post w-beam guardrail have focused entirely on the performance of new guardrail. The risk posed by minor damage modes, e.g. small deflections and missing posts, has never been evaluated. Using finite element models validated by real world crash tests, this study assessed the safety risk of crashes into guardrail with minor damage. The minor damage modes under consideration for this study were rail and post deflection, missing posts, rail flattening, and post/rail separation. Each of these damage modes was evaluated according to the testing protocols laid out in National Cooperative Highway Research Program (NCHRP) Report 350, test level 3. A number of minor damage modes were found to pose significant risks to vehicle occupants and should be repaired as soon as possible. In order of priority of repair, these modes are missing posts, rail and post deflection over 6", and rail flattening over 50%. Damage modes of less concern were rail and post deflections less than 6", rail only deflection up to 6", flattening less than 50%, and separation of the posts from rails. These recommendations were on the conservative side because preventing occupant injury was the highest priority of guardrail performance.

Guardrails with rail and post deflection posed a risk of vehicle vaulting due to lowered rail height and failure of the posts to separate from the rails. This risk would be even greater for guardrails embedded in soft soils, which allow for greater deflection. Guardrails with missing posts frequently resulted in snagging of the vehicle tire on the downstream posts, as well as large increases in the tension carried by the rails during impact. Flattened rails posed a risk of vehicle rollover as they provided a ramp-like surface which caused the side of the vehicle to move upward, greatly increasing the change of override. Flattening also occurs frequently with other damage modes. Pre-existing separation of posts from the rails was found to have very little effect on the crash outcome. Separation of the posts from the rails was desirable as it prevented failure modes that were observed for the rail and post deflection simulations while maintaining the post contributions to lateral strength of the guardrail.

Acknowledgments

I would like to acknowledge the contributions of the project sponsor, the National Academy of Sciences, as well as the Transportation Research Board (TRB) and the National Cooperative Highway Research Program (NCHRP) 22-23 project panel.

TABLE OF CONTENTS

LIST OF FIGURES

LIST OF TABLES

1. BACKGROUND

Strong-post w-beam guardrail is used extensively all over the United States as a roadside barrier system. It is the most widely used of the steel roadside barriers, being more prevalent alternative systems such as thrie-beam, weak-post, and three-cable. It is one of two types of guardrail that utilize the w-beam element, which is named for its distinctive "W" shape (the other type is weak-post guardrail). Strong-post guardrail comes in several varieties such as the systems shown below in Figure 1. A similar but different system that can be seen on roadsides is the strong post median barrier. The median barrier looks similar to guardrail, but the rails are present on both sides of the posts. However, median barriers are outside the scope of this study.

Figure 1: Examples of various types of strong-post w-beam guardrail systems. Steel post with plastic blockouts (top left), steel post with steel blockouts (top right), wood post and blockout (bottom left).

Strong-post w-beam guardrails are important safety features on roadways all across the country. Guardrail is typically placed in front of objects or surface conditions that could cause more injury and damage than the guardrail itself. The primary uses for guardrail are:

- Protecting bridge pillars, poles, trees, and buildings
- Preventing vehicle entry into ravines, ditches, and bodies of water
- Preventing vehicles from crossing into opposing traffic lanes

Constraints on guardrail design include maintaining the vehicle stability. The prevention of vehicle rollover has been of great concern due to the disproportionate rates of injury and death, especially for pickup trucks. It is also desirable, although not required, that the vehicle's exit angle be lower than the impact angle, to minimize the risk of the vehicle returning into the roadway where it would be at risk of being hit by other vehicles.

All guardrail systems are thoroughly crash tested to ensure that the guardrail itself presents minimal risks to the vehicle and vehicle occupants. The testing procedure and thresholds of acceptable performance are determined by a report called NCHRP 350. Guardrail for use must meet these requirements before it can be installed on roadways.

1.1 NCHRP 350 Test Criteria

In 1993, the National Cooperative Highway Research Program published "Report 350 – Recommended Procedures for the Safety Performance Evaluation of Highway Features [1]." This document provided updates to the original NCHRP Report 230 [2], which was released in the 1980s. Although this document provides guidelines for evaluating the performance of a wide range of safety barriers, this study was concerned primarily with the testing procedures regarding the strong-post w-beam guardrail.

NCHRP Report 350 laid out all of the vehicle and test requirements needed to demonstrate the safety of a guardrail system. The severity of the test conditions varied with the intended use of the guardrail, which was graded by levels between 1 and 5, with five being the most severe test condition. For example, guardrail destined for lower speed roadways needed only to pass the less stringent level 1 or 2 testing. However, guardrail intended for highway use must meet the test level 3 criteria.

NCHRP Report 350 listed general types of vehicles that were acceptable for use in a crash test. In general, the higher the test level, the heavier the test vehicle must be. Acceptable vehicles include the following:

- 820 kg small car, such as a Geo Metro
- 2000 kg pickup truck, such as a Chevrolet 2500 or GMC 2500
- 8,000 kg single unit truck, such as an U-Haul truck
- 36,000 kg tractor van or tractor truck

In tests reports, these vehicles are usually not referred to by the make and model, but by more general names such as 820C, 2000P, 8000S, and 36000T respectively. Testing vehicles by weight and class was beneficial because the vehicle fleet changes constantly and a model that was readily available in the 1990s (i.e. the Chevrolet 2500 pickup) may be difficult to obtain today.

NCHRP 350 test level 3 required that testing be performed with both the small car (820C) and the pickup truck (2000P). However, the test initial conditions were different for each vehicle. For a crash test with the small car, the initial conditions were 100 kph at an impact angle of 20 degrees. For the pickup truck, the initial speed was the same (100 kph) but the impact angle was slightly higher at 25 degrees.

Because of the more severe impact angle, as well as the higher center of gravity and lower front overhang, the crash test of the pickup truck was much more severe than that of the small car. Guardrail developed currently tends to focus on meeting the required safety criteria with the pickup truck, because it is uncommon for the less severe crash test of the car to fail when the pickup truck crash tests passes.

NCHRP 350 laid out a variety of measurable criteria with which the performance of the guardrail could be assessed. These criteria were divided into three categories, which were structural adequacy, occupant risk, and post impact vehicle trajectory. For guardrail, maintaining structural adequacy required that the guardrail redirect the vehicle without rupture. Similarly, the post-impact trajectory should not lead into nearby lanes of traffic.

The evaluation of occupant risk was the most detailed of the three criteria for guardrail crash tests. Despite the name, occupant risk was actually evaluated from measurements on the vehicle, because NCHRP 350 does not require that an instrumented crash test dummy be included for the crash test. Recommended and maximum thresholds for occupant impact velocity (OIV) and ridedown acceleration were provided for both the longitudinal and lateral directions. The recommended limit for OIV was 9 m/s, with a maximum of 12 m/s allowed. The ridedown acceleration was recommended to be 15 G or less but must be lower than 20 G. In addition, the integrity of the occupant compartment of the vehicle must remain intact. The procedures for the calculation of OIV and ridedown acceleration can be found in section 5.3 of Appendix A in NHCRP Report 350 [1].

1.2 History of Strong-Post W-Beam Guardrail

Before the 1990s, nearly all of the guardrail installed along roadways was the steel post, steel blockout type of strong-post w-beam guardrail, i.e. the G4(1S). This guardrail was tested according to the NCHRP 230 test criteria, which required testing with a small car and a large car, and was found to be acceptable for safely redirecting vehicles. When the new NCHRP 350 requirements were released, the all-steel w-beam guardrail was tested again with the 2000P pickup truck to ensure that the guardrail met the new standards. While the guardrail was able to redirect the pickup truck, the vehicle rolled over due to the impact [3].

To make the strong-post w-beam guardrail compliant with the new regulations, it was modified. The new system, called the modified G4(1S), replaced the old steel blockouts with larger wood blockouts [3]. Later tests also demonstrated the acceptability of using plastic blockouts as well. However, the failure of the old steel blockout guardrail system meant that there was an enormous length of guardrail that needed to be updated to the meet the new standards. To date, much of the highway guardrail has already been updated to meet the NCHRP 350 requirements, although the older all-steel guardrail still exists on roadways where compliance with lower test levels is required.

1.3 Guardrail Parts

The current modified G4(1S) strong-post w-beam guardrail system consistent of only a few basic parts. These parts are the post, rail, and blockouts. The part dimensions that are illustrated below were obtained from the AAHSTO Online Hardware Guide [4]. The AASHTO identifier for the guardrail system used in this study is SGR-04c.

The w-shaped rails that are used in the modified G4(1S) are shown in Figure 2. For this study, version A of the rail is used. These galvanized metal w-shaped sheets are 4130 mm long, 312 mm tall and 2.77 mm thick. Two rails can be held together using the 35 mm long button head splice bolts with the AASHTO designation FBB01. One or two rails can be connected to the posts using button head bolts (FBB02) which are 255 mm long. All bolts are 16 mm in diameter and are fastened with recessed hex nuts.

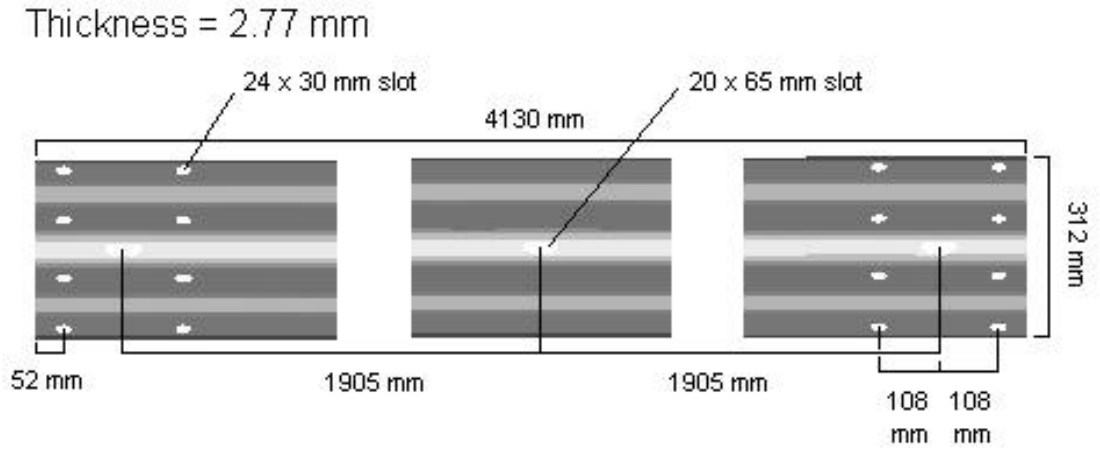

Figure 2: Part dimensions for rail RWM02a [4]

The posts of the guardrail used for this study are of the PWE01 designation. The posts are W150x3.5 structural I-beams that are 1,830 mm in length. Of this length, 1,100 mm is embedded into the soil. Although the drawing specifies only two locations for holes, guardrail in the field may have many more holes drilled, which does not affect the performance of the post. An optional rub rail can be added to the post via a hole just above the ground line, although this feature was not included in this study. A post drawing is provided for reference in Figure 3.

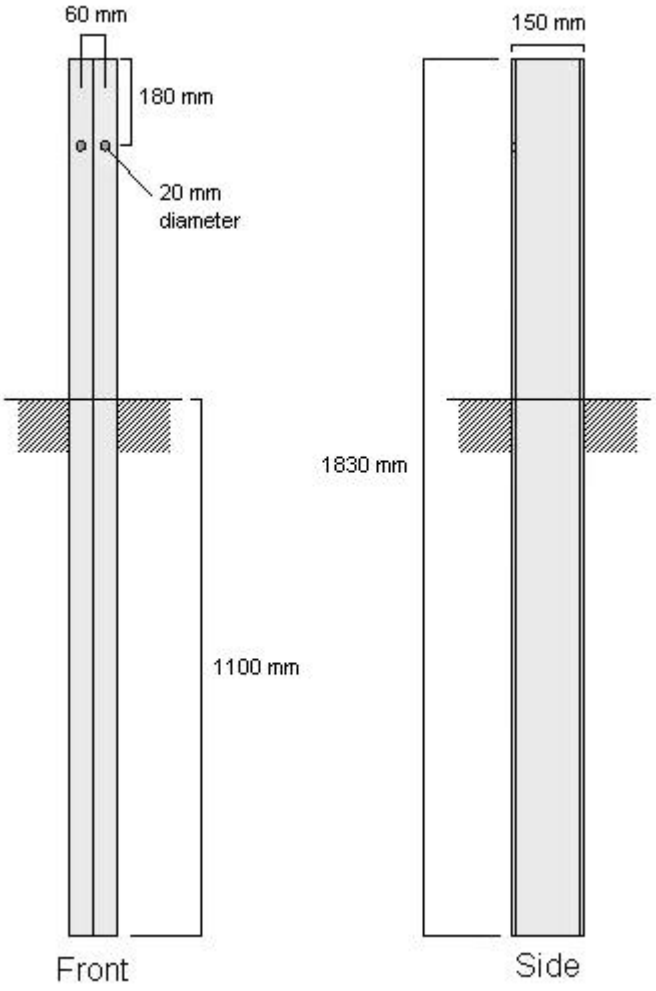

Figure 3: Part dimensions for post PWE01 [4]

The blockout, shown in Figure 4, is made of wood or plastic and is placed between the rails and post to provide spacing. The dimensions are 150 x 200 x 360 mm. The blockout used in the modified G4(1S) system corresponds to version B in the drawing, which differs from version A only in the location of the hole. When in use, the bolt that holds the rails and posts together passes through the holes in the blockouts. Blockouts are typically routed, with the lips fitting around the edges of the post, to prevent the blockouts from rotating around the bolt.

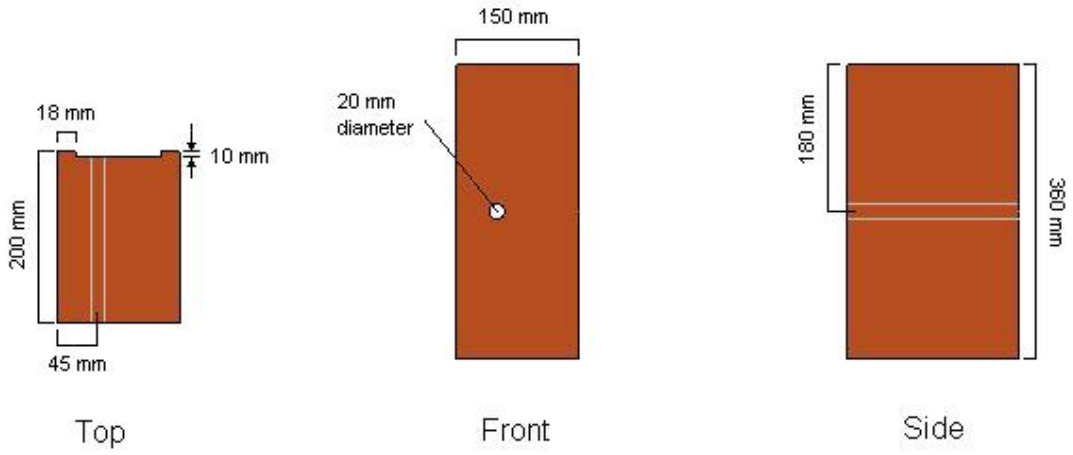

Figure 4: Part dimensions for blockout (PDB01a) [4]

1.4 Guardrail in the Field

Once a strong-post w-beam guardrail has been installed in the field, it typically receives little attention until it has been damaged and needs repair. Guardrail repair is performed by maintenance crews, who bring the new parts to the site of damage and perform the repair. There are a number of factors that affect the time needed to complete the repair, such as the distance between the location of the stored parts and the impact site, volume of traffic and traffic delays, and the existence of other, higher priority accidents. Although all of these factors are important, this study is focused on only one: the prioritization of repair.

2. OBJECTIVE

The objective of this study was to determine the limit of acceptable damage in strong-post w-beam guardrail. A variety of damage modes, with different extents of damage, will be evaluated according to the NCHRP test level 3 criteria. This evaluation will be performed not by crash tests, but by finite element models. The damage modes that are to be evaluated are shown in Table 1.

Table 1: Planned simulations of minor guardrail damage

Barrier	Vehicle	Damage Type	Damage Extent	Testing Criteria
Strong Post W-Beam (Steel post, Wood Blockout)	2000P	No damage	-	-
		Post/rail deflection (no post detachment)	3" lateral	6" Post/rail deflection
			6" lateral	
			9" lateral	
		Rail deflection	3" lateral	6" Rail deflection
			6" lateral	
		Rail Flattening	25% section width	Rail flattening ≥ 50% thickness
			50% section width	
		Post Detachment	1 post, 3"	Any post separated from rail
			2 posts, 3"	

For each type of damage, a recommendation will be developed based on the simulation results, as to whether the damage mode in question represents a significant risk to the safety of vehicle occupants. From these recommendations, a guideline for which damage modes need to be repaired first and which damage modes may not need to be repaired at all will be developed.

3. METHODS

3.1 Introduction

Ideally, the performance of strong-post w-beam systems with pre-existing damage would be determined from crash tests, but there are no crash tests to our knowledge that have been performed on damaged guardrail. Because crash tests were expensive, in terms of money and time, finite element modeling was used. The existing literature on tests of undamaged guardrail was still invaluable because of the need to have data against which the finite element models could be validated.

3.2 Strong-Post W-Beam Guardrail Model

The basic guardrail model used for this study is shown in Figure 7. This guardrail was made available online by the National Crash Analysis Center (NCAC) for use by researchers in crash modeling [6]. The model was designed to be used with the LS-DYNA finite element simulation software. The guardrail system was 53.6 meters (175.8 feet) in length from end to end. There were 29 posts in total, 21 of which were standard W150 x 13.5 (W6 x 9) steel I-beams. All rail sections were 3.81 meters (12.5 feet) long and 2.66 mm (0.1 in) thick, except at each end where the rail sections were double length. All of the rails mounted on posts 1 – 9 and 21 – 29 were coarsely meshed, whereas the rails mounted on posts 9 – 21 were finely meshed. Examples of the different meshing can be seen in Figure 5 and Figure 6. Because this was a modified G4(1S) system, routed plastic blockouts were used in the model rather than steel blockouts. Material properties for all the components came with the model. However, some

small studies on the effects of the rail and post material properties were conducted and detailed in Appendices A and B.

Figure 5: Coarsely meshed rail

Figure 6: Finely meshed rail

Both ends of the guardrail were supported by four wooden terminal posts leading to a breakaway cable terminal (BCT). All of the wooden posts were 140 mm wide, 190 mm deep, and 2200 mm long (5.5" x 7.5" x 7.2') and were embedded in steel foundation tubes, which were embedded into the ground. Each post also had a hole drilled through the center of the post just above the rim of the foundation tube. The model did not include any initial stresses in the tension cable or yoke.

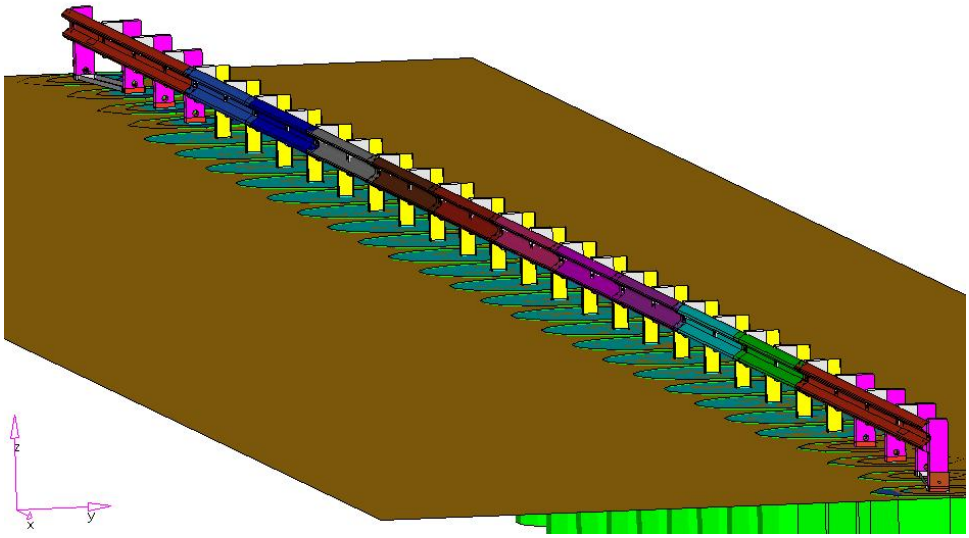

Figure 7: The NCAC strong-post w-beam guardrail model [6]

Near the area of contact, i.e. posts 9 – 21, the bolts that hold the rails and posts together were explicitly modeled as rigid bodies. Figure 8 shows the bolts used in the guardrail. The threads could not be modeled, so all of the bolts and nuts were held together with spring elements. Outside of the area of contact, consisting of posts 1 – 8 and 22 – 29, the connections were modeled as rigid nodal constraints. This simplification was made with the assumption that the connections outside of the area would experience minimal deformation and do not separate during crash tests.

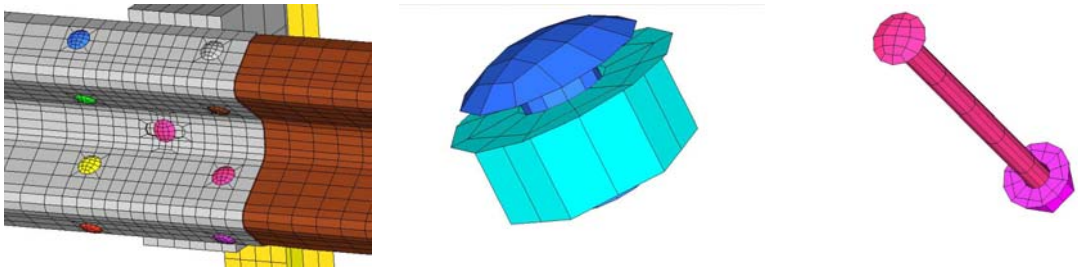

Figure 8: Examples of explicitly modeled connections, including a full splice joint (left), a single splice bolt and nut (middle) and a post bolt and nut (right).

The soil supporting the guardrail system was modeled as individual buckets around each post, rather than as a continuum body. Each steel post was embedded in a cylindrical volume of soil 2.1 meters (6.9 feet) deep and 1.6 meters (5.25 feet) in diameter. The soil buckets at the ends of the guardrail were slightly smaller with a 1.4 meter (4.6 feet) diameter and a coarser mesh.

3.3 Pickup Truck Model

To simulate a crash test, a model of a test vehicle matching the NCHRP 350 test criteria was also needed. The NCAC finite element library contained a number of vehicle models, including a detailed model of a 1994 Chevrolet 2500 pickup truck. This model was version 0.7

that was published to the online library on November 3, 2008. Like the strong-post w-beam guardrail model, this vehicle model was designed to be used with the LS-DYNA finite element solver. The vehicle is shown below in Figure 9. The vehicle model comes with an accelerometer located at the vehicle center of gravity that measured the acceleration of the vehicle in the local vehicle coordinate system. At the beginning of the simulation, the vehicle local coordinate system was exactly the same as the global system. However, as the vehicle was redirected the two systems diverged.

The detailed Chevrolet 2500 pickup model was selected for a number of reasons. First, the model was already subjected to a thorough validation effort to ensure the fidelity of the suspension of structural stiffness [7]. The detailed model also incorporates many interior parts that would not be present in a reduced model, such as the seating, steering column, bearings, fuel tank, and battery. The higher mesh density for the detailed pickup model also improved the accuracy and contact stability during simulation.

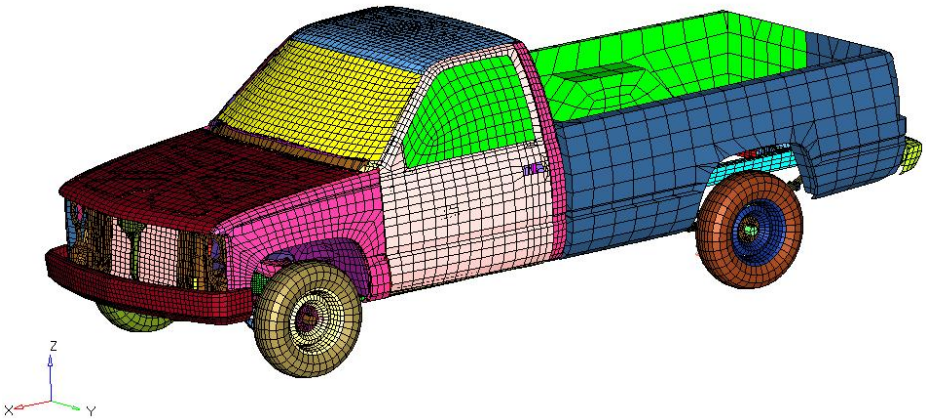

Figure 9: The NCAC finite element model of a 1994 Chevrolet 2500 pickup truck [6]

A limitation of the finite element model of the Chevrolet 2500 was that the dimensions of the vehicle were fixed. Most real pickup trucks have adjustable suspensions, which allow the front and rear bumper height of the vehicle to vary by as much as 100 mm. However, even

changes of a few centimeters in the relative height of the vehicle and guardrail have had been shown to have dramatic effects on the crash test results [8].

To correctly reproduce the results of a real crash, a finite element model matching the dimensions of the each individual test vehicle would be needed. For this study, there were three different crash tests that would be used to validate the full scale crash models. However, the unmodified pickup only matched the needed dimensions for one test. Thus, two alternative vehicle models were developed in which the bumper heights and weights were adjusted. The dimensions of each of these vehicle models are summarized in Table 2. The majority of the simulations in this study were performed with the vehicle matching the dimensions for the TTI crash test.

Table 2: Dimensions of finite element models of the Chevrolet 2500 pickup truck

Dimension	Original Chevrolet 2500 for TTI Test	Chevrolet 2500 for UNL Test	Chevrolet 2500 for MGA Test
Width	195.4 cm	195.4 cm	195.5 cm
Length	565.5 cm	565.4 cm	565.5 cm
Height	179.2 cm	182.9 cm	185.4 cm
F. Bumper height	63.6 cm	60.3 cm	68.1 cm
R. Bumper height	70.6 cm	79.9 cm	76.5 cm
Tire Diameter	73.0 cm	73.0 cm	73.0 cm
Weight	2013 kg	2011 kg	2014 kg

3.4 Combination of Guardrail and Vehicle Models

The vehicle and guardrail finite element models were combined by importing the vehicle model into guardrail model. All of the initial conditions were adjusted to match the values specified by NCHRP 350, i.e. the vehicle was given an initial velocity of 100 kph (roughly 60 mph) and the guardrail was rotated to create a 25 degree impact angle.

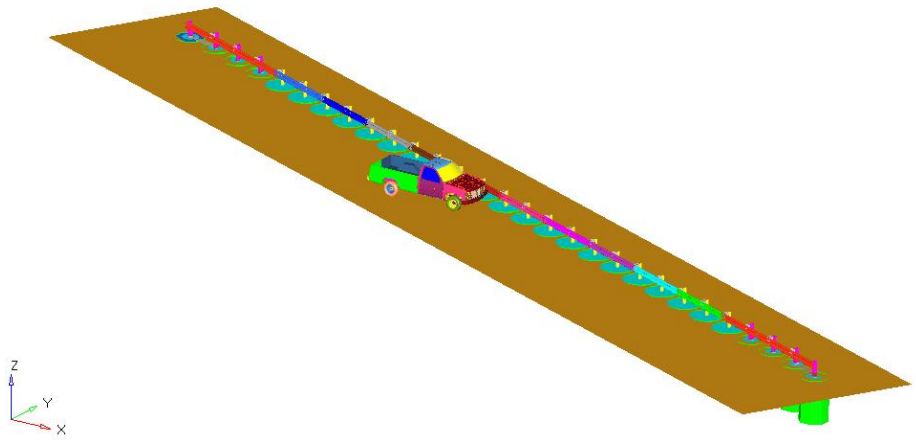

Figure 10: Combined guardrail and vehicle model

Because the models of the vehicle and guardrail were made available as separate objects, the only contacts already defined were those between the truck only and the guardrail only. Thus, it was necessary to develop a set of contact definitions to handle contact between the vehicle and the guardrail. The contact definitions added to simulate this contact are shown in Table 4. The definition of each of the modified parameters is discussed in Table 3. Multiple contact definitions were used to define contact between the same sets of parts to minimize the occurrence of contact instabilities which were the most common problems encountered in this study.

Table 3: LS-DYNA contact parameters and definitions

FS	Static coefficient of friction
FD	Dynamic coefficient of friction
DC	Decay coefficient between dynamic and static coefficient
PenChk	Flag to activate release of nodes and elements with large penetrations. This can prevent nodal snagging and unrealistic contact forces.
Soft	Flag to select penalty formulation (0), soft constraint formulation for parts of widely different stiffness (1), or pinball segment-based formulation (2)
SBOpt	Flag for contact options when using soft=2. A value of 1 activates only the edge-to-edge contact algorithm.
Depth	Search depth for automotive contact.

Table 4: LS-DYNA contact definitions between vehicle and guardrail

Parameter	**#1**	**#2**
Type	Automatic surface to surface	Nodes to surface
FS	0.000	0.200
FD	0.000	0.100
DC	0.000	0.001
PenChk	-	-
Soft	2	-
SBOpt	1	-
Depth	-	-

Because of the drastically different moduli between the vehicle tire and the sheet steel that makes up the guardrail and vehicle body, the front tire on the impact side was given its own contact definition as shown in Table 5. The greatest difficulty in modeling the tire impact was preventing elements in the tire from penetrating the free edges of the posts while also preventing unrealistic forces from developing that would lead to instabilities.

Table 5: LS-DYNA contact definitions between front, impact side tire and guardrail

	#3	#4	#5
Type	Automatic surface to surface	Automatic surface to surface	Nodes to surface
FS	0.000	0.000	0.000
FD	0.000	0.000	0.000
DC	0.000	-	0.000
PenChk	1	1	-
Soft	2	1	-
SBOpt	5	-	-
Depth	5	5	-

To combat this, the PenChk and Depth options on the contact card were activated. The PenChk field activated a penetration check to release any nodes that penetrate too deeply into a surface, preventing the development of unrealistic forces. Most contact definitions in LS-DYNA do not include edge-to-edge checking due to the computational cost. For situations where this type of contact would be expected (such as at the post edges), the Depth option can be used to

activate to edge-to-edge contact algorithm. A more detailed description of each of these fields is provided in the LS-DYNA keyword manual [9].

The last part of the full-scale finite element model was the set of control cards for LS-DYNA. The majority of control cards were already defined in the NCAC guardrail model, so these cards were retained for the full-scale simulation. The only changes made were to the field XPene on Control_Contact, which set to 2. This field was used to set the maximum allowed penetration for contact definitions using the PenChk option. The total simulation time was raised to 1.0 seconds so that the behavior of the vehicle after impact could be examined.

The card Control_Dynamic_Relaxation was added to shorten the time spent in this part of the analysis. The tolerance criterion was raised to 0.05 and a termination time of 0.07 seconds was defined to prevent the relaxation from running too long.

3.5 Changes to Guardrail and Vehicle Models

Since the models that were available from the NCAC's finite element model were validated against test data, there was little need to make changes to the models. The only alteration to the guardrail model was an increase in the stiffness of the springs holding the splice bolts together. The increase in stiffness from 66,500 to 2,400,000 Newtons was needed to keep the splice bolts from popping apart during impact. The increase in stiffness reflected the bolt strength used in a model developed for a study on guardrails encased in paved strips [10]. The finite element model was also available from the NCAC finite element library [6].

There were a few additional changes to the Chevrolet 2500 pickup model as well. The vehicle tires tended to become unstable after experiencing deformation, so all four tires were changed from reduced integration shells to fully integrated shell elements. An interesting feature

of the vehicle model was meshing of parts making up the outer body of the vehicle was not symmetric, particularly in the fenders and adjacent parts. Since the long span crash test used that was to be used for model validation included an impact to the right side of a vehicle instead of the left, the right side of vehicle model was changed to match the left side. The mesh of the right fender was refined to match that of the left fender. Also, the null shells that were on the left side to improve contact stability were also added to the right side.

3.6 Measurements of Predamage Statistics

3.6.1 Post and Rail Deflection Metric

Each of the predamage modes for the strong-post w-beam guardrail, which could be rail deflection, post deflection, or both, was summarized by three pertinent numerical values:

1. The magnitude of rail deflection
2. The magnitude of post deflection
3. The rail flattening

Unless mentioned otherwise, all of these values refer to static measurements. In both the field and the finite element simulation, these three modes of damage almost always occur together. While the deflections of the rail and post were easily measured in the finite element model by looking at the change in nodal position, the evaluation of flattening was more difficult.

Both rail and post deflections are measured as perpendicular displacement from the line of the original guardrail. The line representing the original guardrail is created using two points on the front faces of blockouts on opposing sides of the crash damage. Both blockouts are far

enough away from the damage site that the crash had no significant affect on the blockout positions.

The displacement of the posts and rails was then measured using the perpendicular distance from the line to the rail or post. If the rail or post was bent or twisted, then the measurement was made from the point that was furthest from the line of reference. Only the X and Y coordinates were used in the calculation of distance. Changes in the vertical height of the guardrail components did not contribute to the displacement measurements. An illustration of this process is shown in Figure 11.

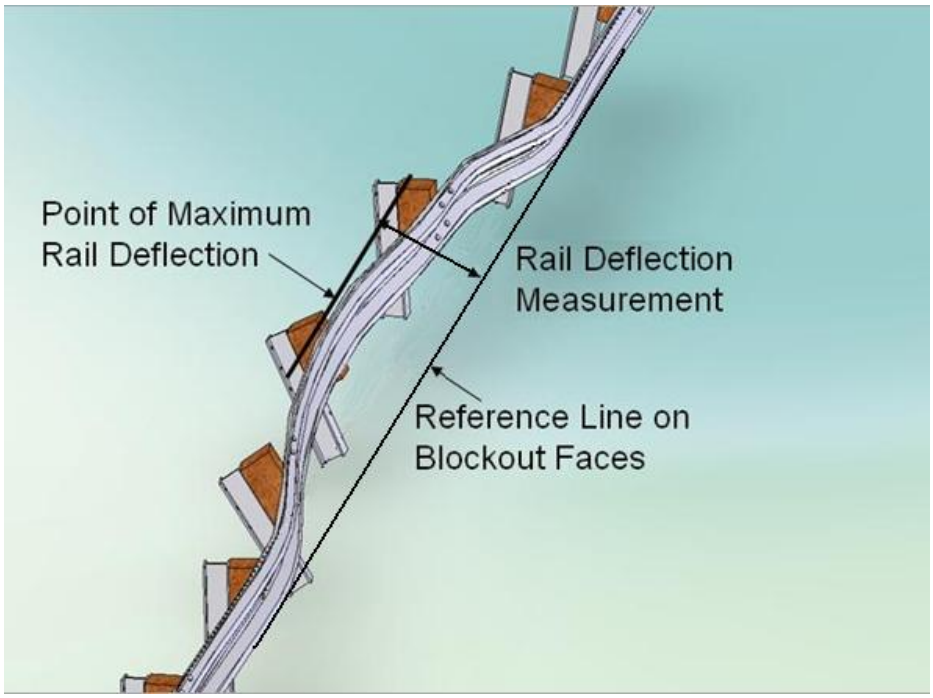

Figure 11: Methodology for measuring the rail deflection

3.6.2 Rail Deflection Metric

A rail-flattening metric has been developed to provide a single percentage for this damage mode. This metric was based heavily on finite element experiments in which the amount of flattening in the guardrail was observed to correlate well with the percentage of

change in cross-sectional height caused by compression of the rail between two rigid plates. Once the relationship between flatness and rail height was established, the measurement of rail flattening was made using simple measurements of the total rail height. In the finite element model, this height was evaluated as the distance between the topmost node and the bottom-most node. An example of this process is shown below in Figure 12 and Figure 13.

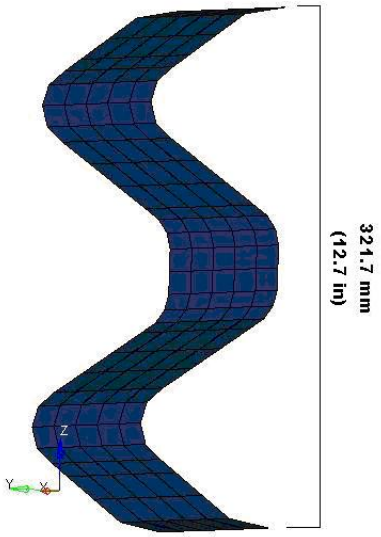

Figure 12: A small section of w-beam rail before flattening (0% flattened)

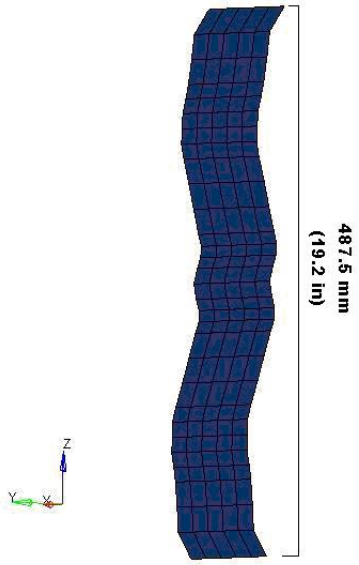

Figure 13: A small section of w-beam rail after flattening (78% flattened)

The resulting equation for rail flattening was broken down into linear and exponential components to account for the different behavior of minor flattening and extensive flattening. The equations are shown below in Table 6. The derivation of these equations is described in more detail in Appendix D.

Table 6: Equations to calculate rail flattening from rail height

Measure of Guardrail Height (h)	Equation for Flattening
Guardrail height (h) is 400 mm or less	$\left(\frac{h}{321.7}-1\right)\cdot 0.9112$
Guardrail height (h) is greater than 400 mm	$0.0718\cdot e^{4.6283\cdot\left(\frac{h}{321.7}-1\right)}$

3.6.3 Rail Tension

One of the limitations of the finite element model was an inability to predict failure via rail rupture, due to the lack of a failure strain criteria. To address the possibility of failure by rupture, the rail tensions for select models were collected to provide an indication of whether rupture would be more likely to occur. Tension measurements were performed with LS-PrePost using the SPlane 3 node cut to plot the force components. For all of the simulations, the same three nodes were used to define each of the cross sections.

Tension data was collected from vertical slices through each individual rail, at a location between two posts. Tension was measured in the region of rail between posts 9 and 21, which was the general area of contact with the vehicle during the crash test. Each slice was given a letter designation (A to L) to uniquely identify which part of the rail the tension data was obtained from. The location of each of the sections is illustrated in Figure 14 and Table 7.

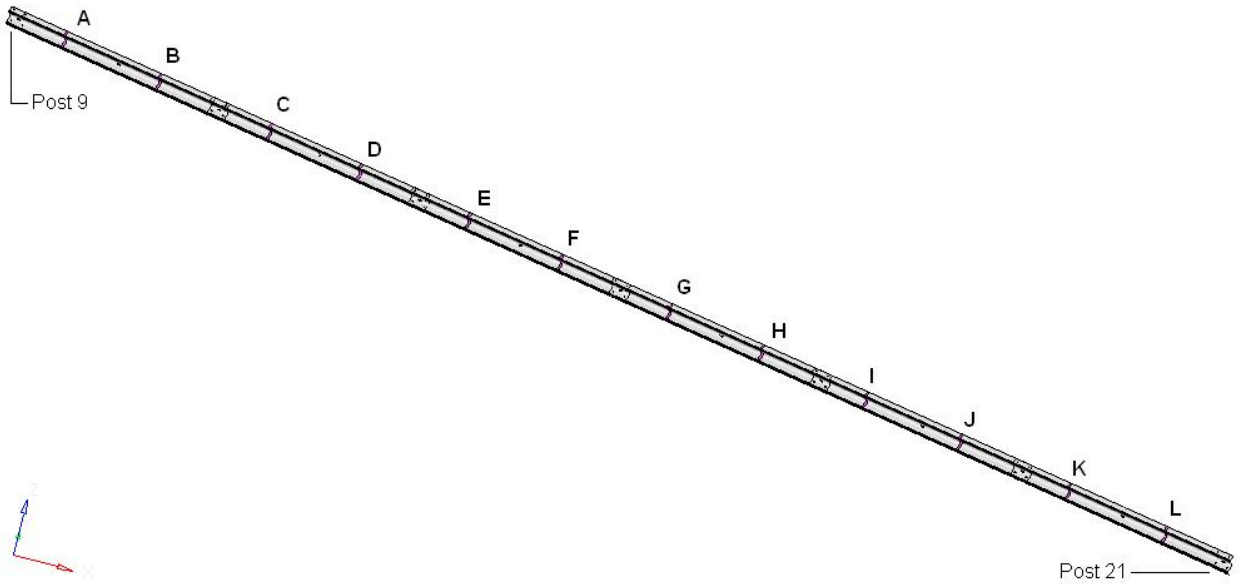

Figure 14: Locations of rail cross section cuts for measurement of rail tension

It was expected that the amount of tension in a rail should not vary in a section between any two posts. In other words, the tension measured between posts 9 and 10 should be the same

regardless of the location between these two posts that the cross section was defined. To demonstrate that this was the case, a number of cross section cuts were made between two adjacent posts, and the magnitude of rail tension was measured from each cross section. The resulting rail tension data is shown in Figure 15. Although the tension force data tended to be noisy, all of the slices generated the same results, confirming that the tension in the rail was the same between two posts no matter where the measurement was made.

Table 7: Mapping of section identifier to adjacent post numbers

Section	Upstream Post	Downstream Post
A	9	10
B	10	11
C	11	12
D	12	13
E	13	14
F	14	15
G	15	16
H	16	17
I	17	18
J	18	19
K	19	20
L	20	21

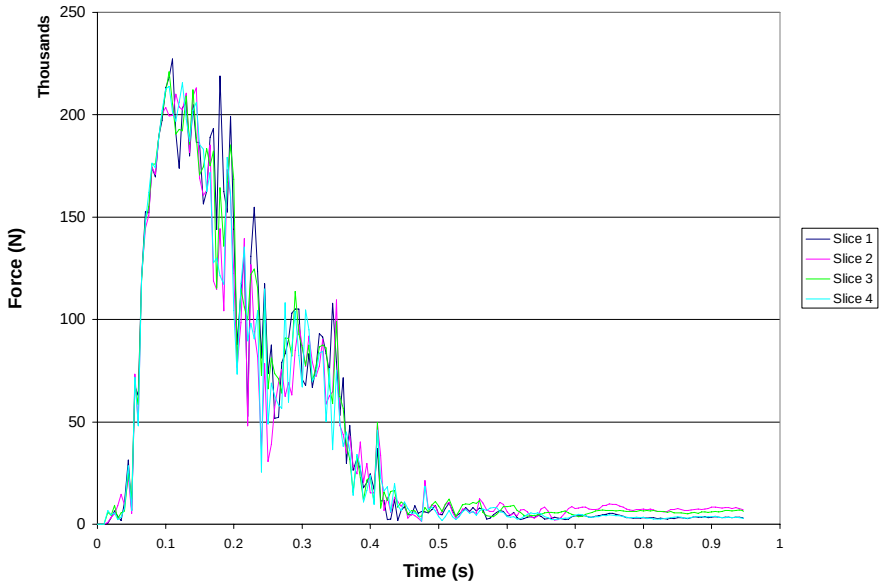

Figure 15: Magnitude of rail tension measured at several different cross sections between two adjacent posts

Tension data for the finite element simulations was collected from the sections as indicated in Figure 14. From each section, the X, Y, and Z components of the force, with respect to the global axis system, were collected. The three force components were then used to compute the magnitude of rail tension over time. Existing literature indicated that the weakest point in the rails was the splice joints, where the maximum sustainable quasistatic force was measured at 408 - 438 kN [11]. For this study, the tension was rounded off to be 410 kN, which was considered to be the highest amount of tension that the rails could carry before rupture would occur.

3.7 Methods of Inducing Controlled Damage

In this section, the modeling of damage in a guardrail system is discussed. The first topic is whether the inclusion of residual stresses in the guardrail was a critical aspect of the response of damaged guardrail. Whether these stresses were significant will determine whether future models will use only the damaged geometry or the geometry with stresses.

3.7.1 Geometric vs. Pre-Stressed Damage

From a logistics standpoint, the cost in time for running a large number of simulations was significant. This gives rise to the question of whether it was an acceptable substitute to reproduce only the geometry of a damaged section of guardrail. While this method represented significant time savings, it was unknown whether neglecting to account for residual stresses in the damaged rail could influence the results of the simulation. Thus, it was desirable to determine whether the residual stresses were indeed a critical aspect of damaged guardrail.

In order to evaluate this issue, two simulations were set up. The first simulation was similar to the validation model, except that it contained two vehicles. In this model, a pickup truck moving at a low speed impacted the guardrail and caused some damage to the guardrail. However, there was also a second vehicle in the simulation following a trajectory leading to the same point of impact. This second vehicle had a speed and trajectory consistent with the test level 3 conditions. Thus, the overall effect was the creation of realistic damage without losing the residual stresses in the damaged guardrail. However, the necessity of considering two vehicles in a simulation greatly increased the required computation time.

The second simulation contained an accurate portrayal of the geometry of the guardrail damage caused the first vehicle in the first simulation. This was accomplished by exporting the geometry of the guardrail from the previously discussed simulation at a time in between the first and second impacts. Since the first vehicle was not included in this simulation, there were no residual stresses in the guardrail. Thus, the damage between the two models was identical with regards to the geometry and mesh layout. Figure 16 below shows the striking similarity between the two models as the vehicles approach impact.

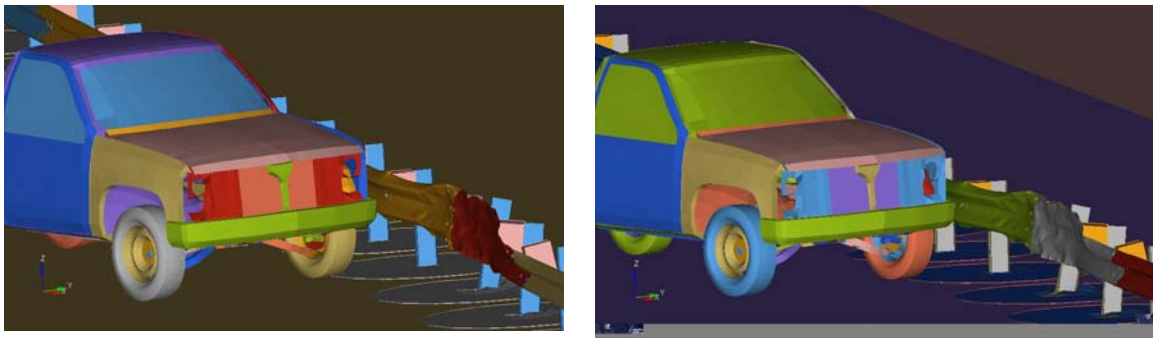

Figure 16: Two simulations of a pickup striking previously damaged guardrail under NCHRP 350 conditions. On the left is the simulation in which there were two vehicles and the residual stresses have been preserved. On the right, only the geometry of the deformation was preserved.

After all simulations were completed, the results were compiled. These results are presented below in Table 8. In all of the simulations, the vehicle rolled during exit and thus did

not have any measurable exit criteria. Additionally, the two models evaluating the effects of pre-damage in the guardrail reached the pre-assigned termination time before the guardrail has settled to its static position. Thus, there were no recordings for the static deflection for these simulations.

Table 8: Results of simulation series to determine the effects of residual stresses.

	Pre-stressed Simulation	Geometry Only Simulation	% Difference
OIV X (m/s)	6.4	6.9	7.8%
OIV Y (m/s)	7.6	7.6	0.0%
Ridedown X (G)	-6.9	-12.0	70.0%
Ridedown Y (G)	14.1	11.2	-20.6%
50ms X Avg (G)	-5.7	-6.0	5.3%
50ms Y Avg (G)	6.8	7.0	2.9%
Dynmc Def (m)	1.37	1.43	4.4%

Looking at the rail deflection first, it appears that the results were consistent between the pre-stressed and damage-only simulations, with both having rail deflections near 1.4 meters. The deflections of the damaged guardrail were measured from the damaged rail and added to the previously recorded static deflections. For the dynamic deflection, the inclusion of the residual stresses did not appear to have a significant influence on the results.

For the simulations including pre-existing damage, the occupant impact velocities, 50 ms moving averages and dynamic deflection all differed from each other by less than 10%. For these parameters, the residual stresses may have had some minor significance. Additionally, the Y-components of the occupant impact velocity (OIV) and 50ms average accelerations varied from the validation results by less than 5%. Paradoxically, there was a large inconsistency in the occupant ridedown accelerations despite the general agreement among the other parameters. This was attributed to the extremely noisy acceleration data produced by the simulation, which tended skew the ridedown accelerations toward much higher values.

Based on these results, a case can be made that reproducing the geometry of the damage can be an acceptable substitute to running a simulation with two vehicles. This was hugely beneficial because it reduced the run time needed to complete each simulation.

3.8 Limitations of the Study

One of the greatest limitations of this study was that only isolated damage modes were considered, whereas in the field multiple modes of damage may be observed as a result of a single impact. Rail flattening was probably the least likely of all the damage modes to occur in isolation, since any force sufficient to flatten the rail would likely be enough to cause some amount of deflection as well. The damage mode closest to what might be observed in the field would be the rail and post deflection damage. This damage mode included both deflection and flattening and also post separation if the magnitude of the deflection was sufficiently large.

The finite element models that were obtained for this study did not include any definitions of failure stress or strain for the vehicle or guardrail components, which prevented the use of the full-scale model to predict rail rupture. Although the failure strains for steels were well defined and widely available, the finite element model still was not capable of accurately reproducing failure by tearing. This was due to limitations imposed by the sizes of the elements, which were to large to be used to accurately model the local concentrations of stresses and strains that tended to occur around the splice joints and splice holes. Since failure strain could not be used to predict rail rupture, the alternative methods of evaluating stress and tension were employed.

Improving the model of the soil in which the posts were embedded would likely improve the performance of the model and would be a good starting point for future study. The major

difficulties with the soil model were the poor meshing and the ability to allow for the large deformations needed for a crash test. As a result of these issues, the soil component of the model suffered from severe hourglassing and excessive stiffness, which contributed to the low deflection of the guardrail in the simulations. An additional complication was that soil was a complex material to model, and can vary widely in material properties from one site to the next.

4. BASELINE VALIDATION

4.1 Introduction

To avoid the significant cost of performing a large series of crash tests, the finite element modeling approach was used to evaluate the crash performance of previously damaged guardrail. While this represents a significant savings in time and cost, it also required that additional effort be undertaken to demonstrate that the resulting finite element mode was capable of producing realistic results. The best way to show that this was true was to use the finite element model to reproduce the results of an existing crash test. If the finite element model was successful in predicting the crash outcome and the NCHRP 350 test criteria values, then the finite element model would be shown to be a valid alternative to the full scale testing.

The crash test that was selected for this purpose was a test performed by the Texas Transportation Institute (TTI) to demonstrate the safety of the modified G4(1S) guardrail [3]. The crash test was a success, with the vehicle being redirected away from the guardrail. The occupant impact velocity and ridedown acceleration were well below the recommended values of 9 m/s and 15 G, respectively. The damage to the guardrail was considered to be moderate, with approximately 1 meter of dynamic deflection and 0.7 meters of static deflection recorded.

Because this was a validation simulation, there was no need to induce any pre-existing damage in the guardrail. Thus, the finite element model of the vehicle and guardrail was unmodified. The finite element vehicle was given initial conditions to match the test level 3 crtieria, i.e. an initial velocity of 100 kph and an impact angle of 25 degrees. This varied slightly

from the real test, for which the initial speed was 101.5 kph at 25.5 degrees. The model was run as is for 1,000 ms and compared to the documented crash test results.

4.2 Results

The completed simulation was first compared to the original crash test by visual inspection. Table 9 below shows a time series of photographs looking down the length of the guardrail. In most real crash tests, the time recorded by the camera was scaled so that at time 0, the vehicle had just touched the guardrail. To match this effect in the simulation, a – 10 ms bias was applied to the simulation.

As can be seen from the time series, the overall behavior of the vehicles matched up well. The simulation showed more roll and pitch than was observed in the crash test in the range of 180 – 490 ms, but it eventually leveled out to the same amount. Due to the large amount of dust stirred up in the crash test, a visual comparison of the guardrail deflection was not possible. However, the guardrail deflection data was still collected for the real test via the overhead camera for which the data is not shown.

Table 9: Comparison of undamaged guardrail crash test and simulation

TTI Crash Test 405421-1 [3]	Simulation of Undamaged Guardrail
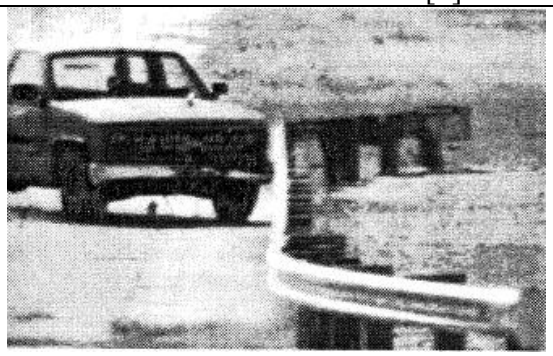 t = 0 ms	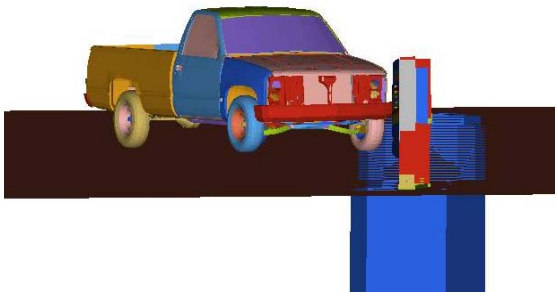 t = 0 ms
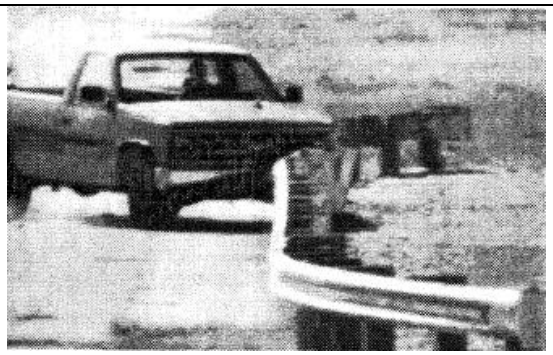 t = 61 ms	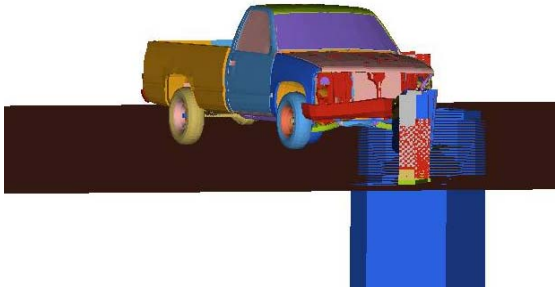 t = 60 ms
 t = 120 ms	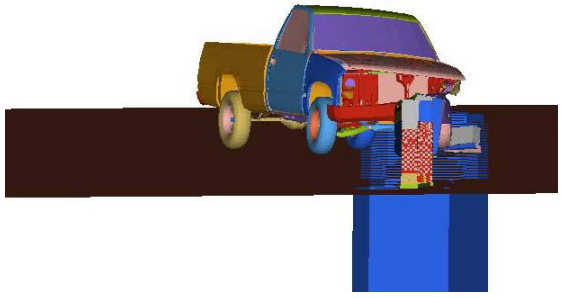 t = 120 ms
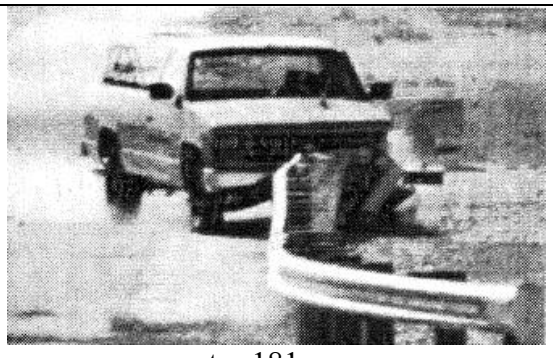 t = 181 ms	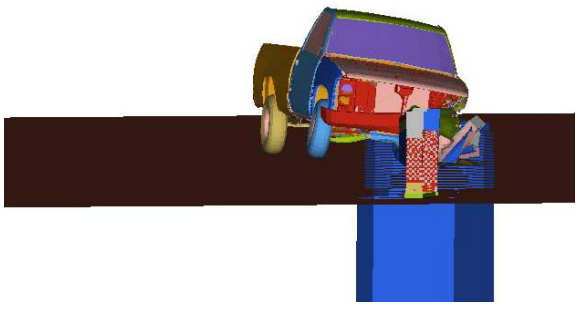 t = 180 ms

 t = 242 ms	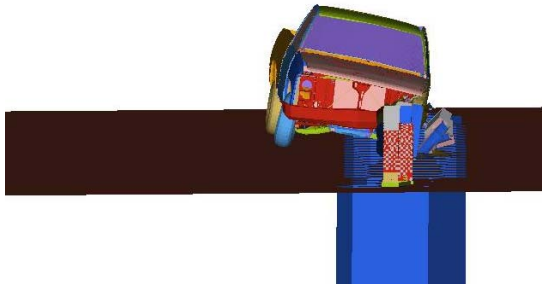 t = 240 ms
 t = 359 ms	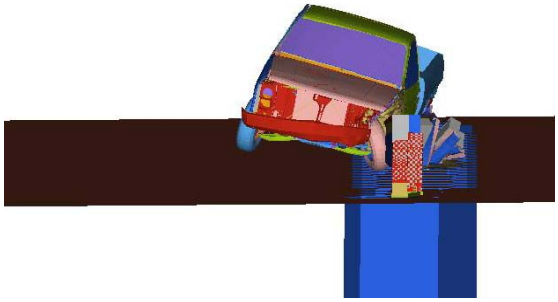 t = 360 ms
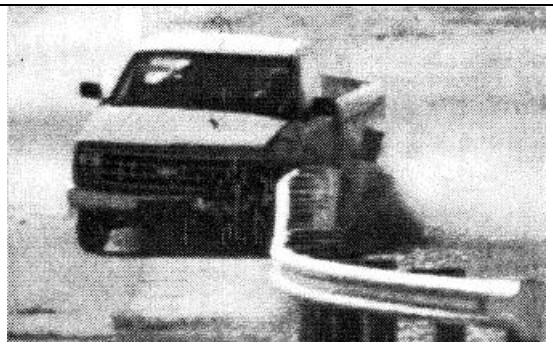 t = 491 ms	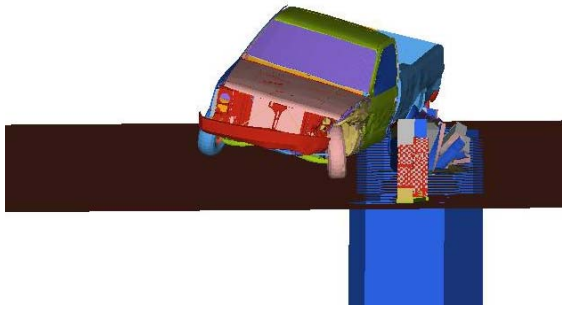 t = 490 ms
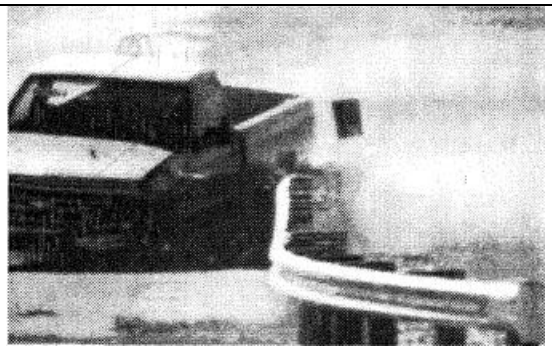 t = 691 ms	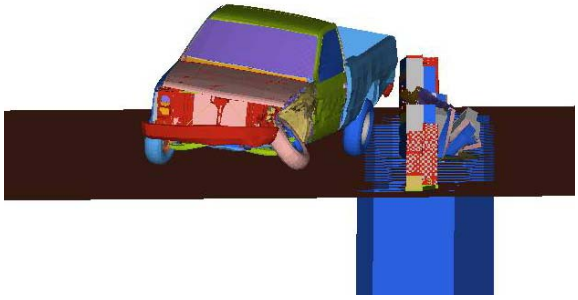 t = 690 ms

In addition to the visual data, all of the criteria specified by the NCHRP 350 test level 3 protocols were calculated. These results are shown in Table 10. The initial conditions varied slightly because it was difficult to get precisely the specified values for the real crash test, whereas in the simulation it was relatively easy. Many of the results matched up well, but some did not.

Table 10: Results for undamaged crash test and simulation

		TTI Test 405421-1 [3]	Undamaged Simulation	% Change
Impact Conditions				
	Speed (kph)	101.5	100.0	-1.5%
	Angle (deg)	25.5	25.0	-2.0%
Exit Conditions				
	Speed (kph)	55.0	53.0	-3.6%
	Angle (deg)	16.0	14.5	-9.2%
Occupant				
	Impact Velocity X (m/s)	7.1	7.5	5.8%
	Impact Velocity Y (m/s)	4.4	5.5	25.9%
	Ridedown X (G)	-7.9	-11.8	49.0%
	Ridedown Y (G)	8.4	-12.3	46.1%
	50 ms Average X (G)	-5.3	-6.7	26.1%
	50 ms Average Y (G)	4.3	-6.8	58.7%
	50 ms Average Z (G)	-4.8	-3.8	-19.8%
Guardrail Deflections				
	Dynamic (m)	1.0	0.69	-31.1%
	Static (m)	0.7	0.55	-21.1%
Vehicle Rotations				
	Max Roll (deg)	-10	-14.4	44.0%
	Max Pitch (deg)	-4	-9.9	147.5%
	Max Yaw (deg)	42	40.3	-4.1%

The vehicle exit speed and angle agree very well with the crash test, although the percent error was large for the exit angle because the initial value was so small. The longitudinal occupant impact velocity (OIV) also agreed between the two. The lateral OIV was higher.

However, the differences between the longitudinal and lateral OIV were the same for both the real crash test and the simulation.

Similar to what was observed for the time series, the vehicle roll and pitch were higher in the simulation than for the real crash test. Both the roll and pitch differed by roughly five degrees, which was a relatively small amount but resulted in a large percent change because of the small values recorded for the crash test. Taken together with the lower exit speed, it was an implication that the friction between the vehicle and guardrail may be slightly high. The max yaw was slightly lower. In general, the vehicle maximum yaw was found to be strongly related to the exit angle of the vehicle.

The vehicle 50 ms average acceleration and especially the ridedown accelerations from the simulation were different from the crash test. Extremely high accelerations were observed for all of the simulations that were conducted in this study. The suspected cause was the finite element solver itself, particularly the way the contact algorithms work. Since the contact algorithms apply forces based on the depth by which a node was intrudes into a surface, the contact forces can vary wildly from one time step to the next. Because of this, the measurements of acceleration tended to be unreliable when sampled over a small time interval.

The guardrail deflection was much lower than was expected in the simulation, being roughly 0.7 meters instead of the expected 1 meter. The deflection contour of the simulated guardrail is shown in Figure 17. The static deflection was also lower, but by a smaller amount. The differences in the guardrail deflection were attributed to the soil model which was for a very stiff soil.

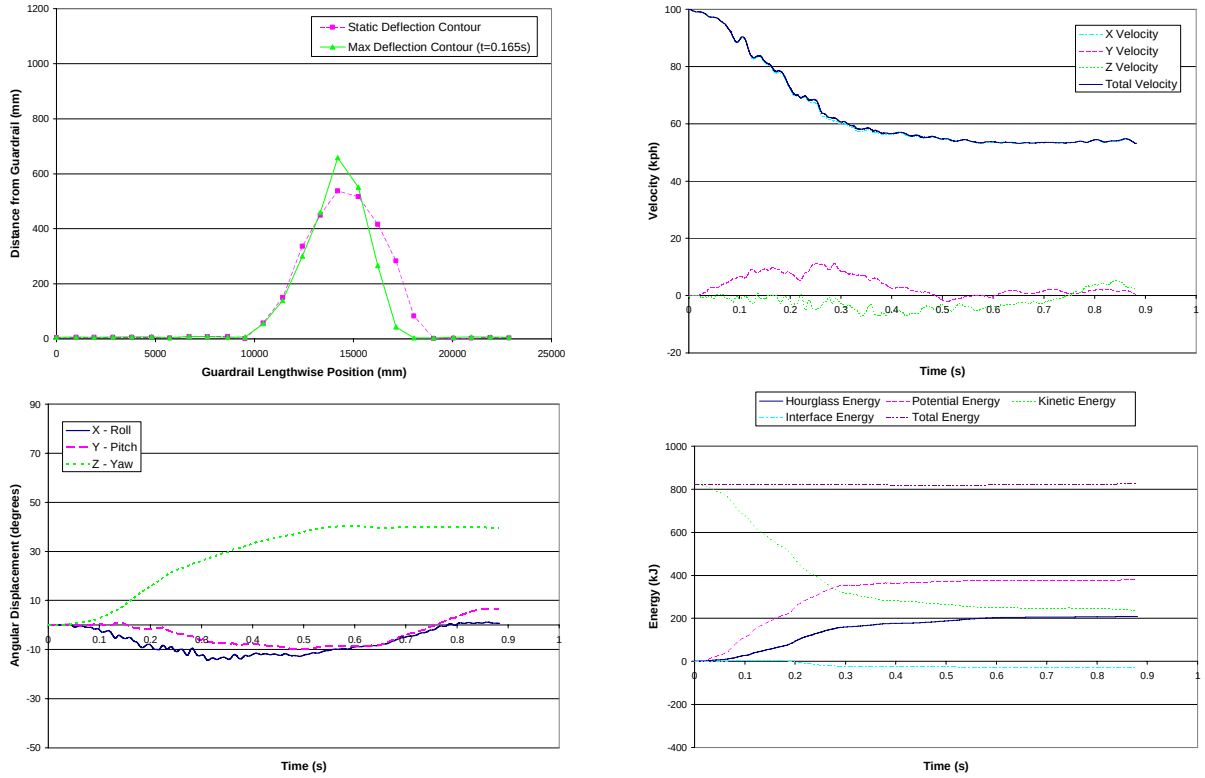

Figure 17: Results of the undamaged simulation. Guardrail deflection (top left), vehicle velocity at center of gravity (top right), vehicle rotation (bottom left), and simulation energy balance (bottom right)

The energy balance for the simulation is presented in the bottom right graph in Figure 17. The total energy of the simulation was stable, which was a good indicator of numerical stability. The interface energy was slightly negative, which was to be expected when many of the contact definitions do not include friction. However, the hourglass energy was higher than desired at roughly 25% of the total energy in the simulation. Parts that experienced large deformations such as the vehicle fender and wheels, posts, soil, and contacted rails were the largest contributors to this energy.

The tension carried by the rails during impact was collected and is shown in Figure 18. For this particular simulation, the maximum observed rail tension was 237 kN, occurring in slice E (between posts 13 and 14). The measured tension was well under the maximum allowed tension of 410 kN and was within the range of tensions that would be expected during full scale

crash testing [11]. Because the tension carried by the rail was low, there was no risk of rail rupture occurring. However, the tension measured for this simulation provided a baseline rail tension against which the results of the damage mode simulations could be compared.

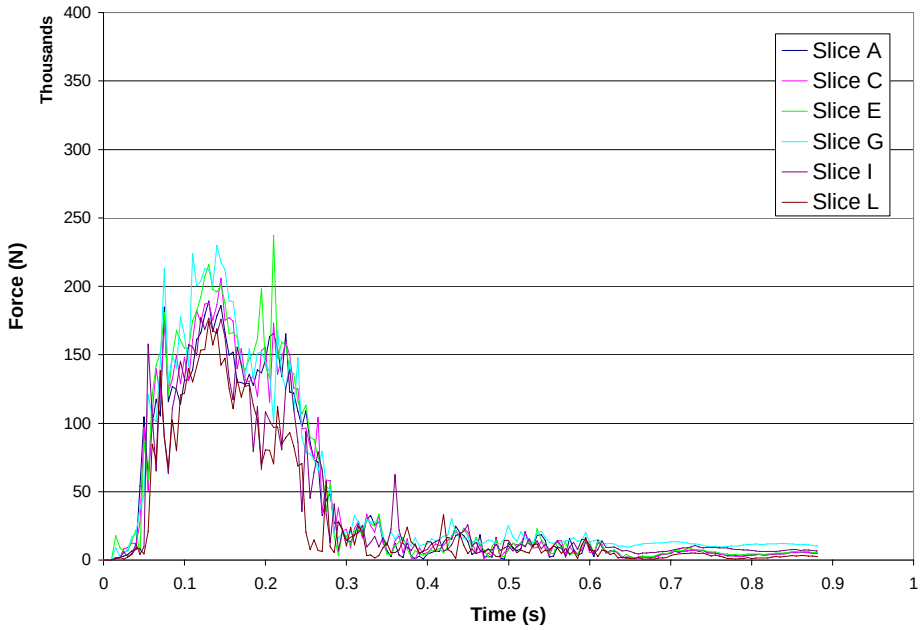

Figure 18: Rail tension for undamaged guardrail simulation

4.3 Discussion

The modeling of the undamaged crash test revealed a number of potential issues with the model that were particularly difficult to address. While the greatest of these focused on the soil model, there were also potential issues with the measurement of the rail deflection and hourglassing in the deformed parts.

4.3.1 Accuracy of the Soil Model

Most of the vehicle-specific test level 3 criteria matched up well, although there was a problem with matching the guardrail deflection. The dynamic deflection of the guardrail was

roughly 30% lower than observed in the crash test, which was a large difference. The cause of this discrepancy was believed to be the soil model, which was much stiffer than the soil in the crash test. However, the type of soil, and the preparation performed on it, tends to be poorly documented in crash test publications.

There was some concern that the size of the soil buckets holding each post was not enough to allow the post to move naturally. However, the effect of soil bucket size was evaluated by increasing the total size, replacing the buckets with a continuous trough (detailed in Appendix C), and adding non-reflecting boundaries to approximate an infinite soil domain. Each of these approaches produced only slight increases in the resulting deflection of the posts and guardrail, implying that the size of the soil bucket was not a cause of the lower deflection in the simulated guardrail.

The problem of the soil stiffness was compounded by the fact that the guardrail model that was used for this study may not have been developed for the soil that was used in the TTI crash test. An investigation into the effects of the soil model on the guardrail performance revealed that the two were closely related. When the material model of the soil was weakened by allowing a greater strain for a given soil pressure, or a softer soil model such as Drucker-Prager was used, the deflection of the guardrail increased.

Another problem with the modeling of the soil was the complex geometry of the posts. To accurately represent the resistance to post torsion, it was necessary to model the soil that was present in between the flanges. By necessity, these elements were fairly small in length and width while being very tall, leading to very large aspect ratios for the elements. Yet in the LS-DYNA manual [9], there was a warning against this very situation as it tended to cause excessive

stiffness in the soil. This effect became more pronounced as the deformation of the soil increased.

Ultimately, although the problems with the guardrail deflection were eventually isolated to the unknown soil conditions and the unnatural stiffness of the elements under large deflections, a reasonable solution that did not affect the model stability or the time needed to complete a simulation was not found. It was decided that the deflection for the simulations of pre-damaged guardrail would be evaluated as the percentage change from the simulation of undamaged guardrail, rather than using the absolute value of deflection. This way, the changes in guardrail deflection would be applicable to the results of the real crash test.

4.3.2 Measurement of Rail Deflection

One of the greatest problems in measuring the rail deflection was that the methodology for doing so was not precisely specified. In most crash tests, the deflection was mentioned as having been measured by video analysis, but the methodology and how the points of reference were determined were not specified. Thus, it was possible that the deflection could have been exaggerated or understated, depending on how the deflection was actually measured.

As was discussed in the methods section, the deflection of the simulated guardrail was measured as the distance between a line representing the undamaged guardrail and the closest point on the guardrail. It would have been possible, then, to increase the measured deflection simply by changing the approach to measuring to the farthest point on the guardrail rather than the closest point. Changing the measurement technique was found to result in a variance of +/- 100 mm for the undamaged simulation. While this could improve the accuracy of the deflection measurement, it still does not fully explain the large decrease in deflection for the simulation.

Therefore, it was likely that the soil stiffness had some significant influences as well, as discussed in the previous section.

4.3.3 Hourglass Energy

The hourglass energy ended up being a larger portion of the total energy of the simulation than was desired. In finite element models, hourglass energy is the cost associated with the use of faster, reduced integration elements. While using these elements greatly reduced the time needed to run each simulation, there was a price paid in the energy that was diverted to the hourglass modes. The energy was particularly focused in parts of the model that were greatly deformed, i.e. the impacted rails and the vehicle fender.

Some sources of hourglass energy, such as the soil and wooden posts, could not be addressed because the options available to treat solid elements were quite limited. Attempts to reduce the amount of hourglass energy consumed by solid elements were met with failure as the simulations became unstable and terminated well before the crash was completed.

The absorption of crash energy through hourglassing could have been another contributor to the low deflection of the guardrail in the simulation. It was believed that by fully integrating all of the rails, the deflection might increase. To test whether hourglassing was causing the low guardrail deflection, the undamaged simulation was rerun. In this simulation, all parts modeled as thin shells were fully integrated. As a result, the hourglass energy at the end of the simulation decreased from 210 kJ to 58 kJ and the potential energy increased from 379 kJ to 539 kJ. Thus, the hypothesis that hourglass modes were absorbing potential energy was true. However, the deflection of the guardrail was observed to decrease slightly (~0.02 meters) in the fully integrated simulation. This was due to the fully integrated elements being stiffer than the

reduced integration elements. Since the fully integrated elements greatly increased the runtime and provided minimal benefit, they were not used for the simulations of damaged guardrail.

4.4 Conclusion

The finite element model of the undamaged guardrail matched well with the crash test, with the one major exception being the measured guardrail deflection. The disagreement with the guardrail deflection was found to depend on a number of factors including the properties of the soil, the stiffness of the guardrail components, and the method by which the deflection was measured. To accommodate the underprediction in deflection, an alternative approach was used. Rather than comparing the absolute measure of guardrail deflection, the percentage change between this simulation and the future simulations could be used. In this way, the simulation results in which the guardrail possessed minor damage could be applied to the real crash test results.

The measurements of vehicle acceleration were computed, but were not found to be particularly valuable due to the large variability in the recorded data. The vehicle exit speed and angle, the occupant impact velocities, and the vehicle rotations all matched well to the values observed in the crash test. These measures will be particularly valuable as the simulations of damaged guardrail are completed and compared to this simulation of the undamaged guardrail.

5. MISSING POSTS MODELS

5.1 Introduction

One of the damage conditions under consideration for this study was missing posts in the strong-post w-beam guardrail system. Posts can be missing from a guardrail system from causes such as crash damage or extensive post rot. For some guardrail systems, posts may be missing on purpose. An example would be a guardrail needing to span a culvert, with modifications made to compensate for the loss of strength due to the missing posts.

For this study, the focus was solely on strong-post w-beam guardrail that was unintentionally missing posts. Thus, the guardrail contains no modifications that might compensate for the loss of lateral strength. Because there was no literature on unmodified guardrails with missing posts, a series of simulations was planned to best ascertain the limit at which the guardrail can no longer contain the vehicle safely.

5.2 Methods

5.2.1 Creation of Pre-existing Damage

The missing post damage conditions was one of the simpler damage conditions to model. To reproduce the damage, the entire post, along with all the supporting elements, was simply deleted from the simulation. The supporting elements consisted of the soil, post bolt, post nut, and blockout. An example of this process is shown in Figure 19. Any LS-DYNA contacts specific to the removed posts were also deleted.

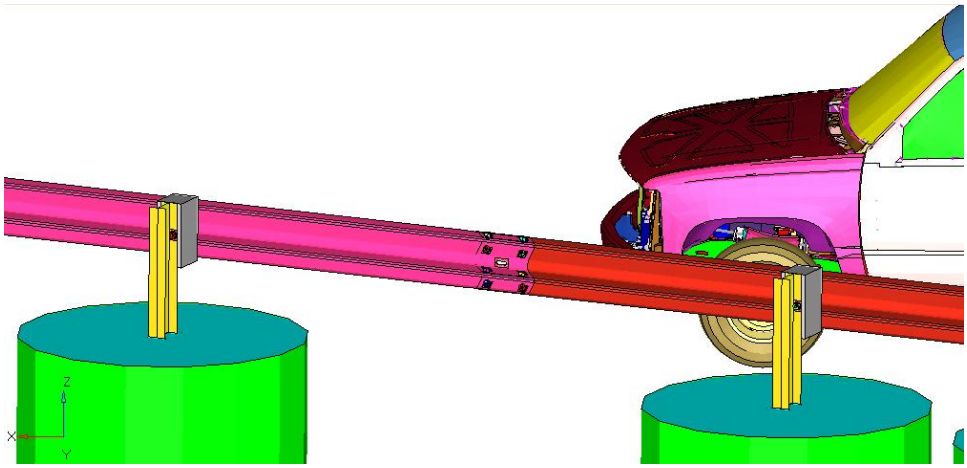

Figure 19: Simulated guardrail missing one post

5.2.2 Validation

Ideally, the performance of strong-post w-beam systems with missing posts could be determined from crash tests, but there are no crash tests to our knowledge with this exact damage mode. However, there are some crash tests of specialized variations of guardrail called long span systems [12, 13]. Long span systems are different from the systems under consideration in the chapter because the posts are missing by design. Long span systems are used wherever posts cannot be driven into the ground. The most common reason being the presence of medium to large culverts under the roadway.

Long span systems are typically modified in order to compensate for the loss of one or more posts. Typically, the rails are nested (doubled up) over the unsupported portion of the guardrail and the adjacent sections of the rail that would be involved in the impact. Other long span systems may also incorporate changes to the blockout spacing or number of blockouts.

Despite these differences, the long span crash tests were useful in validating the finite element model of missing post guardrail systems. Three missing post tests were available: a long span crash test with three missing posts performed by the University of Nebraska-Lincoln (UNL) and denoted as OLS-2 [12], a second long span crash test with modified blockout spacing also

performed by UNL called OLS-3 [13], and a long span crash test of a wood strong-post guardrail with two missing posts performed by the Texas Transportation Institute (TTI) [14]. The respective result for each crash test was a rollover, a successful test, and a rail rupture.

The crash test OLS-2 (hereafter referred to as the UNL crash test) was selected for several reasons. First, the guardrail design was less modified than the OLS-3 test, and thus was closer to the type of missing post guardrail systems of interest for this study. Secondly, the damage condition was more severe than the two post TTI crash test. Also, the test was of a steel strong-post system, which matched the finite element model more closely. Finally, being able to accurately reproduce the failure by rolling of the vehicle in the crash test would confirm the ability of the finite element model to predict the crash test results, especially in combination with the results of the undamaged simulation discussed in the previous chapter.

5.2.3 Planned Simulations

As mentioned previously, a major limitation of all of the crash tests that could be used to validate a missing post model were of limited use, because of the modifications made to the system to compensate for the loss of strength. Thus, there were no indicators of how many posts could be removed before the integrity of the guardrail system would be compromised.

A series of finite element simulations was planned to accurately identify the point at which the performance of the guardrail becomes unacceptable. In the UNL crash test [12], the modeling software Barrier VII was used to identify the critical impact point as being 2.44 m downstream of the last post before the unsupported span. However, these results were applicable only to the nested guardrail system with three missing posts that was used for the UNL test. The crash test of the guardrail missing two posts contained no discussion of where the critical impact point would be located.

Because the simulations planned for this study did not call for nested guardrail and the Barrier VII software was not available, the critical impact points were not known. In an attempt to resolve this problem, two different impact points were used to examine the effects of impact location. While more impact points would have provided more accuracy in pinpointing the critical impact point, the cost in time to perform so many simulations for each of the missing post conditions was prohibitive. The final set of planned simulations contained only two impact points for each of the missing post damage conditions, which resulted in the six simulations that are summarized in Table 11.

Table 11: Planned missing post simulations

Simulation #	# of Missing Posts	Impact Point
1	1	Mid-span
2	1	Beginning of span
3	2	Mid-span
4	2	Beginning of span
5	3	Mid-span
6	3	Beginning of span

5.3 Results

5.3.1 Validation of the Missing Post Model

Before running the missing post simulations, it was important to show that the predictions of the finite element model were reasonable. To achieve this, a review of crash tests performed on missing post systems was conducted. The study selected for validation was a crash test of a strong-post w-beam guardrail system missing three posts, performed by the University of Nebraska-Lincoln (UNL) as part of a study of long-span systems [12]. The strong-post w-beam long span guardrail is shown in Figure 20.

Figure 20: Strong-post w-beam guardrail with nested rail used for UNL crash test

The guardrail system shown was a 53.3 meter long installation of strong-post w-beam guardrail. Nested rails were used to cover a 30.48 meter region in and around the area of impact, i.e. the unsupported span. Three posts on each side of the unsupported span were replaced with wooden posts as well, to lessen the chance of the vehicle getting caught on the posts. In this crash test the critical impact point was calculated via Barrier VII to be 2.44 m downstream of post 12.

The undamaged finite element model of strong-post w-beam guardrail model was modified to resemble the UNL crash test. The modifications included the addition of nested guardrail and wood posts around the area of impact, as well as the removal of three posts. The final change was to the end constraints. In the UNL crash test, only two posts on each end were wooden terminal posts. Two wooden posts from each end of the finite element model were replaced with steel posts. The position of the guardrail in the finite element model was adjusted so that the vehicle impact point was 2.2 m downstream of post 12, which was similar to the impact point for the UNL crash test. The finite element vehicle was also adjusted to match the vehicle dimensions of the UNL test vehicle, as shown in Table 2.

The validation simulation was run with the same settings as discussed above in the methods section, except that the runtime was increased to 1.5 seconds to see if the post impact behavior of the vehicle matched with the crash test. Table 12 below presents a series of pictures from both the UNL crash test and the simulation at varying times. The simulations matched visually up until the vehicle exited the guardrail system. The simulation terminated early at 0.935 seconds, due to the large force applied to the vehicle front left tire when it returned to the ground. Because of this, it was not known whether the simulation vehicle would have rolled.

Table 12: Comparison of UNL Crash Test and Simulation

UNL Long-Span Crash Test [12]	**Simulation of UNL Test**
	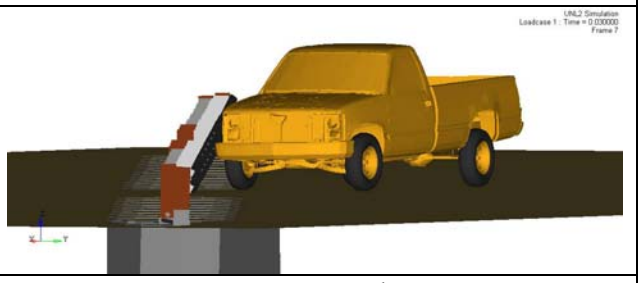
t = 0 seconds	t = 0 seconds
	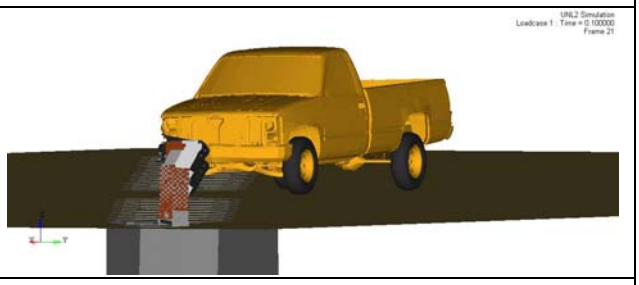
t = 0.072 seconds	t = 0.070 seconds
	
t = 0.126 seconds	t = 0.125 seconds

	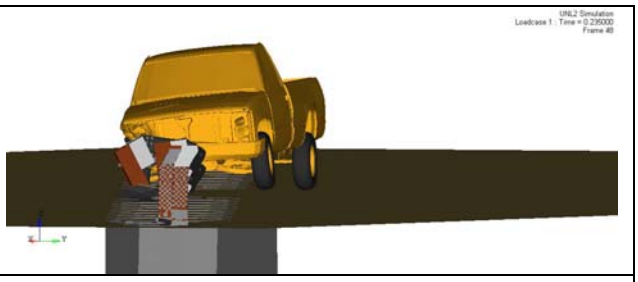
t = 0.206 seconds	t = 0.205 seconds
	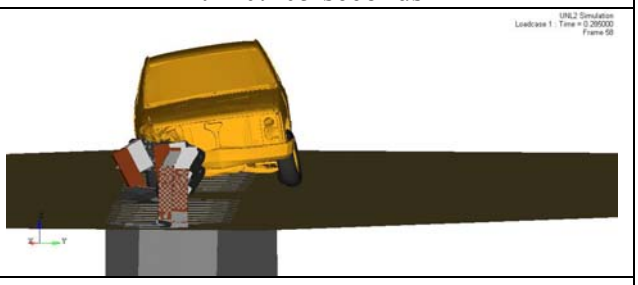
t = 0.254 seconds	t = 0.255 seconds
	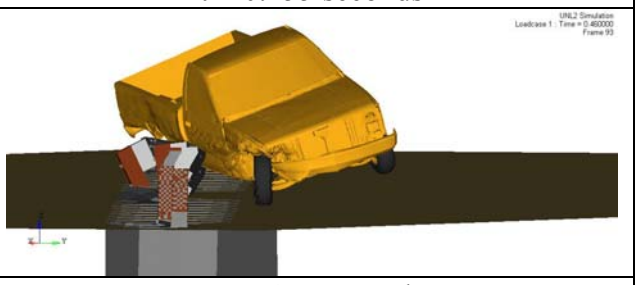
t = 0.428 seconds	t = 0.430 seconds
	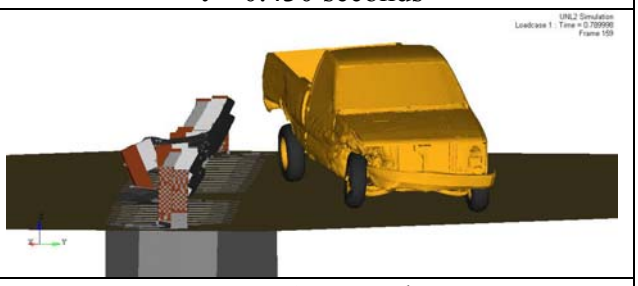
t = 0.760 seconds	t = 0.760 seconds
	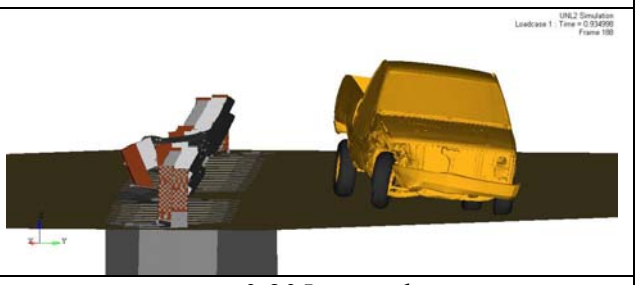
t = 0.946 seconds	t = 0.905 seconds

Visually, the crash test and simulation matched well until the vehicle exited the guardrail. The vehicle pitched more in the crash test than in the simulation. Even though the crash test

ended unsuccessfully with the test vehicle rolling over, some of the NCHRP 350 test criteria were still computed, providing some numerical data to further validate the simulation. These results, along with the simulation results are shown in Table 13. The simulation predicted a lower exit speed and higher accelerations and occupant impact velocities, suggesting that the simulation impact was more severe than that of the real crash test. One possible source of the increased forces was the wooden posts, which did not fracture in the simulation as in the crash test. Part of the problem was in the difficulty of modeling a wood material. The wood material properties depend strongly upon the grain quality and direction which varied from piece to piece. Another possible problem may be the soil strength, which was not known. From photographs from the crash test, the soil may have been much stronger than the soil used for the simulation.

Table 13: Results for UNL crash test validation

		UNL Crash Test	Validation Simulation
Impact Conditions			
	Speed (kph)	102.7	102.7
	Angle (deg)	24.5	24.5
Exit Conditions			
	Speed (kph)	66.2	55.0
	Angle (deg)	16.7	16.3
Occupant			
	Impact Velocity X (m/s)	6.7	8.6
	Impact Velocity Y (m/s)	5.0	-6.3
	Ridedown X (G)	6.4	-14.0
	Ridedown Y (G)	8.3	14.6
	50 ms Average X (G)	NR	-9.1
	50 ms Average Y (G)	NR	8.6
	50 ms Average Z (G)	NR	-4.9
Guardrail Deflections			
	Dynamic (m)	1.3	1.0
	Static (m)	1.0	0.7
Vehicle Rotations			
	Max Roll (deg)	Rolled	14.3
	Max Pitch (deg)		-15.5
	Max Yaw (deg)		-43.5

Figure 21 shows the vehicle rotation around the CG for the UNL crash test. Figure 22 shows the vehicle rotation observed in the simulation of this crash test. The roll, pitch, and yaw show similar values up until the time the vehicles left the guardrail (around 0.7 seconds). After this point, the behavior of the real and simulated vehicle diverged, with the real vehicle yawing considerably more. Because the simulation terminated early, it is unknown what the simulated vehicle behavior would have been after the impact.

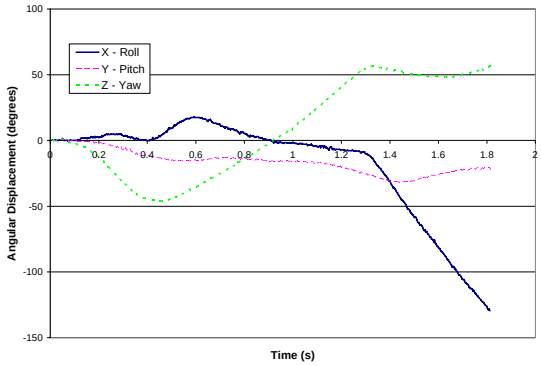

Figure 21: Vehicle CG roll, pitch, and yaw for UNL crash test

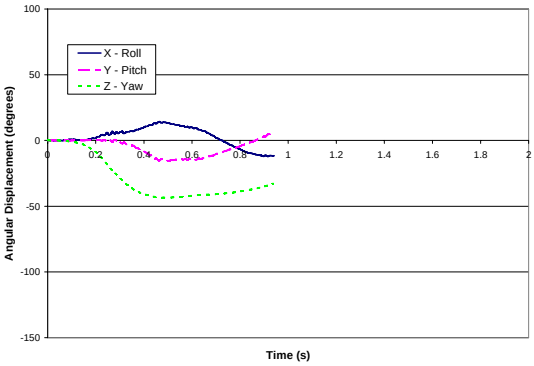

Figure 22: Vehicle CG roll, pitch, and yaw for UNL simulation

The plots below (Figure 23 - Figure 25) show additional results for the simulation of the UNL crash test. The crash test report did not contain equivalent data, so there was no way to compare these results to the crash test results. However, there was a very large increase in the magnitude of rail deflection as compared to the simulation of undamaged guardrail (data not shown). In Figure 23, the deflection was measured from post 14 to post 7. The simulation energies, shown in Figure 25, revealed that the residual vehicle velocity and energy absorbed through deformation accounted for approximately 80% of the simulation energy. Another 17% of the energy was accounted for by the hourglass and interface energies. The unofficial recommendation at the time was for hourglass energy to be less than 10% of the total energy, so this was higher than desired. However, it proved difficult to eliminate the hourglassing without

increasing the time needed to complete each simulation dramatically. The remaining energy was dissipated through the vehicle dampers and joints and the ground.

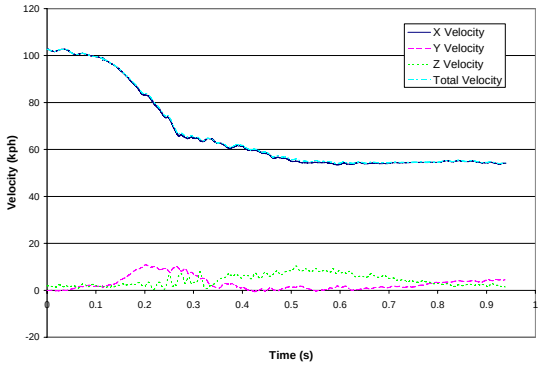

Figure 23: Vehicle CG velocities for UNL simulation

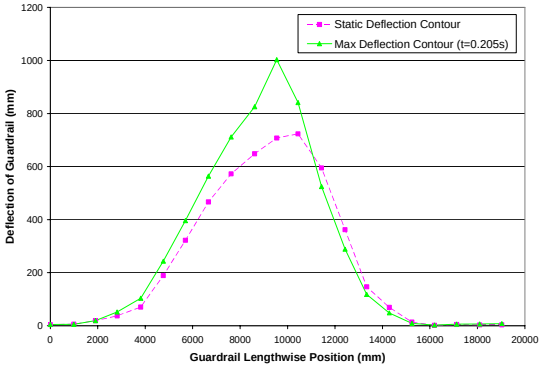

Figure 24: Guardrail deflection contours (static and maximum) for UNL simulation

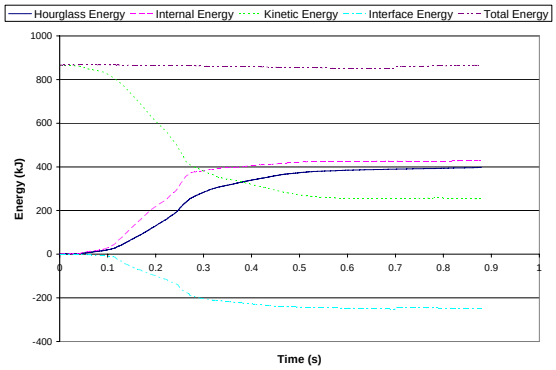

Figure 25: Energies for UNL simulation

The simulation was able to match the UNL crash test with reasonable accuracy up until 0.5 seconds, after which the behavior of the vehicles diverged. In the crash test, the vehicle pitched and ultimately rolled over but the simulation failed to reproduce this behavior. The simulation was overall an adequate approximation of the crash test.

5.3.2 Missing Post Simulations

With the missing post model validation completed, a series of finite element simulations was developed to determine the effect of missing posts on the vehicle – guardrail crash performance. Unlike the validation simulation however, there were no alterations made to

compensate for the missing posts. All of the posts around the impact area in these models were steel posts and none of the guardrails were nested. The test matrix for the three missing post simulations, each with two different initial impact points, is shown below in Figure 26 - Figure 31 .

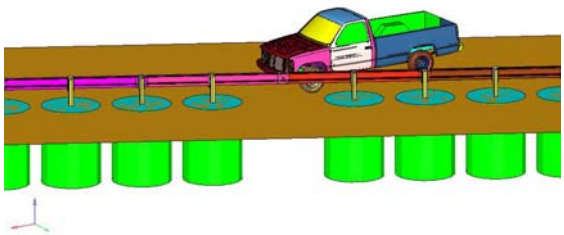

Figure 26: Simulation of 1 post missing. Impact point is at the middle of the unsupported span.

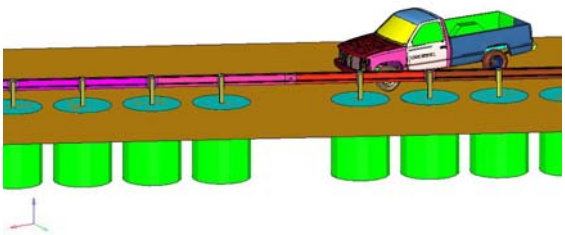

Figure 27: Simulation of 1 post missing. Impact point is at the beginning of the unsupported span.

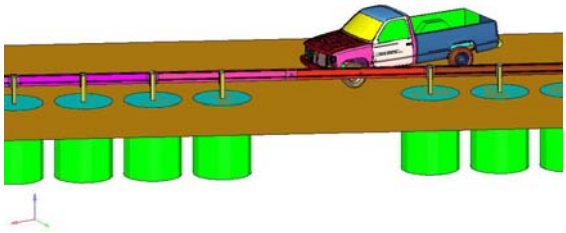

Figure 28: Simulation of 2 posts missing. Impact point is at the middle of the unsupported span.

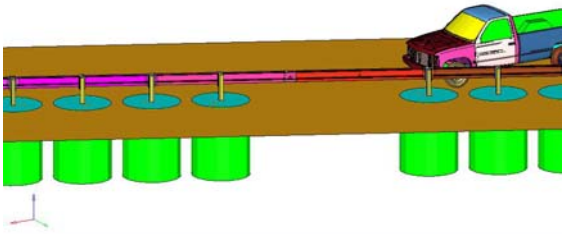

Figure 29: Simulation of 2 posts missing. Impact point is at the beginning of the unsupported span.

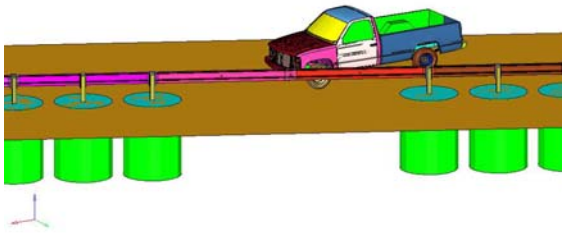

Figure 30: Simulation of 3 posts missing. Impact point is at the middle of the unsupported span.

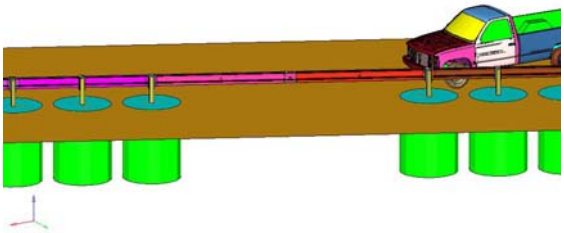

Figure 31: Simulation of 3 posts missing. Impact point is at the beginning of the unsupported span.

Each simulation required approximately 26-28 hours to run. All of the runs were performed on a SGI Altix parallel system using four processors for each simulation. However, there were multiple simulations running at any given time. Pictures depicting the simulation results at 700 ms are shown in Figure 32 - Figure 37. Numerical results are tabulated in Table 14 - Table 17.

The initial point of impact appeared to have a stronger effect on the simulation results than the number of missing posts. Simulations in which the vehicle struck the guardrail at the beginning of the unsupported span predicted less severe roll and pitch (all less than 10 degrees). This was true with respect to both the undamaged guardrail simulation and the missing post simulations for which the impact point was mid-span. The mid-span simulations showed higher roll and much higher pitch values. The most severe kinematics were associated with the system missing one post and impacted at the mid-span. For this simulation, the vehicle pitch was just short of 45 degrees.

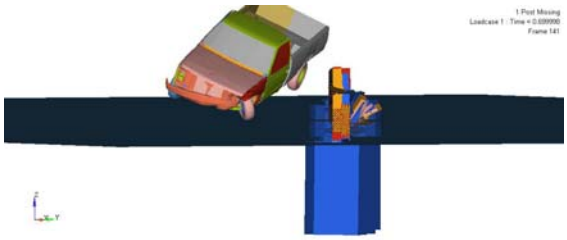

Figure 32: 1 post missing simulation. Impact point was mid-span. t = 0.7s

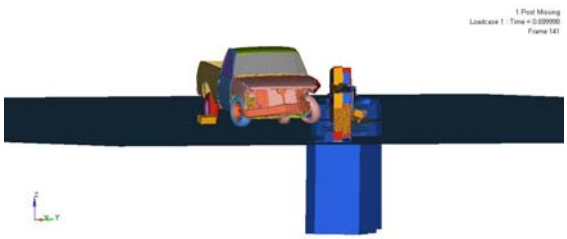

Figure 33: 1 post missing simulation. Impact point was beginning of unsupported span. t = 0.7s

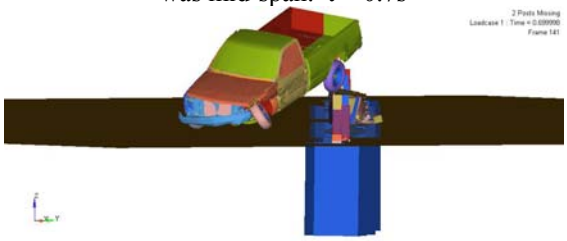

Figure 34: 2 posts missing simulation. Impact point was mid-span. t = 0.7s

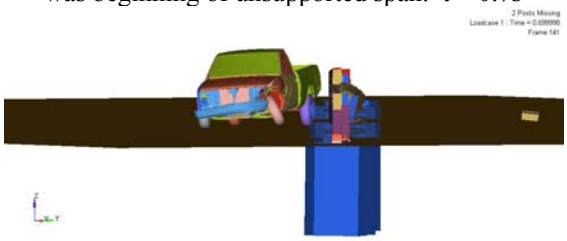

Figure 35: 2 posts missing simulation. Impact point was beginning of unsupported span. t = 0.7s

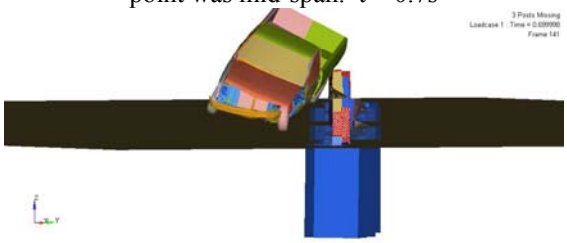

Figure 36: 3 posts missing simulation. Impact point was mid-span. t = 0.7s

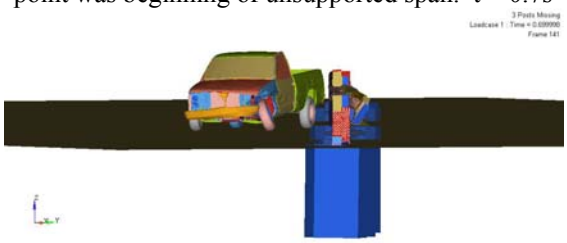

Figure 37: 3 posts missing simulation. Impact point was beginning of unsupported span. t = 0.7s

The results for missing post simulations in which the impact point was mid-span are summarized in Table 14. This table also contains the results of a simulated impact into

undamaged guardrail (i.e. no posts missing) for reference. The percentage changes from the undamaged simulation are shown in Table 15. For the vehicle, the exit speed was related to the number of missing posts, with the exit speed decreasing sharply for each additional post missing. The guardrail dynamic deflection also increased as more posts were removed. This was an expected result as much of the lateral stiffness of the guardrail system is provided by the strong posts. For three posts missing, the dynamic deflection increased by a little over 50%. The occupant kinematics, such as ridedown and impact velocities, varied between simulations but did not show any clear trend.

Table 14: Results for missing post simulations where impact point was the center of the unsupported span

		Undamaged	1 Post Missing	2 Post Missing	3 Post Missing
Impact Conditions					
	Speed (kph)	100	100	100	100
	Angle (deg)	25	25	25	25
Exit Conditions					
	Speed (kph)	53	60	47	32
	Angle (deg)	14.5	20.9	29.4	13.3
Occupant					
	Impact Velocity X (m/s)	7.51	7.55	6.81	7.63
	Impact Velocity Y (m/s)	5.54	5.56	3.65	3.56
	Ridedown X (G)	-11.77	-9.50	-13.98	-12.88
	Ridedown Y (G)	-12.27	-9.02	-9.87	-9.71
	50 ms Average X (G)	-6.68	-6.67	-8.11	-8.52
	50 ms Average Y (G)	-6.82	-6.10	-7.00	-6.44
	50 ms Average Z (G)	-3.85	4.29	-3.18	-6.73
Guardrail Deflections					
	Dynamic (m)	0.69	0.86	0.97	1.05
	Static (m)	0.55	0.71	0.78	0.60
Vehicle Rotations					
	Max Roll (deg)	-14.4	-15.4	-13.2	-19.4
	Max Pitch (deg)	-9.9	-44.6	-17.8	-23.4
	Max Yaw (deg)	40.3	44	78.8	40

Table 15: % change for missing post simulations where impact point was the center of the unsupported span

		1 Post Missing	2 Post Missing	3 Post Missing
Impact Conditions				
	Speed (kph)	0.0%	0.0%	0.0%
	Angle (deg)	0.0%	0.0%	0.0%
Exit Conditions				
	Speed (kph)	13.2%	-11.3%	-39.6%
	Angle (deg)	43.6%	102.8%	-8.6%
Occupant				
	Impact Velocity X (m/s)	0.5%	-9.4%	1.7%
	Impact Velocity Y (m/s)	0.5%	-34.1%	-35.7%
	Ridedown X (G)	-19.3%	18.8%	9.5%
	Ridedown Y (G)	-26.5%	-19.6%	-20.9%
	50 ms Average X (G)	-0.1%	21.4%	27.5%
	50 ms Average Y (G)	-10.6%	2.6%	-5.6%
	50 ms Average Z (G)	11.3%	-17.3%	74.7%
Guardrail Deflections				
	Dynamic (m)	24.2%	40.8%	52.7%
	Static (m)	28.4%	41.3%	9.6%
Vehicle Rotations				
	Max Roll (deg)	6.9%	-8.3%	34.7%
	Max Pitch (deg)	350.5%	79.8%	136.4%
	Max Yaw (deg)	9.2%	95.5%	-0.7%

In Table 16 and Table 17, the results for the missing post simulations for which the point of impact was the beginning of the unsupported span are presented. The results were quite different from the results of the previously discussed missing post simulations.

Table 16: Results for missing post simulations with impact point at the beginning of the unsupported span

	Undamaged	1 Post Missing	2 Post Missing	3 Post Missing
Impact Conditions				
Speed (kph)	100	100	100	100
Angle (deg)	25	25	25	25
Exit Conditions				
Speed (kph)	53	39	57	63
Angle (deg)	14.5	-11.5	11.4	15.3
Occupant				
Impact Velocity X (m/s)	7.51	8.88	7.53	6.51
Impact Velocity Y (m/s)	5.54	5.81	5.75	5.48
Ridedown X (G)	-11.77	-9.10	-12.13	-10.22
Ridedown Y (G)	-12.27	-10.08	-8.89	-10.30
50 ms Average X (G)	-6.68	-7.93	-6.37	-6.32
50 ms Average Y (G)	-6.82	-6.76	-6.75	-7.27
50 ms Average Z (G)	-3.85	-4.82	3.21	1.71
Guardrail Deflections				
Dynamic (m)	0.69	0.78	0.89	1.00
Static (m)	0.55	0.51	0.68	0.70
Vehicle Rotations				
Max Roll (deg)	-14.4	-7.6	-7.8	-6.5
Max Pitch (deg)	-9.9	-7.6	-6.9	2
Max Yaw (deg)	40.3	23.8	37	40

Like the previous simulations, there was a noticeable increase in dynamic deflection for each post that was removed from the system. The increase in deflection was slightly lower, indicating that the beginning of the span was not the point of impact that maximized the total deflection of the system.

There were some definitive trends that appeared in the vehicle exit speed, occupant impact velocities and the 50 ms X acceleration. For all of these criteria, the highest value was observed for one missing post. Subsequently, all values dropped as more posts were removed from the system, with the lowest values occurring when three posts were removed. This effect was attributed to the decrease of interaction between the vehicle and the posts. Because the vehicle was interacting primarily with the rails, the redirection of the vehicle, and the resulting

occupant forces, would have been smoother. As more posts were removed, the vehicle was impacting its first post at a lower speed, and as a result the forces that developed due to the wheel assembly hitting the posts were lower.

Table 17: % Change for missing post simulations with impact point at beginning of the unsupported span

		1 Post Missing	2 Post Missing	3 Post Missing
Impact Conditions				
	Speed (kph)	0.0%	0.0%	0.0%
	Angle (deg)	0.0%	0.0%	0.0%
Exit Conditions				
	Speed (kph)	-26.4%	7.5%	18.9%
	Angle (deg)	-179.2%	-21.4%	5.5%
Occupant				
	Impact Velocity X (m/s)	18.2%	0.3%	-13.2%
	Impact Velocity Y (m/s)	4.9%	3.9%	-1.1%
	Ridedown X (G)	-22.6%	3.0%	-13.2%
	Ridedown Y (G)	-17.9%	-27.6%	-16.0%
	50 ms Average X (G)	18.7%	-4.7%	-5.5%
	50 ms Average Y (G)	-0.9%	-1.1%	6.5%
	50 ms Average Z (G)	25.3%	-16.7%	-55.7%
Guardrail Deflections				
	Dynamic (m)	12.7%	29.3%	44.9%
	Static (m)	-8.2%	24.0%	27.1%
Vehicle Rotations				
	Max Roll (deg)	-47.2%	-45.8%	-54.9%
	Max Pitch (deg)	-23.2%	-30.3%	-79.8%
	Max Yaw (deg)	-40.9%	-8.2%	-0.7%

Surprisingly, the exit speed of the vehicle actually increased as the number of posts removed from the system was increased. The most likely explanation for this was that the interactions between the vehicle tire and suspension and the guardrail posts was eliminated. This was, however, in direct opposition of the results observed for the three simulations were the impact point was at the middle of the unsupported span.

To explore the possible causes of this difference, the distance between the vehicle's point of impact and the first downstream post was tabulated (see Table 18). The distances to the first post for a 3 post missing system struck mid-span and a 1 post missing system struck at the

beginning were exactly the same. In this light, the similarity in exit speeds between these simulations was not as troublesome as previously thought.

The vehicle exit speeds were cross-plotted with the distance to the first downstream post in Figure 38. The resulting plot shows that the vehicle exit speed reaches a minimum when the distance to the post is roughly 3.8 meters and the exit speed increases as the distance to the first post deviates from this value. Thus, a distance of 3.8 meters between the impact point and the first downstream post was the distance for which the vehicle-post interaction was maximized. For smaller distances, the vehicle was observed to glance off the edges of the posts or to override the deformed posts. For larger distances, the vehicle's energy would be greatly diminished by the time the vehicle encounters its first post. For sufficiently large spans, the vehicle would not interact with any posts at all.

Table 18: Distance between impact point and first downstream post

	Undamaged	**1 Post Missing**	**2 Posts Missing**	**3 Posts Missing**
Center of Span	1905 mm	1905 mm	2857.5 mm	3810 mm
Beginning of Span		3810 mm	5715 mm	7620 mm

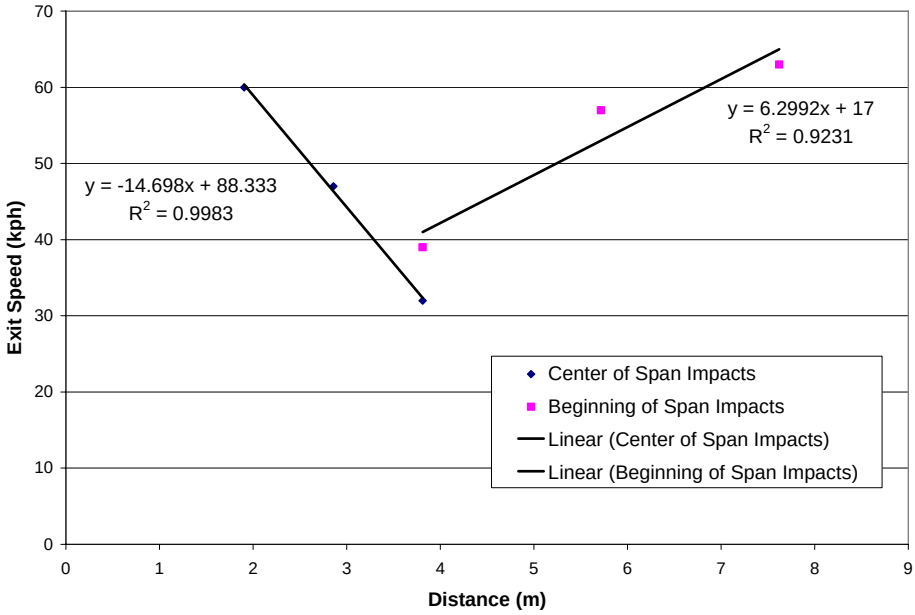

Figure 38: Relationship between the vehicle exit speed and the distance from the point of impact to the first downstream post

The deflection (both static and maximum dynamic) contours are shown below in Figures 40 - 45. For most of the simulations, the point of maximum deflection typically occurs around 0.2 seconds. At this time, the vehicle was just beginning to turn due to contact with the rails. As would be expected, the dynamic deflection increased as more posts were removed from the system. For the 3 posts missing simulation, the guardrail deflection exceeded that of the UNL validation simulation (Figure 24), which was also missing three posts. However, the UNL test made use of nested guardrail to reduce the deflection, so this was not unexpected. The static deflection varied greatly between simulations. This was partly due to twisting in the rails, but also because of the manner in which the vehicle exited the guardrail. For the one and two post missing simulations, the snagging of the vehicle tires on the posts caused the vehicle to slide away from the rails. In the undamaged and three post missing simulations, the vehicle remained in contact with the rails longer which caused the damage contour to smooth out more.

Because of the coarse sampling, the damage contours do not accurately represent the maximum static or dynamic deflection. However, the contours are useful for observing the shape of the guardrail during the time of maximum deflection. The contours shown all begin at that same point (starting at post 9). The deflection was sampled roughly every 953 mm until post 21 was reached. The total length sampled was just under 23 meters.

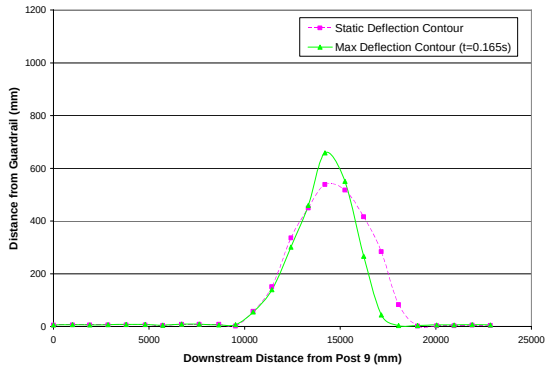

Figure 39: Guardrail deflection for undamaged guardrail simulation

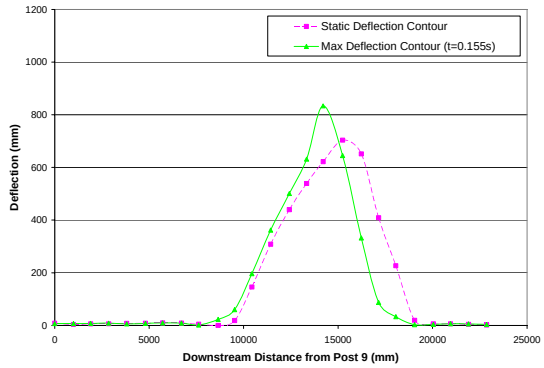

Figure 40: Guardrail deflection for mid-span impact, 1 post missing simulation

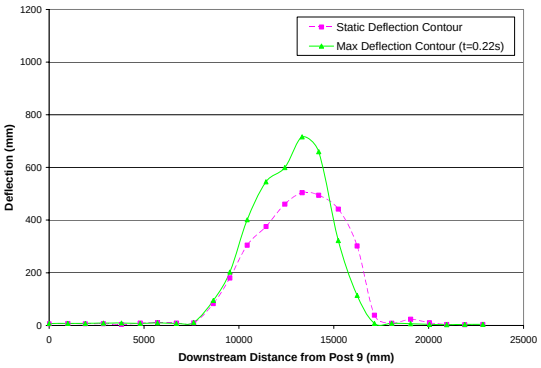

Figure 41: Guardrail deflection for beginning of span impact, 1 post missing simulation

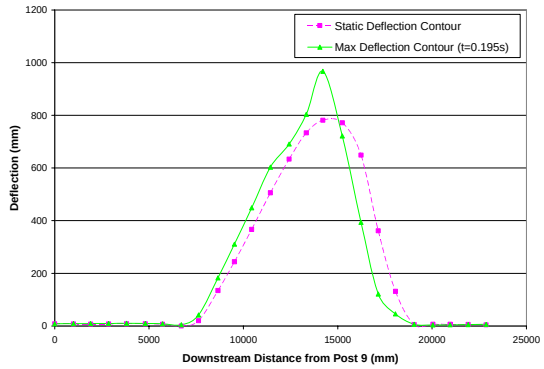

Figure 42: Guardrail deflection for mid-span impact, 2 posts missing simulation

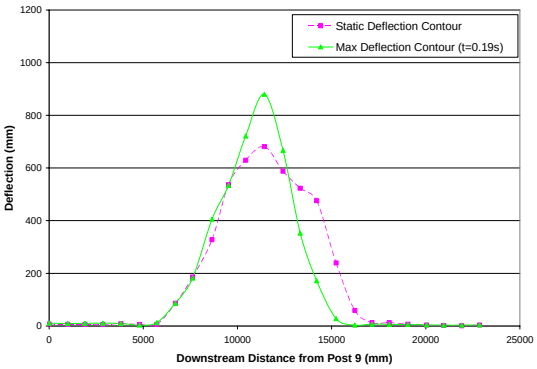

Figure 43: Guardrail deflection for beginning of span impact, 2 posts missing simulation

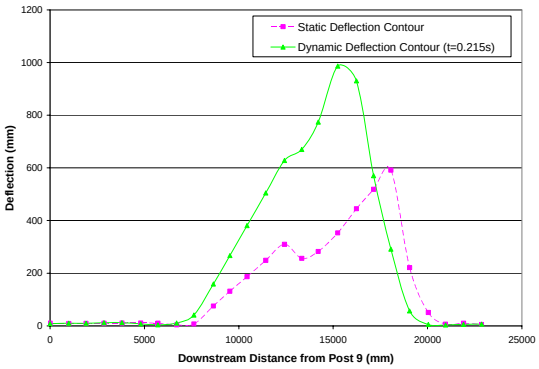

Figure 44: Guardrail deflection for mid-span impact, 3 posts missing simulation

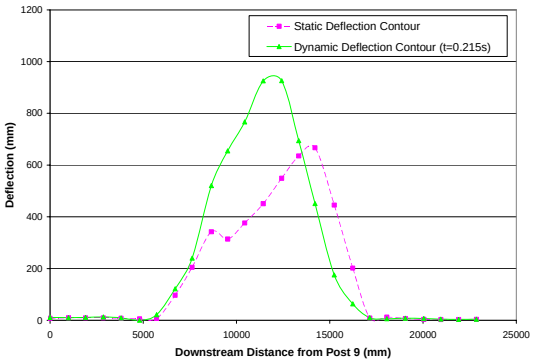

Figure 45: Guardrail deflection for beginning of span impact, 3 posts missing simulation

Figures 46 - 52 show the vehicle velocity for each simulation. All velocities were reported in the vehicle local coordinate system. Not all of the simulated vehicles reached a constant velocity after leaving the guardrail. In these cases, the velocity that was selected to be the exit speed was sampled at roughly 0.7 seconds. The magnitude of the Y and Z velocity components tended to be the highest for the simulations where there was a short distance between the point of impact and the first downstream post. This was attributed to the front left tire snagging on the downstream posts.

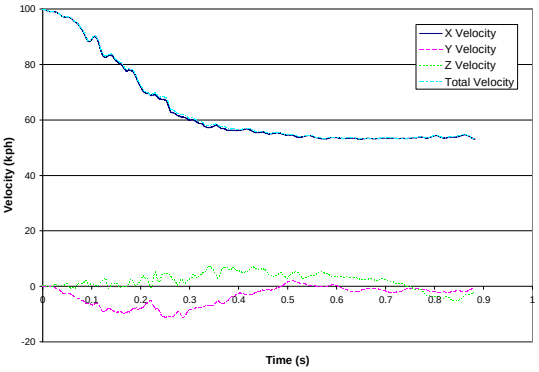

Figure 46: Vehicle CG velocity for undamaged guardrail simulation

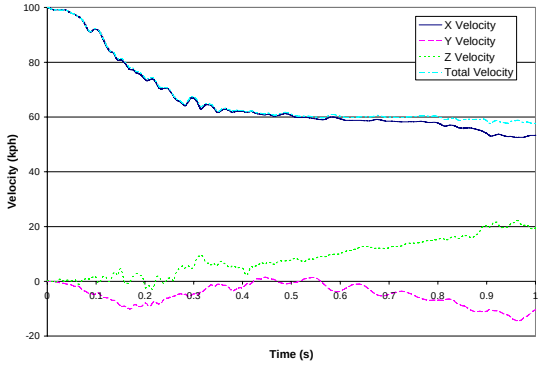

Figure 47: Vehicle CG velocity for mid-span impact, 1 post missing simulation

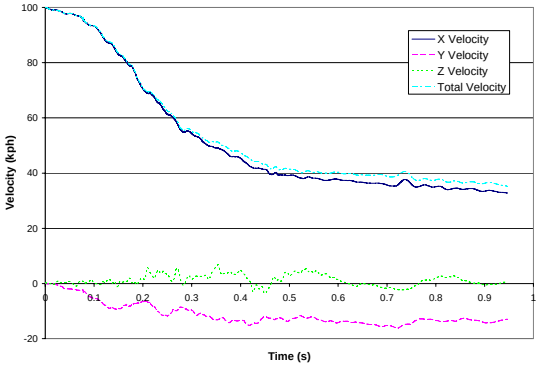

Figure 48: Vehicle CG velocity for beginning of span impact, 1 post missing simulation

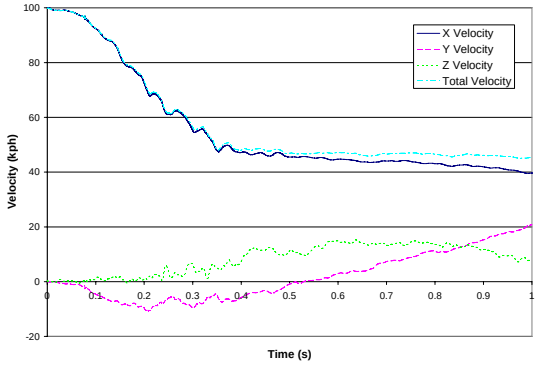

Figure 49: Vehicle CG velocity for mid-span impact, 2 posts missing simulation

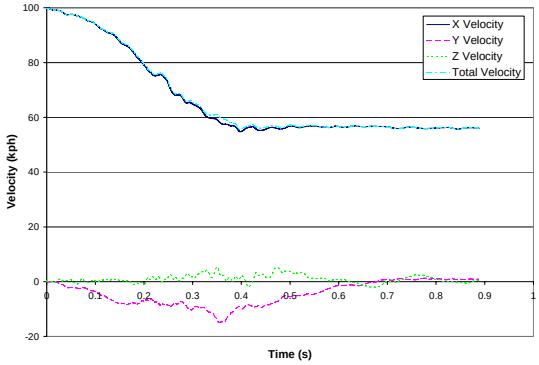

Figure 50: Vehicle CG velocity for beginning of span impact, 2 posts missing simulation

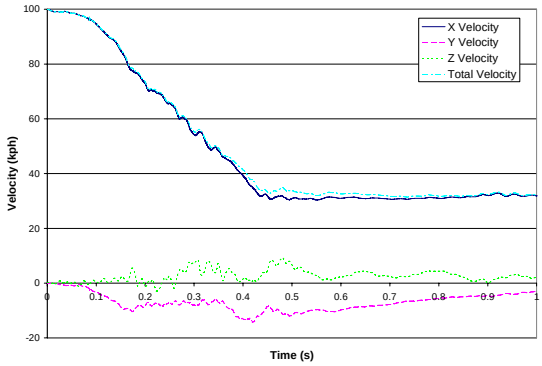

Figure 51: Vehicle CG velocity for mid-span impact, 3 posts missing simulation

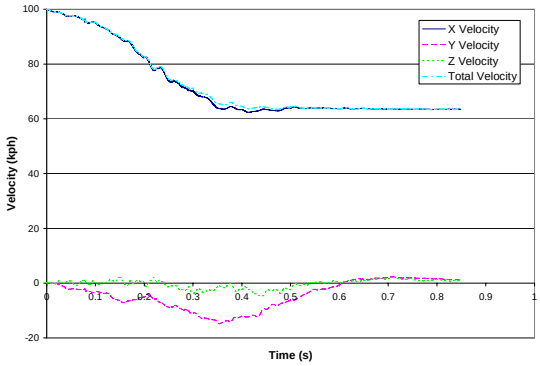

Figure 52: Vehicle CG velocity for beginning of span impact, 3 posts missing simulation

Figures 53 - 59 show the vehicle rotation (roll, pitch, and yaw) for the missing post simulations. All the data was reported with respect to the local vehicle axes. The single post missing simulation, with the impact at mid-span, showed the most severe vehicle rotations, with the pitch leveling at approximately -45 degrees. The simulations with a longer distance to the first downstream post showed the lowest degrees of roll and pitch. Thus, it would be expected

that the interactions between the vehicle tire and the posts would be the most significant contributor to unfavorable vehicle rotations.

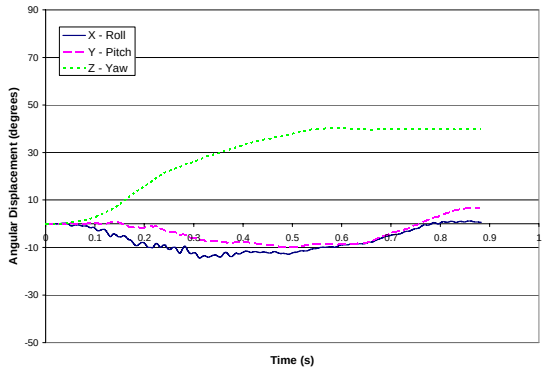

Figure 53: Vehicle CG rotation for undamaged guardrail simulation

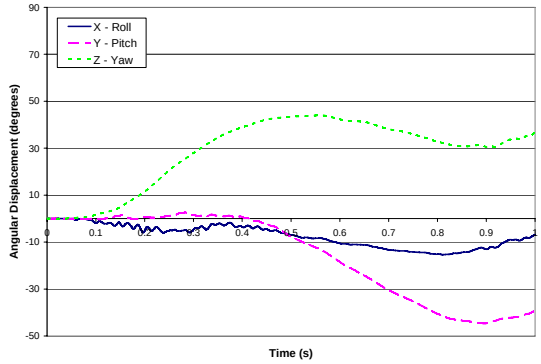

Figure 54: Vehicle CG rotation for mid-span impact, 1 post missing simulation

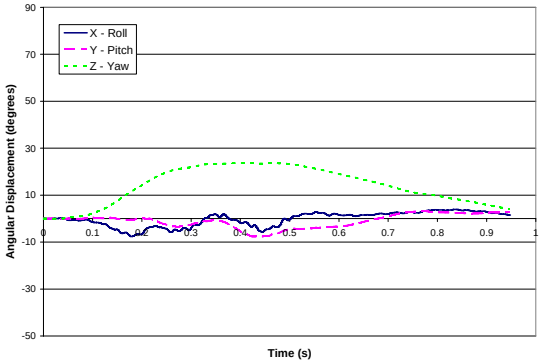

Figure 55: Vehicle CG rotation for beginning of span impact, 1 post missing simulation

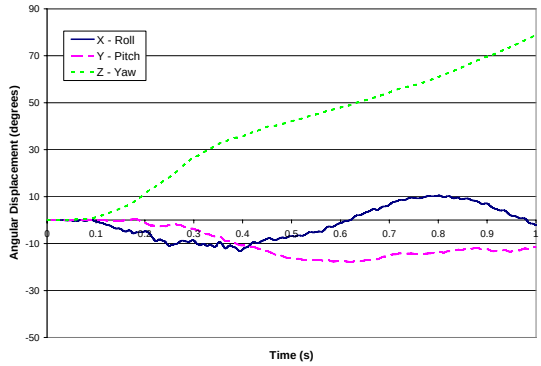

Figure 56: Vehicle CG rotation for mid-span impact, 2 posts missing simulation

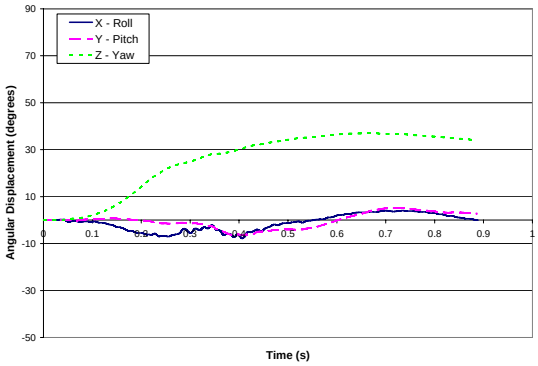

Figure 57: Vehicle CG rotation for beginning of span impact, 2 posts missing simulation

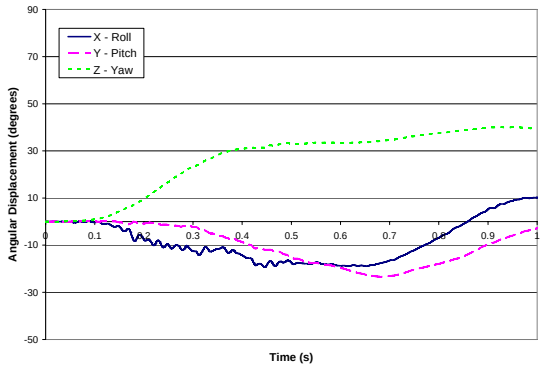

Figure 58: Vehicle CG rotation for mid-span impact, 3 posts missing simulation

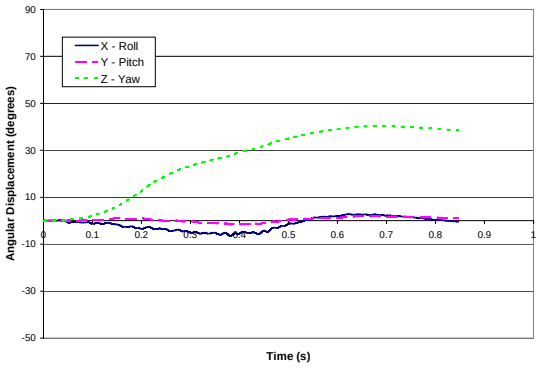

Figure 59: Vehicle CG rotation for beginning of span impact, 3 posts missing simulation

The plots below (Figure 61 - Figure 66) show the simulation energies as reported by LS-DYNA. These energy balances were useful in identifying unrealistic behavior in the model, such as unexplained energy sources and sinks. The presence of sudden spikes in energy was another indicator of instability, usually a contact problem resulting in nodes "sticking" to the guardrail and arresting the vehicle.

All of the simulations were very consistent for total energy, with the largest change being a 1.6% decrease for the simulation of one missing post struck mid-span. Kinetic energy and potential energy (energy absorbed in deformation of the vehicle and guardrail) represented more than 80% of the total energy at the end of the simulation. The other major contributors to the total energy were the hourglass energy and the interface energy.

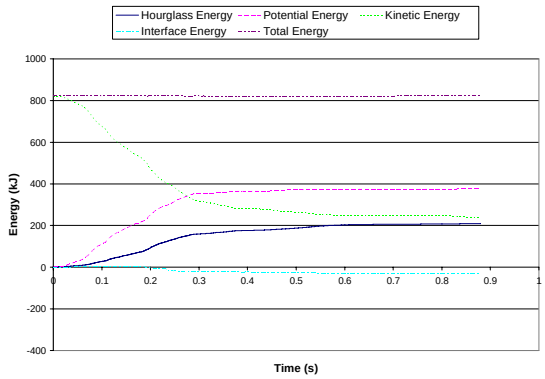

Figure 60: Simulation energy balance for undamaged guardrail simulation

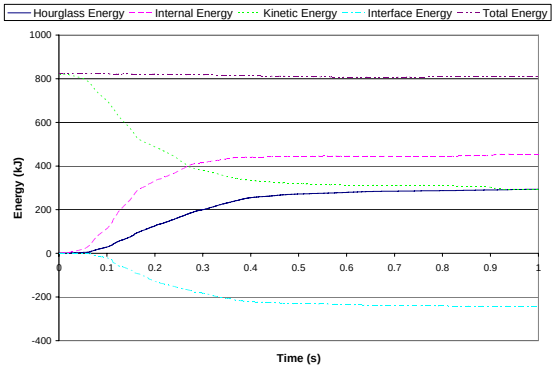

Figure 61: Simulation energy balance for mid-span impact, 1 post missing simulation

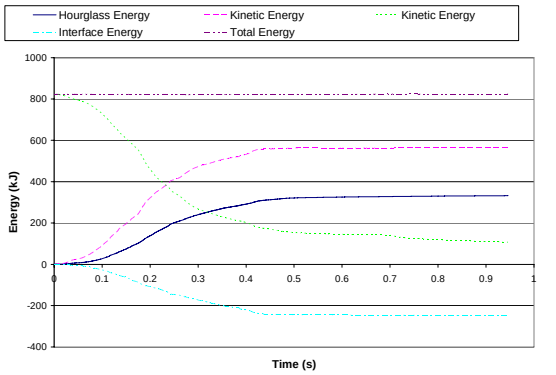

Figure 62: Simulation energy balance for beginning of span impact, 1 post missing simulation

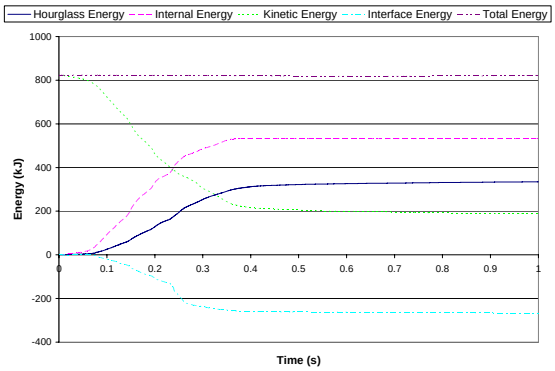

Figure 63: Simulation energy balance for mid-span impact, 2 posts missing simulation

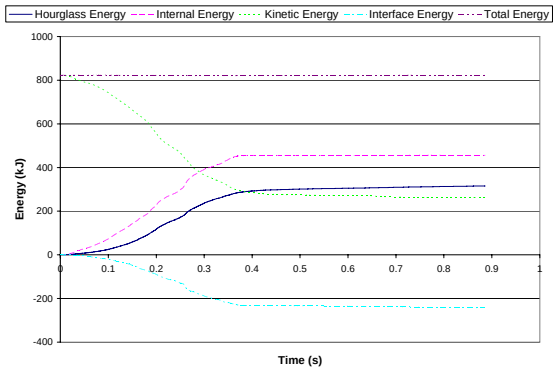

Figure 64: Simulation energy balance for beginning of span impact, 2 posts missing simulation

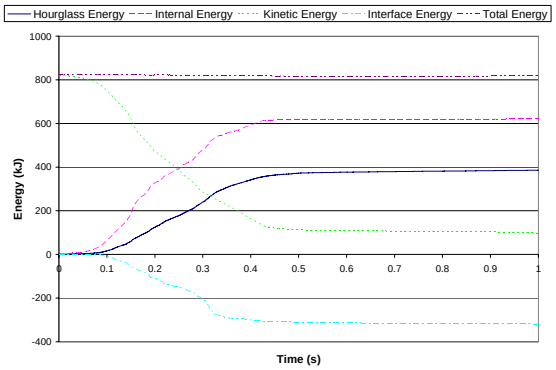

Figure 65: Simulation energy balance for mid-span impact, 3 posts missing simulation

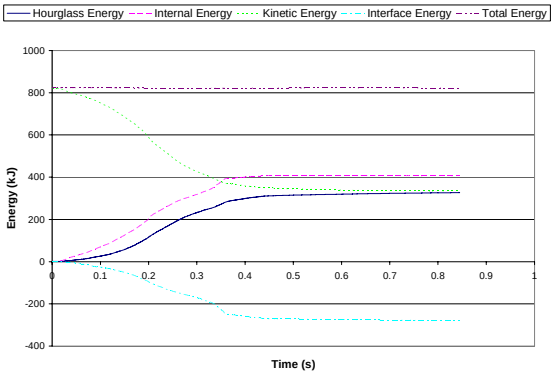

Figure 66: Simulation energy balance for beginning of span impact, 3 posts missing simulation

5.3.3 Evaluation of Rail Rupture Potential via Stress and Strain

The previous section focused on whether missing posts adversely affected the vehicle stability. Another potential failure mode was rail rupture. With each additional missing post, the rails were forced to absorb more of the crash energy, leading to increased deflection. At some point, the maximum tensile capacity of the rail would be exceeded and a rail rupture would occur. However, the failure of the guardrail steel cannot be reproduced with the large elements used in the finite element model. Even though the failure cannot be modeled, the stress and strain data in the rails can be observed to provide insight into how the removal of posts from a system affects the stress and strain during impact.

To evaluate how the stress varied with the number of missing posts, the stress contours of four sections of rail in the area of impact were examined. The number of elements in these rail sections that exceeded a threshold value of 400 MPa (hereafter called a stressed element) was recorded. The number of elements was tabulated between 40 and 250 ms, in 10 ms intervals, and then up to 700 ms at 50 ms intervals. The resulting data was plotted in Figure 68 below. Most of the simulations reached a maximum value around 0.2 seconds. The number of stressed elements in the one missing post simulation peaked at 120 ms, but the number of elements at 200

ms was only slightly lower than this peak value. The contours for each simulation at the time for maximum number of elements is shown in Figure 69 - Figure 72.

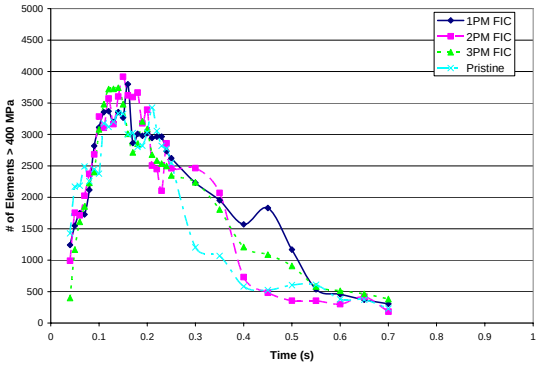

Figure 67: Stressed elements for simulations with mid-span impacts

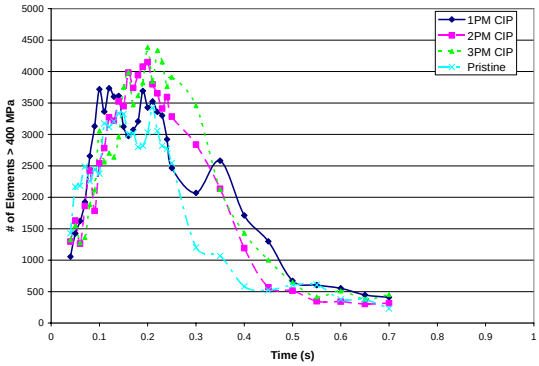

Figure 68: Stressed elements for simulations with beginning of span impacts

Figure 67 above shows the number of elements over 400 MPa for the series of simulations with a mid-span impact. While there was no clear pattern that emerged relating the number of posts to the number of elements above 400 MPa, all of the missing post simulations contained more stressed elements than that of the undamaged simulation. The greatest increase was for the two posts missing simulation at 14.4%. The lowest increase was 9.2% for three missing posts.

The results in Figure 68 were intriguing because there was a trend for the maximum number of elements exceeding the stress threshold value to increase as the number of posts missing was increased. The undamaged simulation had the fewest elements exceeding the threshold at peak, confirming the expectation that the undamaged guardrail was the least likely to rupture. Each post that was removed from the simulations resulted in an increase in the maximum number of elements over 400 MPa. The increase between the one post missing simulation and two posts missing simulation was the largest at 11.1% and the increase between

two and three missing posts was the smallest at 5.7%. The one post missing simulation resulted in a 9.0% increase over the undamaged simulation.

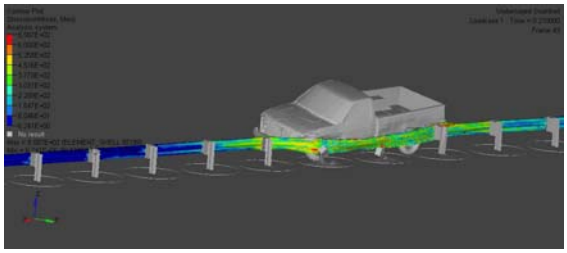

Figure 69: Maximum stress contour for undamaged guardrail at 210 ms

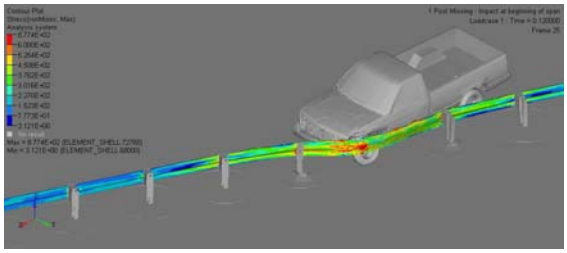

Figure 70: Maximum stress contour for 1 post missing simulation at 120 ms

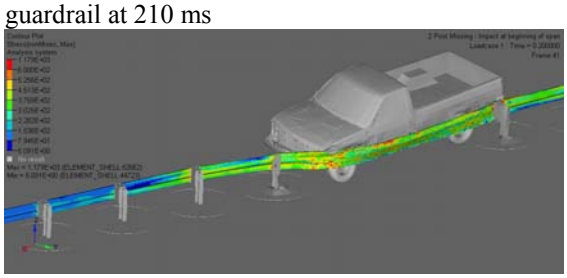

Figure 71: Maximum stress contour for 2 posts missing simulation at 200 ms

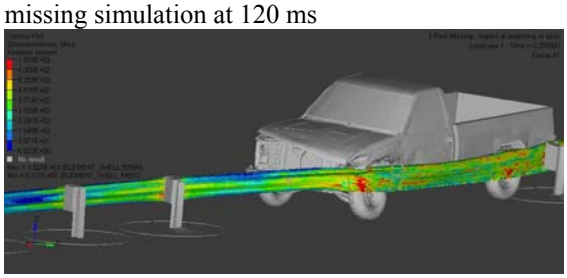

Figure 72: Maximum stress contour for 3 posts missing simulation at 200 ms

5.3.4 Evaluation of Rail Rupture Potential via Tension Force

The information that could be obtained from the stress in the rail elements was limited, both because the stress threshold was arbitrary and because the expected increase in stress was not observed for the series of mid-span impacts. Another way to look at the possibility of rail rupture was to examine the tension carried by the rails during the crash.

Figure 73 shows the rail tensions through the rail cross section at various locations on the guardrail. The tension was measured across a vertical slice through each rail according to the procedures that were detailed in the Methods section. Although the rail tension data was noisy, there were clearly observed increases in the rail tension as the number of posts removed from the system increased. Unlike the results for the stress analysis, the trend of increasing rail tension applied to both of the impact locations.

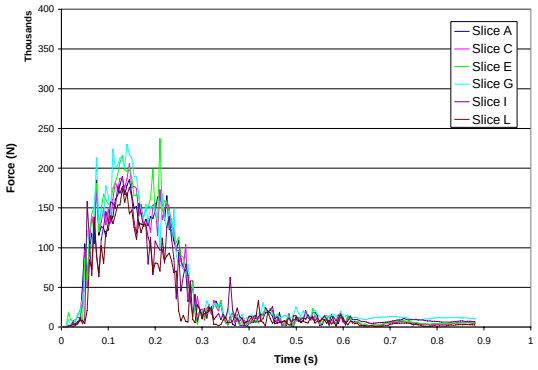

Undamaged

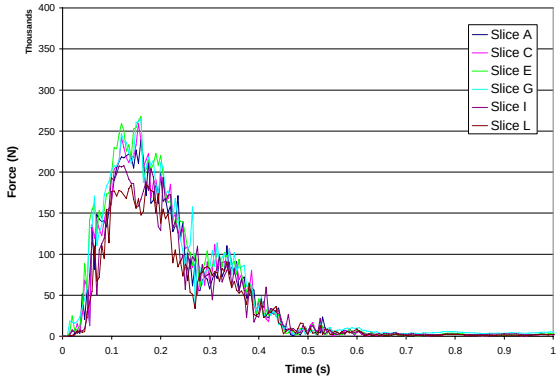

1 post missing, mid-span impact

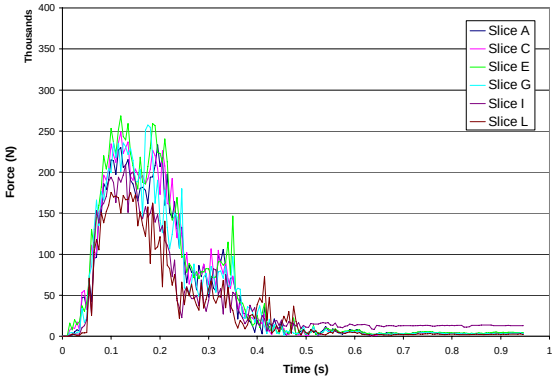

1 post missing, beginning of span impact

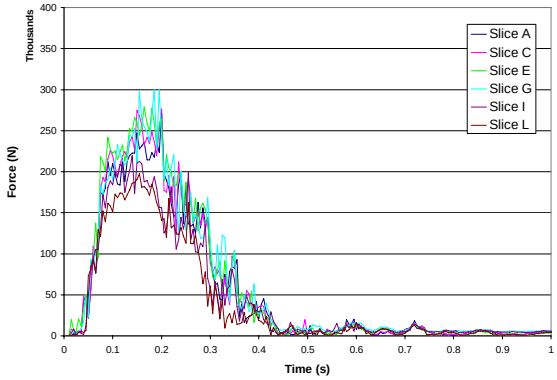

2 posts missing, mid-span impact

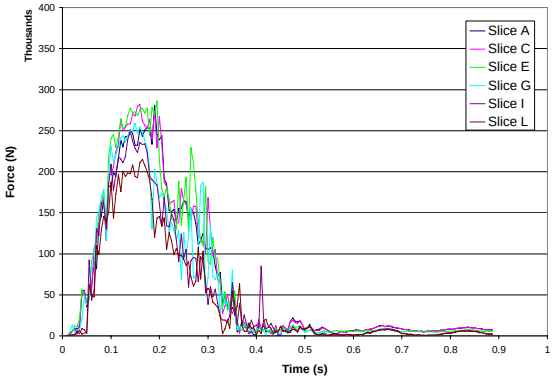

2 posts missing, beginning of span impact

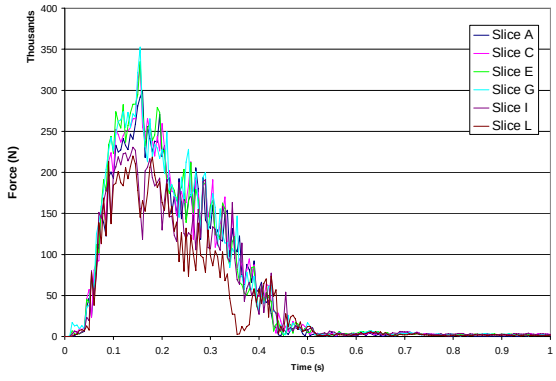

3 posts missing, mid-span impact

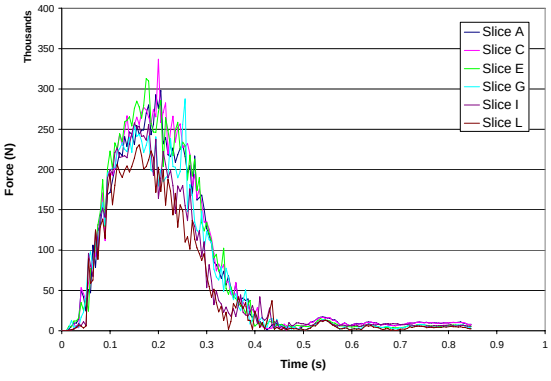

3 posts missing, beginning of span impact

Figure 73: Magnitude of rail tension in multiple cross section slices

In Table 19, the maximum observed tensions for each of the missing post simulations is tabulated along with the percent increase over the simulation of the undamaged guardrail. For each additional post removed from the guardrail system, the maximum tension in the rail increased by 20 – 50 kN. The maximum tension observed was 352.8 kN for the guardrail missing three posts and impacted by the pickup truck at the middle of the unsupported span. This was almost a 50% increase in rail tension compared to the undamaged simulation, where the maximum tension recorded was 237.4 kN.

Table 19: Maximum rail tensions in simulations of missing post guardrails

	Maximum Rail Tension (kN)		**% Increase Over Undamaged**	
	Beginning of Span	Mid-span	Beginning of Span	Mid-span
Undamaged	237.4		0.0%	
1 Post Missing	268.4	267.5	13.1%	12.7%
2 Posts Missing	286.2	299.8	20.6%	26.3%
3 Posts Missing	336.7	352.8	41.9%	48.6%

While the increase in rail tension as posts were removed was large, the maximum tension observed in the simulations was still below the quasistatic tension limit of 410 kN. However, this did not necessarily mean that rail rupture could not occur, as previous research has shown that rail rupture typically occurs at much lower rail tensions that can be reached in quasistatic testing [11]. This has been attributed to the development of high localized stresses around the splices. Taking the results of the rail tension analysis and the stress analysis together, the likelihood of the rails rupturing during impact increased as more posts were removed.

5.4 Conclusions

The simulation of vehicle collisions with guardrail systems missing posts demonstrated that there was an increased risk of vehicle instability. While none of the vehicles in the

simulations overturned, there were several that were close to rolling over. Some of the vehicles exhibited significant skidding upon exiting the system, and these vehicles would be easily tripped by irregularities in the ground.

The removal of even one post can be expected to increase the system deflection by as much as 25%. Further increases in deflection and stress were expected as more and more posts were removed from the system. The most severe condition simulated (three posts missing) resulted in a 50% increase in the maximum deflection of the guardrail. Therefore, it would be especially important to repair missing posts whenever there is a substantial crash risk immediately behind the barrier.

One aspect of the study was the consideration of the impact point on the simulation results. Each missing post condition was simulated twice, with one impact point at the center of the unsupported span and the other impacting at the beginning of the unsupported span. The results of the simulations did not depend on the impact point per se, but rather on the length of rail between the impact point and the first downstream post. Thus, the results for a system missing one post and struck at the beginning of the span were comparable to the results of a three post missing system struck mid-span. The interactions between the vehicle and the posts were maximized when the impact point was 3.8 meters upstream, regardless of number of posts missing from the system.

The stress in the guardrails was considered as an indicator of whether the missing post systems would be more likely to rupture. It was found that the number of elements in the simulation that exceeded a threshold stress limit of 400 MPa increased as the number of missing posts increased for the simulations where the impact point was the beginning of the unsupported span. Removing even one post resulted in an 11.8% increase in the number of elements over this

value. However, the simulations with the impact point at the middle of the unsupported span did not show increased stress as more posts were removed, although all of the missing post simulations recorded higher stresses than the undamaged simulation.

Rail tension was also considered as a possible predictor of rail rupture. Unlike the stress analysis, the rail tension clearly increased as posts were removed from the system for both of the impact points used in the simulations. With three posts missing from the system, the tension was increased by nearly 50%, but was still below the quasistatic failure limit of 410 kN. However, rail ruptures have been observed in crash test at much lower tensions than can be reached at quasistatic loading due to localized stresses around the splices. Thus, it was likely that the increased rail tension, combined with the higher stresses, would lead to increased chances of the rail rupturing during impact.

5.5 Recommendation for Missing Posts

It is recommended that maintenance crews repair any strong-post w-beam systems that are missing any number of posts. Impacts into guardrail systems missing posts were found to have a higher risk of vehicle instability, greater maximum guardrail deflection, and an increased risk of rail rupture.

6. RAIL AND POST DEFLECTION MODELS

6.1 Introduction

Crash-induced deflection in a strong-post w-beam guardrail was the damage mode of greatest interest to transportation agencies in the U.S and Canada [5, 15]. Three damage modes, rail and post deflection over 6 inches, rail deflection without post deflection, and rail and post deflection less than 6 inches, were ranked 1st through 3rd respectively as modes of damage most likely to compromise the functionality of the guardrail. These damage modes were also the most commonly observed types of minor damage in the field.

6.2 Methods

6.2.1 Reproducing the MGA Crash Test

As part of a larger study [5], two full-scale crash tests were performed to evaluate the performance of damaged guardrail. These tests were performed by the MGA Research Corporation during August 2008 [16, 17]. The goal of these crash tests was to observe how pre-existing rail and post deflection would affect the crash test results. The first crash test was a low speed impact of a Chevrolet 2500 pickup into an undamaged guardrail. The initial speed for this first impact was 48.3 kph (30 mph) at 26 degrees. The result of the crash, shown in the top row of Figure 74, was a maximum of 369 mm (14.5 inches) of static guardrail deflection. None of the posts were separated from the rails as a result of the first impact.

A second impact, performed according to NCHRP 350 test level 3 conditions (i.e. 100 kph at 25 degrees) was prepared. For this impact, another Chevrolet 2500 pickup truck would impact the damaged guardrail at the same location as the previous vehicle. The vehicle initial conditions were 99.9 kph at 26 degrees. This second test resulted in the vehicle vaulting, along with significant deflection to the guardrail. The vehicle's direction of travel was not significantly altered before the vaulting occurred. Posts 8, 10-12, and 14 were separated from the rail as a result of the impact, but post 13 remained attached to the rail.

Figure 74: MGA Crash Test C08C3-027.1 after installation (top left) and after the first, low speed impact (top right) [16]. The following day, the guardrail was prepared for MGA Crash Test C08C3-027.2 (bottom left) which resulted in the vehicle vaulting and further damage to the guardrail (bottom right) [17].

To further validate the finite element model, the MGA crash tests were reproduced using the finite element model. Like the real crash test, this model was developed as two separate parts. The first model was developed to reproduce the initial damage to the guardrail in the first,

low-speed impact and the second model was used to predict the outcome of the second, test level 3 impact.

To model the MGA crash tests, the finite element model needed to be altered to match the guardrail installation that was used for the test. The MGA guardrail setup is shown in Figure 75. The MGA guardrail contained 27 posts and the rails were overlapped in such a way that the right side of the vehicle would strike the guardrail. In contrast, the finite element model used for this study contained 29 posts and was oriented so that the left side of the vehicle would strike the guardrail.

The finite element model was altered by both the removal of two posts and by the reversal of the rail direction to match the setup for the MGA crash test. The initial impact was also adjusted so that the front right corner of the vehicle would impact the guardrail at post 11. In the MGA test, the guardrail was installed in a relatively narrow slot in the concrete surface. If the posts were to experience significant displacement at the ground level, the presence of the concrete edge could affect the outcome of the test. A representation of this concrete edge, made out of rigid elements, was added to the finite element model roughly 280 mm (11 inches) behind the back of the posts.

The final change made to the simulation was to modify the vehicle. The vehicle used in the MGA crash tests was much higher than the used in the TTI crash test and the simulation of undamaged guardrail. The bumper heights in particular were very different, with the front bumper of the MGA test vehicle being 45 mm higher and the rear bumper being 59 mm higher. Since the relative heights of the vehicle to the rail has already been shown to be a critical factor in determining crash outcome [8] it was necessary to accurately represent the vehicles used. The original and modified vehicle dimensions were shown in Table 2.

Figure 75: Guardrail for MGA crash tests [16]

The finite element model for the second impact was prepared by exporting the geometric data from the end of the first simulation and importing that geometry into the model of the second impact. The two simulations, before impact, are shown in Figure 76.

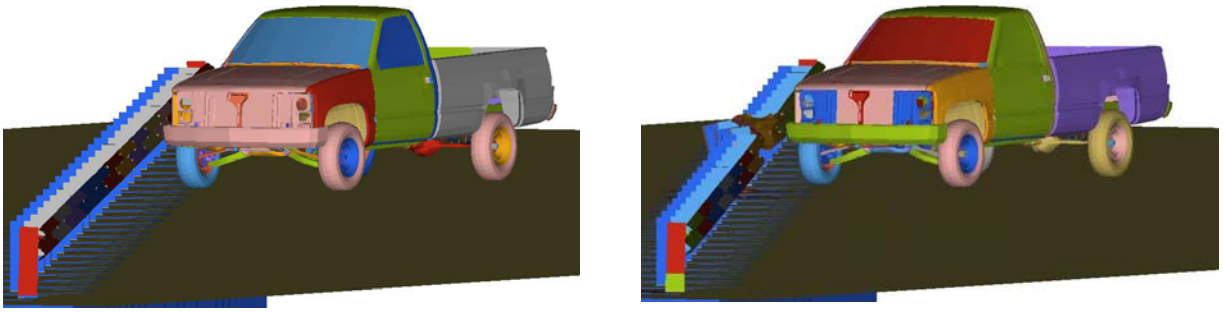

Figure 76: Finite element simulations of MGA crash tests. Before first impact (left) and after first but before second impact (right)

6.2.2 Creating controlled rail and post deflection

A combination of rail and post deflection was the most complex damage mode under consideration in this study. Additionally, a number of different damage extents were to be examined, ranging from 3 inches up to 11 inches. The desired damage extents (3 inches, 6

inches, 9 inches, and 11 inches) were produced by running the undamaged guardrail impact simulation with much lower speeds but at the same impact angle of 25 degrees to create the pre-existing damage, just like for the MGA test models discussed previously. The damage caused by these lower severity simulations would become the starting point for the full scale simulations at test level 3 conditions. These simulations were performed with the TTI crash test vehicle model instead of the MGA crash test model.

Because the speeds needed to reproduce the desired amount of rail and post deflection were not known, a series of simulations was conducted to correlate the impact speed with the resulting amount of damage. The simulation results are summarized in Table 20. The maximum static rail deflection for each simulation was recorded.

Table 20: Results of low speed simulations to cause minor damage

Initial Vehicle Speed (mm/s)	Initial Vehicle Speed (kph)	Static Max Rail Deflection (mm)	Static Max Rail Deflection (in)	Maximum Post Deflection (in)
8000	28.8	62	2.4	
8500	30.6	76	3.0	1.3
9000	32.4	106	4.2	
10000	36.0	152	6.0	1.6
10500	37.8	186	7.3	
12000	43.2	228	9.0	6.5
13500	48.6	266	10.5	
16000	57.6	275	10.8	13.5
17000	61.2	322	12.7	
19000	68.4	386	15.2	
27778	100.0	552	21.7	

The simulations successfully identified the initial velocities needed to produce 3, 6, and 9 inches of deflection to the guardrail. These speeds were 30.6 kph, 36 kph, and 43.2 kph respectively. For each of these simulations, the maximum static post deflection was also computed and was found to be less than the rail deflection. The initial vehicle speed and maximum rail and post deflection were plotted in Figure 77. The relationship between the two

was non-linear, most likely because the number of guardrail and vehicle parts involved in the impact increases as the impact speed went up. However, in the range of speeds that were simulated (28 – 100 kph) the data closely resembled a logarithmic curve ($R^2 > 0.98$).

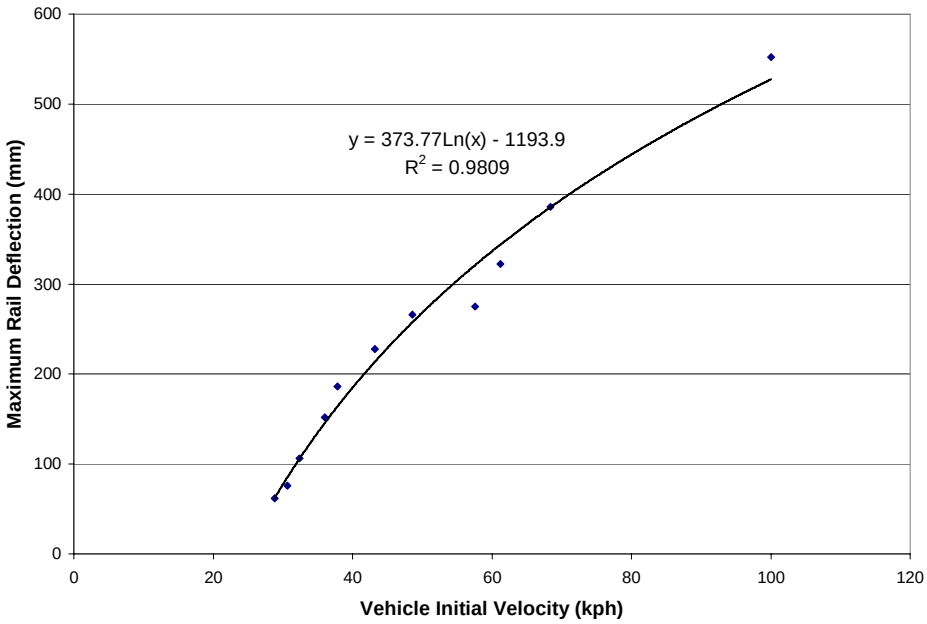

Figure 77: Relationship between initial vehicle speed and amount of rail and post deflection in the simulation for an impact angle of 25 degrees

The damaged geometry of the 3, 6, and 9 inch deflected guardrail was exported and incorporated into the undamaged simulation. The resulting finite element models (Figure 78) were then given initial conditions matching the NCHRP 350 test criteria, i.e. initial speed of 100 kph and an impact angle of 25 degrees.

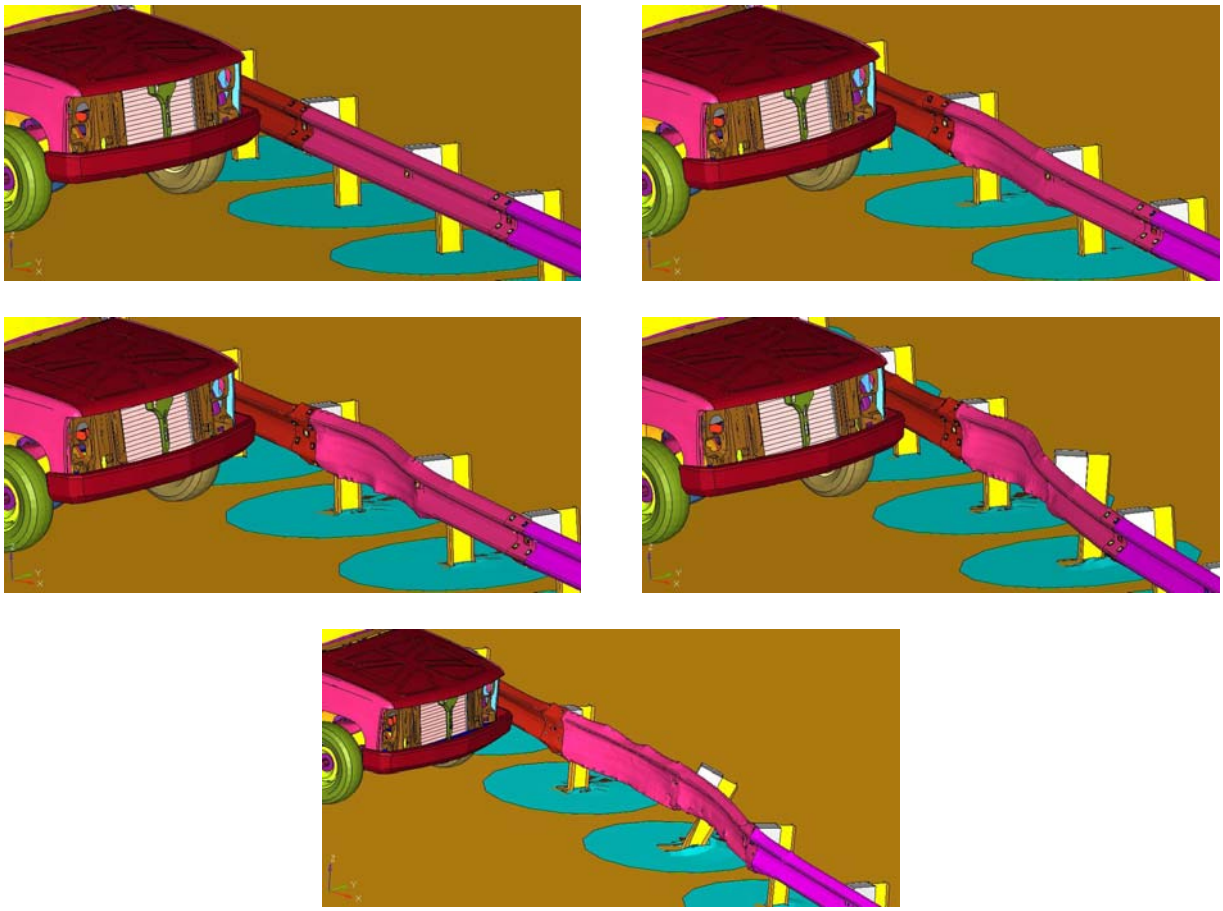

Figure 78: Guardrail simulations before second impact. Undamaged (top left), 3 inch (top right), 6 inch (middle left), 9 inch (middle right), and 11 inch (bottom).

6.2.3 Creating controlled rail only deflection

It was also necessary to perform two simulations for which only the rail was deflected by 3 inches and 6 inches. For these two simulations, the effects of the rail damage alone could be isolated. The extent of damage examined was lower for these simulations, because it believed that any higher amount of the deflection could not reasonably be expected to occur without also causing movement in the posts.

Rail only deflection was introduced into the finite element simulations by the same process that was described for combined rail and post deflection, except that some artificial constraints were added to the posts in the contact region. These constraints prevented all motion

of the posts, but allowed the rail to deform freely. The position of the guardrail was adjusted so that the area of impact was roughly 500 mm downstream of a post, rather than at the splice. This change both increased the amount of observed deflection and more closely represented the type of impact that would be likely to cause only rail deflection. The initial conditions for the vehicle used to create the desired amount of pre-existing damage are shown in Table 21. The resulting minor damage to the rails is shown in Figure 79.

Table 21: Initial conditions for rail deflection only simulations

Initial Vehicle Speed (mm/s)	Initial Vehicle Speed (kph)	Static Max Rail Deflection (mm)	Static Max Rail Deflection (in)	Maximum Post Deflection (in)
8000	28.8	78	3.1	0.0
10000	36.0	142	5.6	0.0

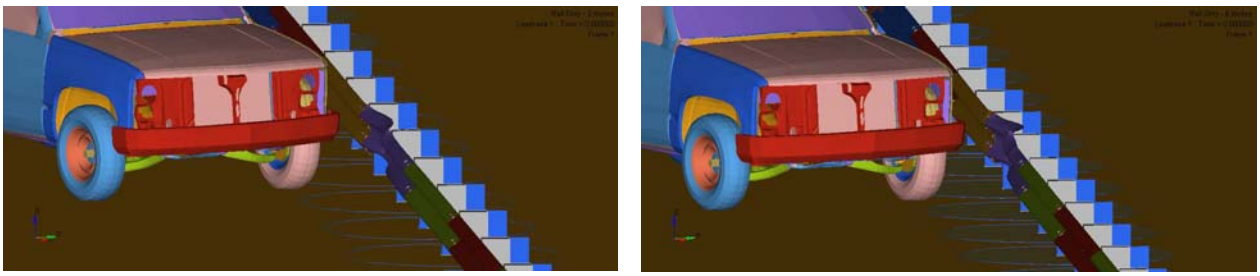

Figure 79: Pre-existing damage for rail deflection only simulations. 3 inches on left, 5.6 inches on right.

6.3 Results

6.3.1 Results for MGA Crash Test Simulations

The initial speeds and crash test results for the MGA crash tests and the MGA simulations are shown in Table 22. For the first impact, the initial velocity needed to get the same amount of simulated damage was 52.2 kph, which was higher than the initial speed of 48.3 kph in the MGA test. The impact speed in the simulation was higher because the simulated guardrail and soil was much stiffer than the real material, as mentioned earlier in Chapter 4. This higher stiffness caused the posts to separate more readily. To prevent any separation in the first

impact, it was necessary to use a rigid connection to keep post 11 connected to the rail. However, with the higher impact speed, the correct amount of static guardrail deflection was produced by the impact, as shown in Figure 80.

For the second impact, the simulation produced a lower deflection than the real MGA crash test. Again, this was due to the higher stiffness of the simulated guardrail and soil. The simulated deflection of 800 mm (31.5 inches) was 20% lower than the recorded deflection in the crash test of 999 mm (39.3 inches), which was exactly what was expected from the results presented in Table 10. Despite the lower deflection, the simulation was still able to match the crash test results and predict that the vehicle would vault over the guardrail. Like in the first impact, it was necessary to use a rigid connection to keep post 13 from separating. This was the only constraint present in the second impact model.

Table 22: Initial velocities and results for MGA tests

Crash Test	Initial Vehicle Velocity (kph)	Maximum Static Rail Deflection (mm)	Test Outcome
MGA Crash Test 1	48.3	369	Success
MGA Crash Test 2	99.9	999	Vault
MGA Simulation 1	52.2	372	Success
MGA Simulation 2	100.0	800	Vault

An important factor in the outcome of the second crash was whether the rail and post connections remained intact. In the real MGA crash test, posts 8, 10-12, and 14 separated from the rail as a result of the impact. However, post 13, which was directly in the path of the vehicle's initial trajectory, failed to separate from the rail for unknown reasons (see Figure 81). As the post deflected backwards, it pulled the rail downward. This was believed to be a critical factor in the result of the crash test.

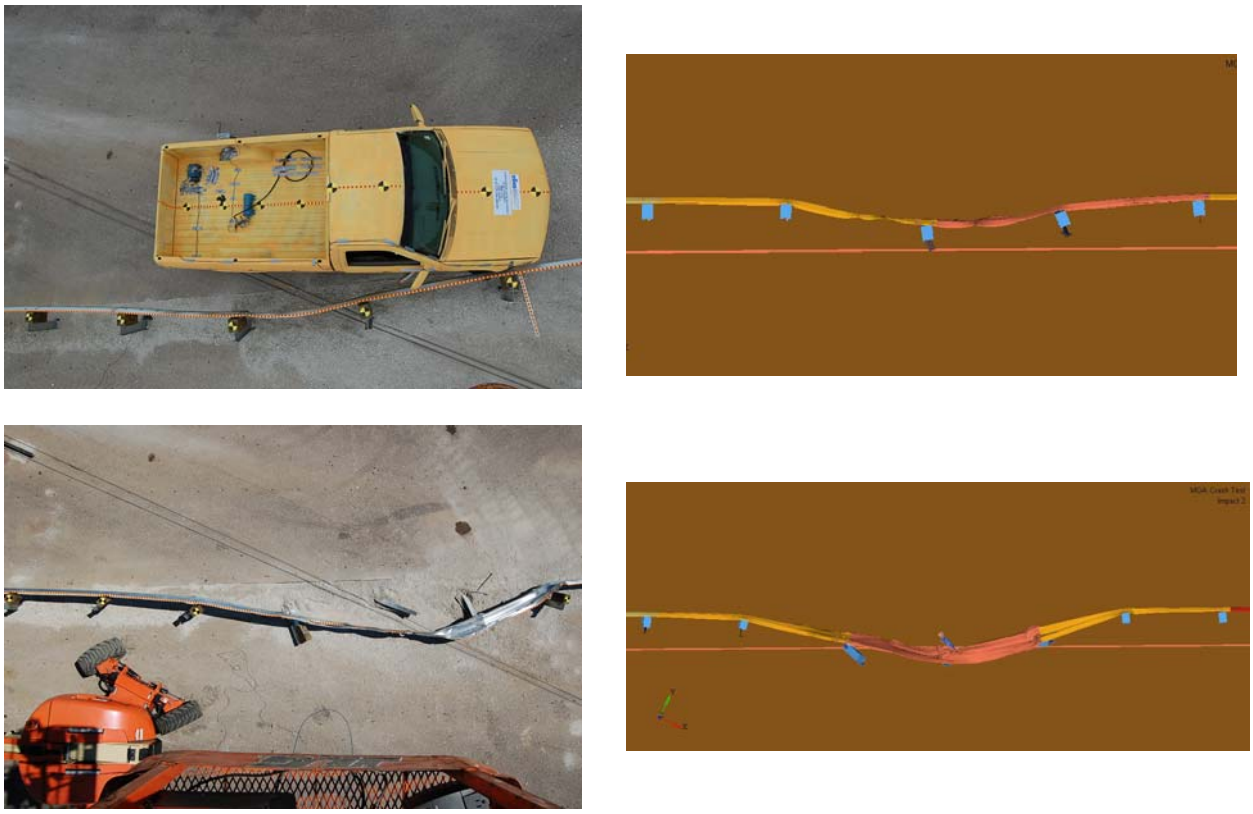

Figure 80: MGA crash test damage (left column) and MGA simulation damage (right column). The top row shows the guardrail damage after the first impact while the second row shows the damage for the second impact.

Figure 81: Post 13 after the second impact. In both the real test (left) and the simulation (right), the post failed to separate from the rail.

6.3.2 Results for rail and post deflection simulations

Each of the simulations with smaller pre-existing rail and post deflections (3 – 11 inches) were run, taking 21 to 25 hours each to complete. The damage caused by both the low severity

first impact and the full-scale second impact has been tabulated in Table 23. The results are collected in Table 24.

Table 23: Damage to guardrail in rail and post deflection simulations

	After First Impact		**After Second, TL3 Impact**	
	Max Flattening	**Separated Posts**	**Flattening**	**Separated Posts**
3 Inch	29.75%	None	84.61%	Posts 16-18
6 Inch	34.43%	None	83.21%	Posts 16-18
9 Inch	37.39%	Post 16	76.75%	Posts 16-17
11 Inch	51.89%	Post 16	81.10%	Posts 16-18

In Table 25 the simulation results are presented again, this time as the percentage difference between each of the minor damage simulations and the undamaged simulation. The majority of the changes were under 10%, with a couple exceptions in the acceleration measurements and the vehicle pitch.

Table 24: Simulation results for rail and post deflection

	Undamaged Model	3 Inches Rail & Post Deflection	6 Inches Rail & Post Deflection	9 Inches Rail & Post Deflection	11 Inches Rail & Post Deflection
Impact Conditions					
Speed (kph)	100	100	100	100	100
Angle (Deg)	25	25	25	25	25
Exit Conditions					
Speed (kph)	53	53	52	56	50
Angle (Deg)	14.5	13.2	13.8	15.6	15.0
Occupant					
Impact Velocity X (m/s)	7.5	8.0	8.0	8.6	8.3
Impact Velocity Y (m/s)	5.5	5.6	5.5	5.5	5.9
Ridedown X (G)	-11.8	-12.0	-12.2	-10.7	-12.8
Ridedown Y (G)	-12.3	-13.0	-10.1	-12.0	-10.4
50 ms Average X (G)	-6.7	-6.7	-6.8	-7.9	-7.1
50 ms Average Y (G)	-6.8	-6.7	-6.5	-6.5	-6.8
50 ms Average Z (G)	-3.8	-3.9	-3.0	-4.2	-4.6
Guardrail Deflection					
Max Dynamic (m)	0.69	0.72	0.74	0.76	0.78
Static Deflection (m)	0.55	0.62	0.55	0.60	0.64
Pre-existing damage (m)	0.00	0.07	0.15	0.22	0.28
Vehicle Rotation					
Max Roll (Deg)	-14.4	-12.9	-13	-16.6	-13.2
Max Pitch (Deg)	-9.9	-10	-6.6	-5.6	10
Max Yaw (Deg)	40.3	40	40	41	40.5

Table 25: % Change from undamaged simulation for rail and post deflection simulations

		3 Inches Rail & Post Deflection	6 Inches Rail & Post Deflection	9 Inches Rail & Post Deflection	11 Inches Rail & Post Deflection
Impact Conditions					
	Speed (kph)	0.00%	0.00%	0.00%	0.00%
	Angle (Deg)	0.00%	0.00%	0.00%	0.00%
Exit Conditions					
	Speed (kph)	0.00%	-1.89%	5.66%	-5.66%
	Angle (Deg)	-8.88%	-4.87%	7.43%	3.54%
Occupant					
	Impact Velocity X (m/s)	6.46%	6.34%	14.49%	10.33%
	Impact Velocity Y (m/s)	1.54%	0.17%	-1.01%	6.18%
	Ridedown X (G)	1.54%	3.51%	-9.41%	9.10%
	Ridedown Y (G)	6.19%	17.58%	-1.80%	-15.21%
	50 ms Average X (G)	0.78%	1.53%	18.21%	6.9%
	50 ms Average Y (G)	-1.55%	-4.74%	-4.60%	-0.24%
	50 ms Average Z (G)	1.51%	21.49%	8.19%	20.04%
Guardrail Deflection					
	Max Dynamic (m)	4.65%	7.28%	9.76%	13.37%
	Static Deflection (m)	12.09%	-0.09%	7.90%	15.69%
Vehicle Rotation					
	Max Roll (Deg)	-10.42%	-9.72%	15.28%	-8.33%
	Max Pitch (Deg)	1.01%	-33.33%	-43.43%	1.01%
	Max Yaw (Deg)	-0.74%	-0.74%	1.74%	0.50%

Figure 82 shows the vehicle rotation (roll, pitch, and yaw) for the undamaged simulation and each of the rail and post deflection simulations. The vehicle yaw and roll were nearly identical for all of the simulations. The pitch varied between the simulations, but there was no pattern observed and the magnitude of the vehicle pitch remained small in all of the simulations.

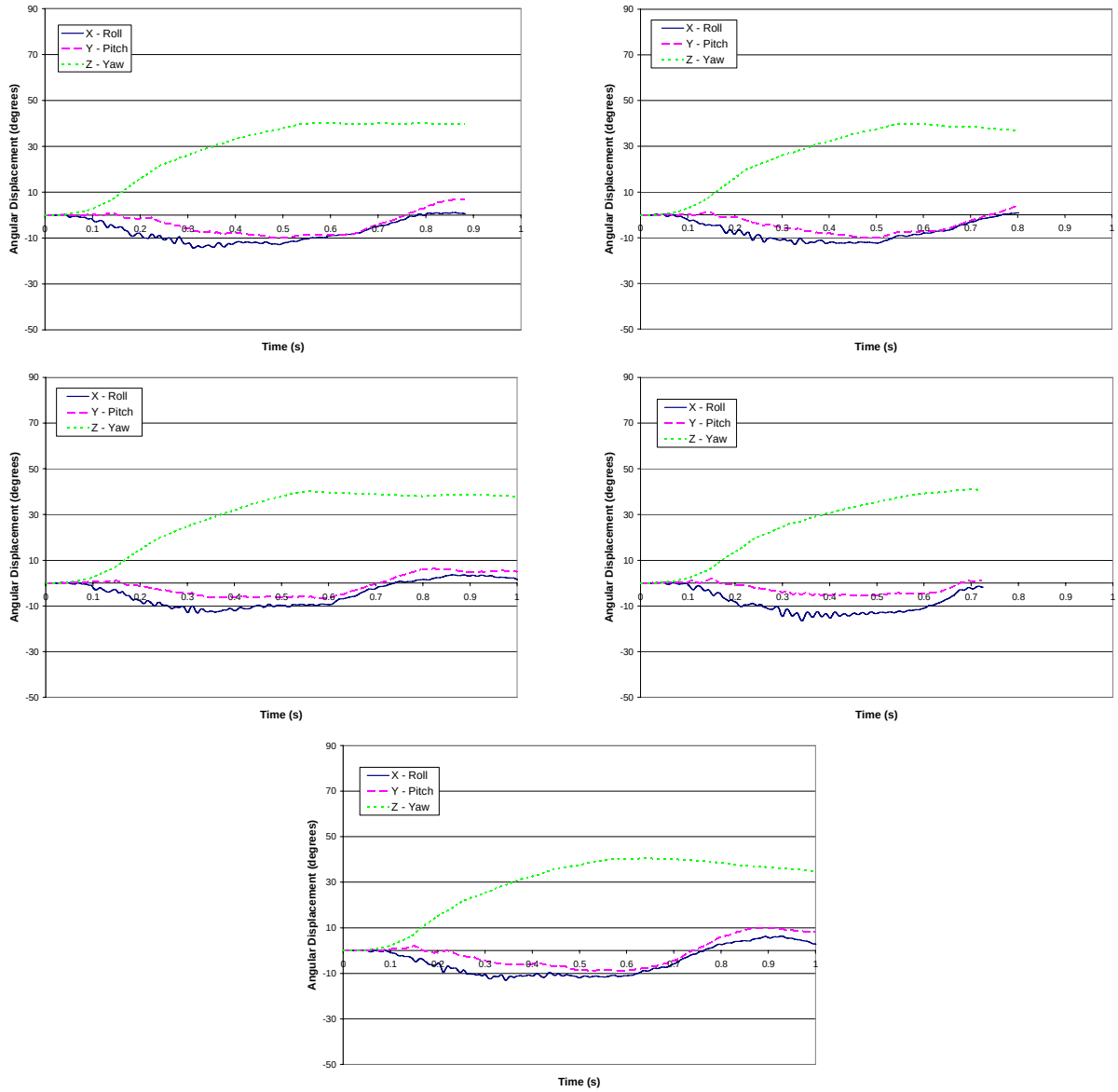

Figure 82: Vehicle rotation for rail and post deflection simulations. Undamaged (top left), 3 inches (top right), 6 inches (middle left), 9 inches (middle right), and 11 inches (bottom).

Next, Figure 83 shows the local vehicle velocity at the center of gravity as a function of time. Again, there was almost no difference in the velocity between the undamaged simulation and the rail and post deflection simulations. Exit speeds for all of the simulations were consistently in the range of 50 – 56 kph. There was also a peak in the vehicle lateral (Y-axis) motion during the impact, implying that the vehicle was skidding during the impact, but this died out by the time the vehicle was exiting the guardrail (~ 0.65 to 0.7 seconds).

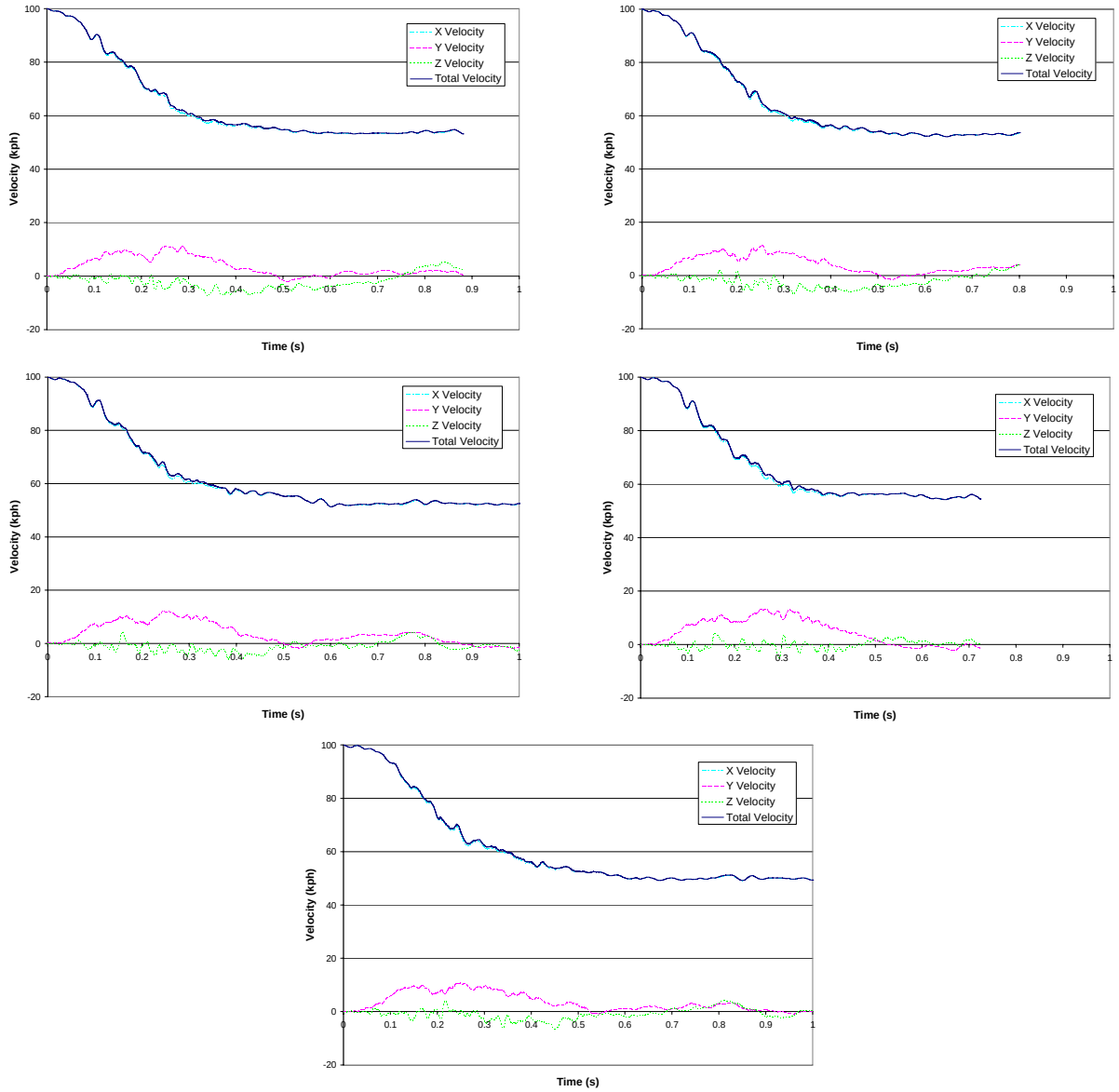

Figure 83: Vehicle velocities for rail and post deflection simulations. Undamaged (top left), 3 inches (top right), 6 inches (middle left), 9 inches (middle right), and 11 inches (bottom).

Although there was very little change in the vehicle speed or rotation, there were changes in the maximum deflection of the guardrail. As the amount of rail and post deflection increased, the maximum dynamic deflection of the rail also increased. However, each increase in pre-existing rail and deflection (60 – 80 mm each) only resulted in a 20 – 30 mm increase in maximum rail deflection. The increase in maximum dynamic deflection was much lower than

was observed for the missing post simulations, but could still pose some risk if a hazardous object was directly behind the guardrail space.

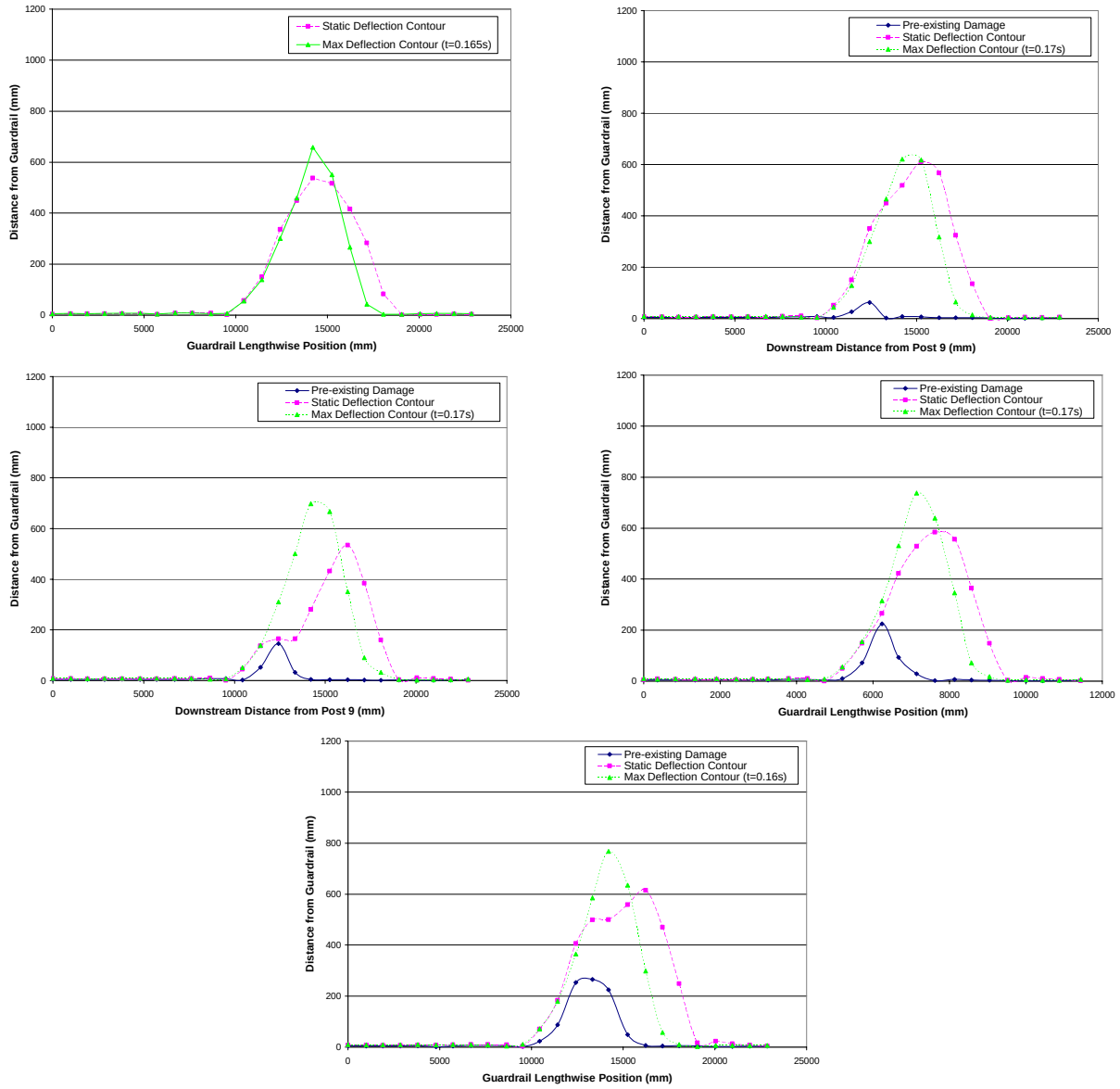

Figure 84: Guardrail damage contours for rail and post deflection simulations. Undamaged (top left), 3 inches (top right), 6 inches (middle left), 9 inches (middle right), and 11 inches (bottom).

The energies for each simulation are shown in Figure 85. For all of the simulations, the total energy in the simulation was nearly constant (< 1% variation from beginning to end). The final kinetic energy was also very similar for all of the simulations. The potential energy and hourglass energy increased along with the magnitude of pre-existing deflection. However, these

increases were offset by the increases in the interface energy, and the net result was little change to the vehicle speed or overall energy.

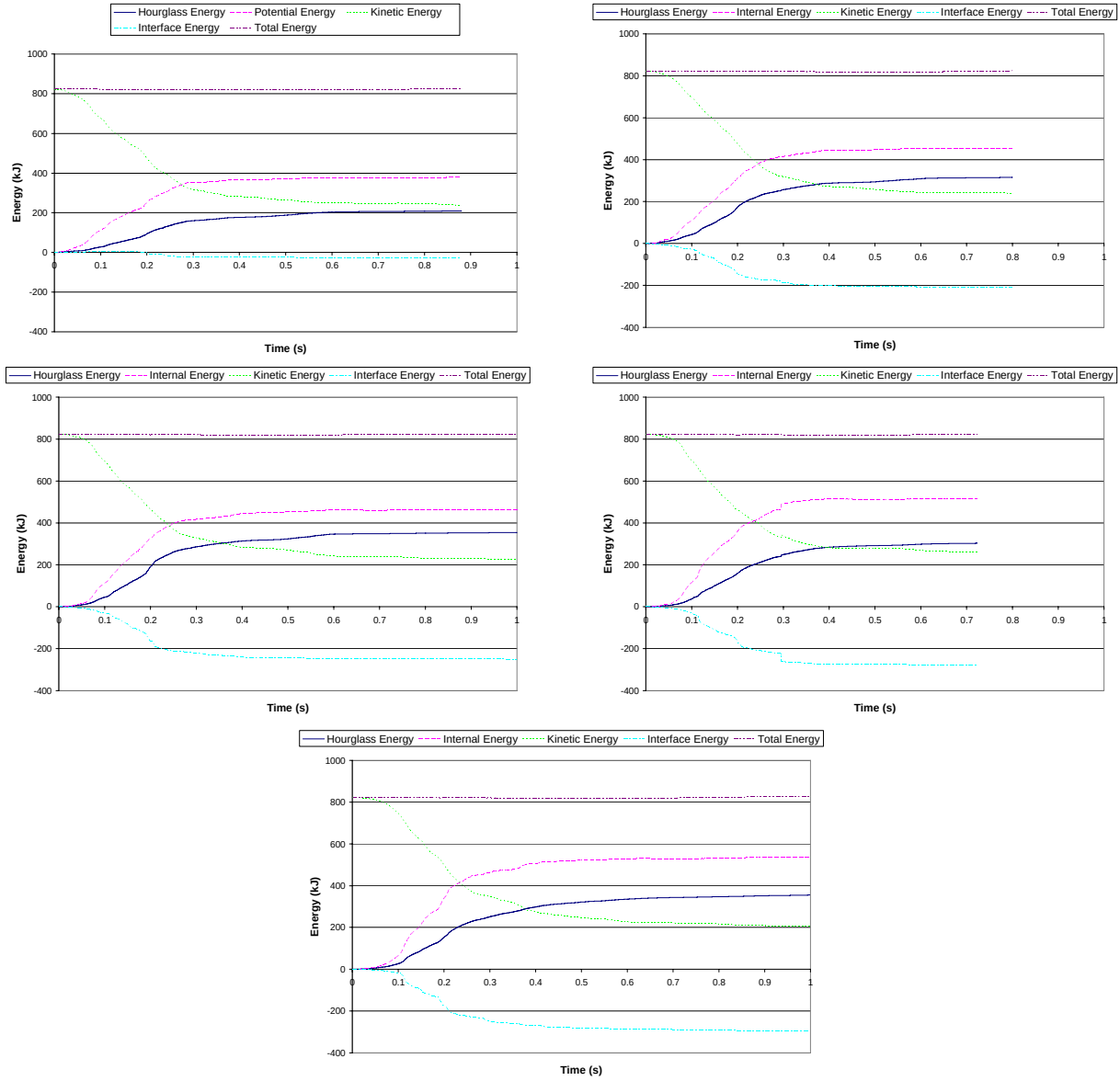

Figure 85: Energy balances for rail and post deflection simulations. Undamaged (top left), 3 inches (top right), 6 inches (middle left), 9 inches (middle right), and 11 inches (bottom).

6.3.3 Results for rail deflection only simulations

In Table 26, the damage to the guardrail, both after the first impact and after the second impact, are shown. Similar to the results observed for the combined rail and post deflection

simulations, the flattening in the rail produced by the first, low severity impact increased along with the magnitude of the rail deflection. None of the posts separated in the first impact for either of the simulations, which was to be expected as no damage to the post was incurred. After the second impact, both simulations reported similar amounts of post separation and flattening.

Table 26: Damage to guardrail in rail deflection only simulations

	After First Impact		**After Second, TL3 Impact**	
	Max Flattening	**Separated Posts**	**Flattening**	**Separated Posts**
3 Inch	31.3%	None	81.5%	16-18
6 Inch	39.9%	None	82.4%	16-17

The NCHRP 350 test criteria are reported in Table 27. The vehicle exit conditions remained consistent for both the undamaged and rail deflection only simulations. The 50ms averaged accelerations were also the same across all the simulations. Roll and pitch decreased slightly as the amount of rail deflection increased, whereas the longitudinal occupant impact velocity increased.

Table 27: Simulation results for rail deflection only simulations

		Undamaged Model	3 Inches Rail Deflection Only	6 Inches Rail Deflection Only
Impact Conditions				
	Speed (kph)	100	100	100
	Angle (Deg)	25	25	25
Exit Conditions				
	Speed (kph)	53	53.5	54.0
	Angle (Deg)	14.5	11.5	12.5
Occupant				
	Impact Velocity X (m/s)	7.5	8.0	8.2
	Impact Velocity Y (m/s)	5.5	5.6	5.3
	Ridedown X (G)	-11.8	-10.0	-9.7
	Ridedown Y (G)	-12.3	-14.2	-9.7
	50 ms Average X (G)	-6.7	-6.4	-6.6
	50 ms Average Y (G)	-6.8	-7.3	-7.0
	50 ms Average Z (G)	-3.8	-3.4	3.5
Guardrail Deflection				
	Max Dynamic (m)	0.69	0.71	0.71
	Static Deflection (m)	0.55	0.60	0.58
	Pre-existing damage (m)	0.00	0.08	0.14
Vehicle Rotation				
	Max Roll (Deg)	-14.4	-12.0	-10.8
	Max Pitch (Deg)	-9.9	-8.1	-8.6
	Max Yaw (Deg)	40.3	39.5	40.9

The percentage changes for NCHRP 350 test criteria relative to the simulation of undamaged guardrail are shown in Table 28. There was no observed trend of increasing maximum dynamic or static deflection in the guardrail, despite the observance of small increases when the rail deflection was combined with post deflection. This would imply that the posts contribute significantly to the performance of the guardrail.

Table 28: % change from undamaged simulation to rail deflection only simulations

		3 Inches Rail & Post Deflection	6 Inches Rail & Post Deflection
Impact Conditions			
	Speed (kph)	0.0%	0.0%
	Angle (Deg)	0.0%	0.0%
Exit Conditions			
	Speed (kph)	0.9%	1.9%
	Angle (Deg)	-21.0%	-13.6%
Occupant			
	Impact Velocity X (m/s)	6.4%	9.4%
	Impact Velocity Y (m/s)	2.6%	-2.8%
	Ridedown X (G)	-15.4%	-17.7%
	Ridedown Y (G)	15.2%	-20.8%
	50 ms Average X (G)	-4.7%	-1.8%
	50 ms Average Y (G)	7.7%	2.5%
	50 ms Average Z (G)	-9.5%	-7.9%
Guardrail Deflection			
	Max Dynamic (m)	2.8%	2.5%
	Static Deflection (m)	8.8%	5.5%
Vehicle Rotation			
	Max Roll (Deg)	-16.7%	-10.0%
	Max Pitch (Deg)	-18.2%	7.4%
	Max Yaw (Deg)	-2.0%	3.5%

The vehicle rotation about its own center of gravity is shown in Figure 86 for the two rail deflection simulations and the undamaged simulation. The vehicle's yaw was roughly the same for all of the simulations. The roll and pitch varied by only a slight amount (< 5 degrees). For all of the simulations, there were no indications that the vehicle would become unstable.

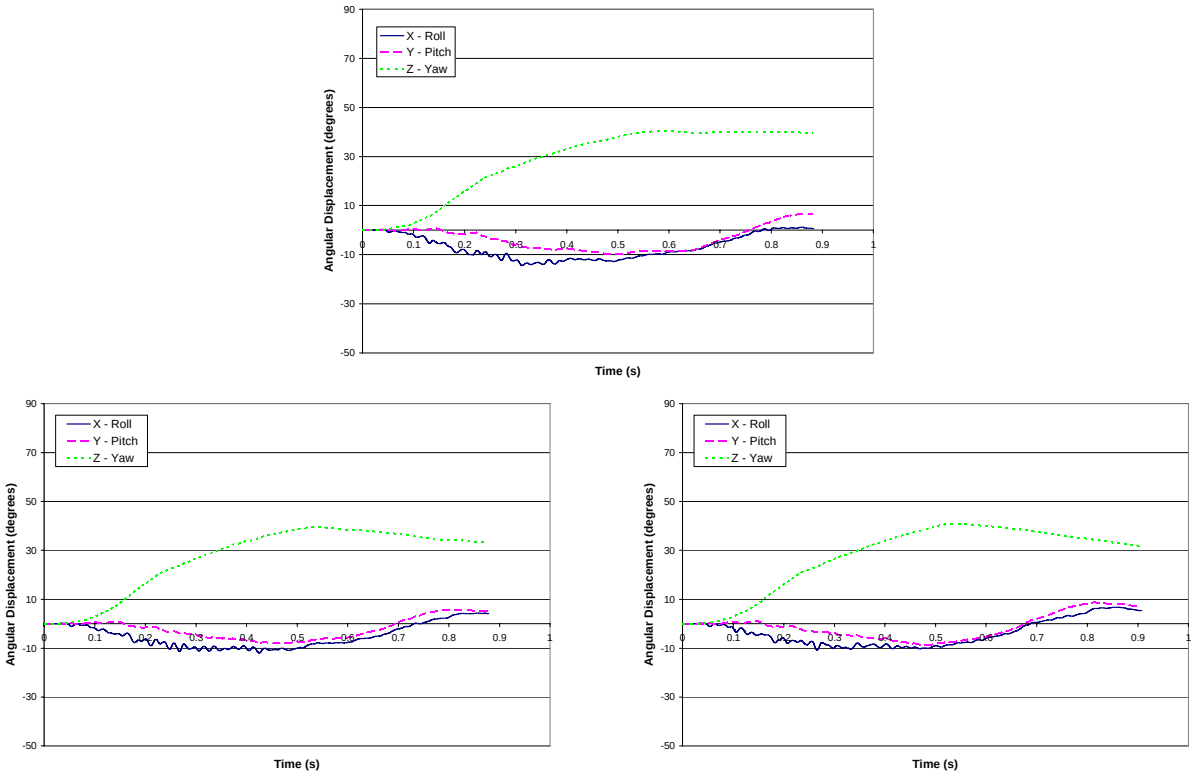

Figure 86: Vehicle rotations for rail deflection only simulations. Undamaged simulation (top), 3 inches (bottom left), and 6 inches (bottom right).

Similarly, the vehicle velocities were much the same between the three simulations, as shown in Figure 87. The vehicles all exited the guardrail with a final speed around 54 kph, and showed some lateral skidding during redirection that died out by the time the vehicle was exiting the guardrail.

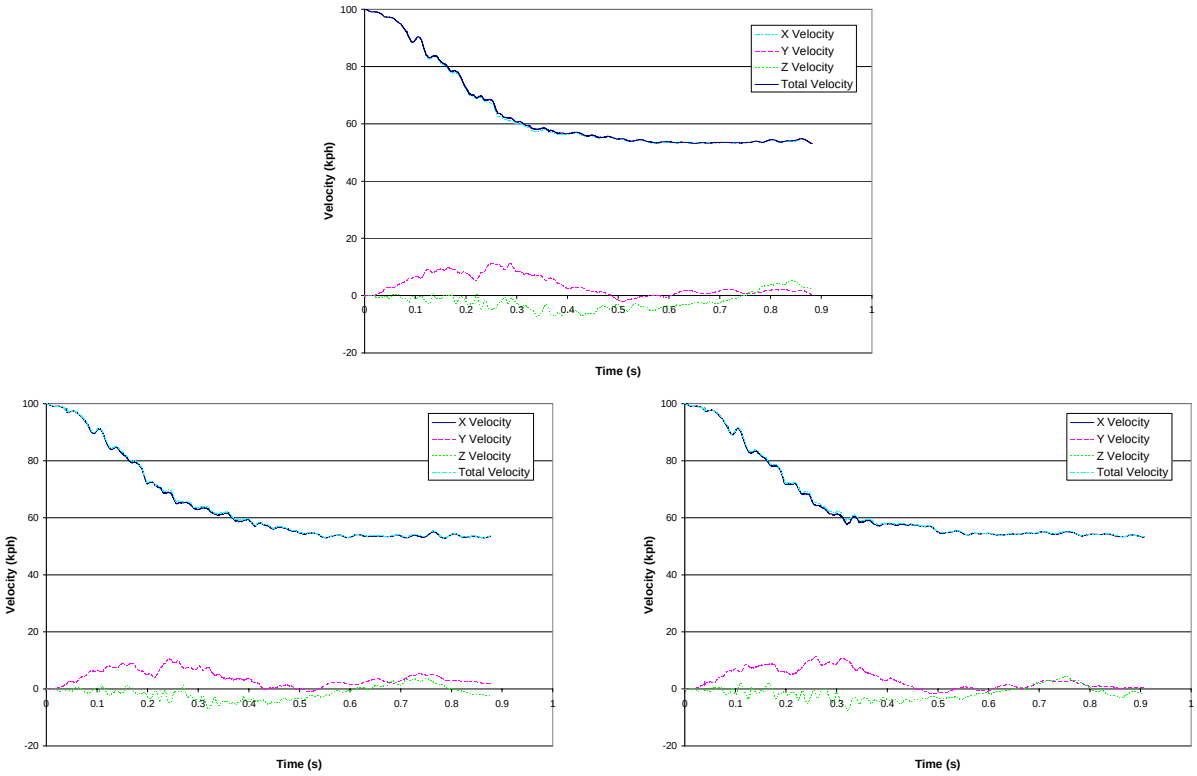

Figure 87: Vehicle CG velocities for rail deflection only simulations. Undamaged simulation (top), 3 inches (bottom left), and 6 inches (bottom right).

The static and dynamic guardrail deflections varied by very little, as shown in Figure 88. The pre-existing deflection in the guardrail had almost no effect on the deflection of the guardrail in the second, full-scale impact. This was a completely different outcome compared to the rail and post deflection simulations, with the only difference being the elimination of the post deflection. However, the location of the maximum dynamic deflection and maximum pre-existing damage in the guardrail did not match up, which was the same behavior observed for the simulations of combined rail and post deflection.

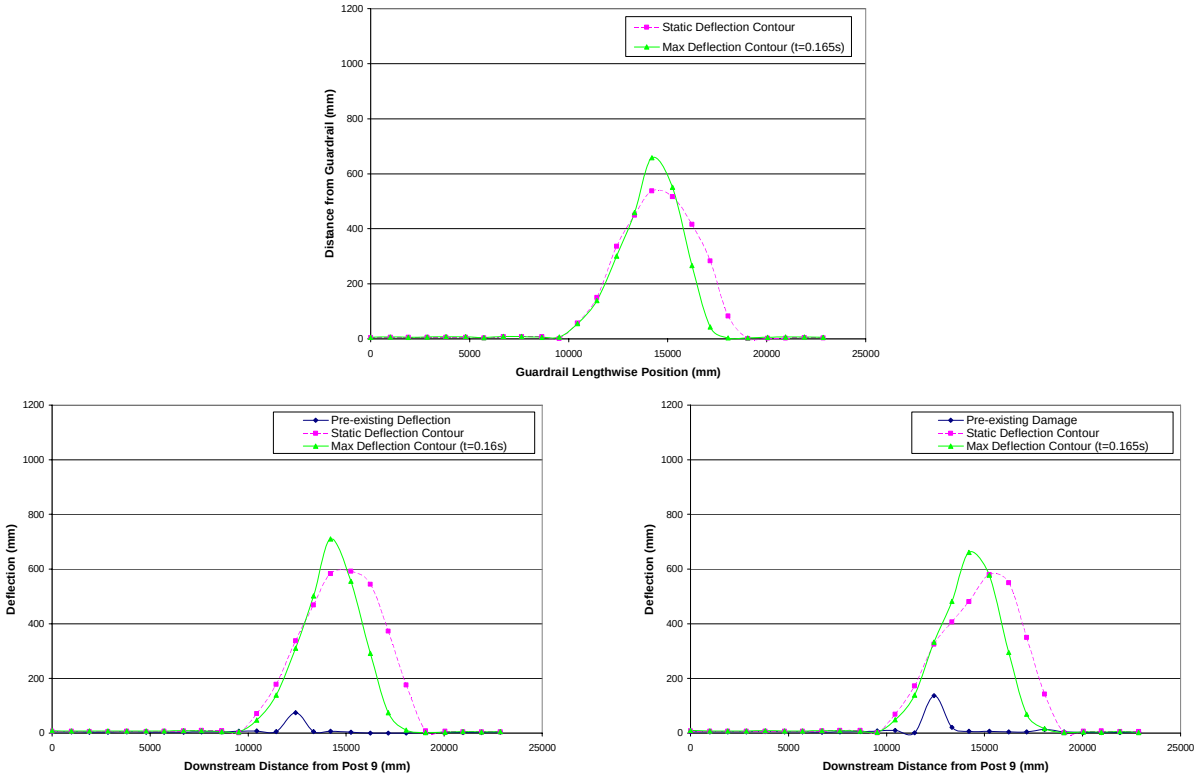

Figure 88: Guardrail deflection for rail deflection only simulations. Undamaged simulation (top), 3 inches (bottom left), and 6 inches (bottom right).

The simulation energies, shown in Figure 89, remained reasonable for all the simulations. The total energy in the simulation was very stable (< 1% variation) for the two simulations with rail only deflection. The hourglass energy was significantly higher, but it was balanced out by the higher negative energy in the interfaces, i.e. the contact algorithms. The potential and kinetic energies in the simulations were the same, which was expected since the damage to the guardrail and the vehicle exit speeds were also the same for the simulations.

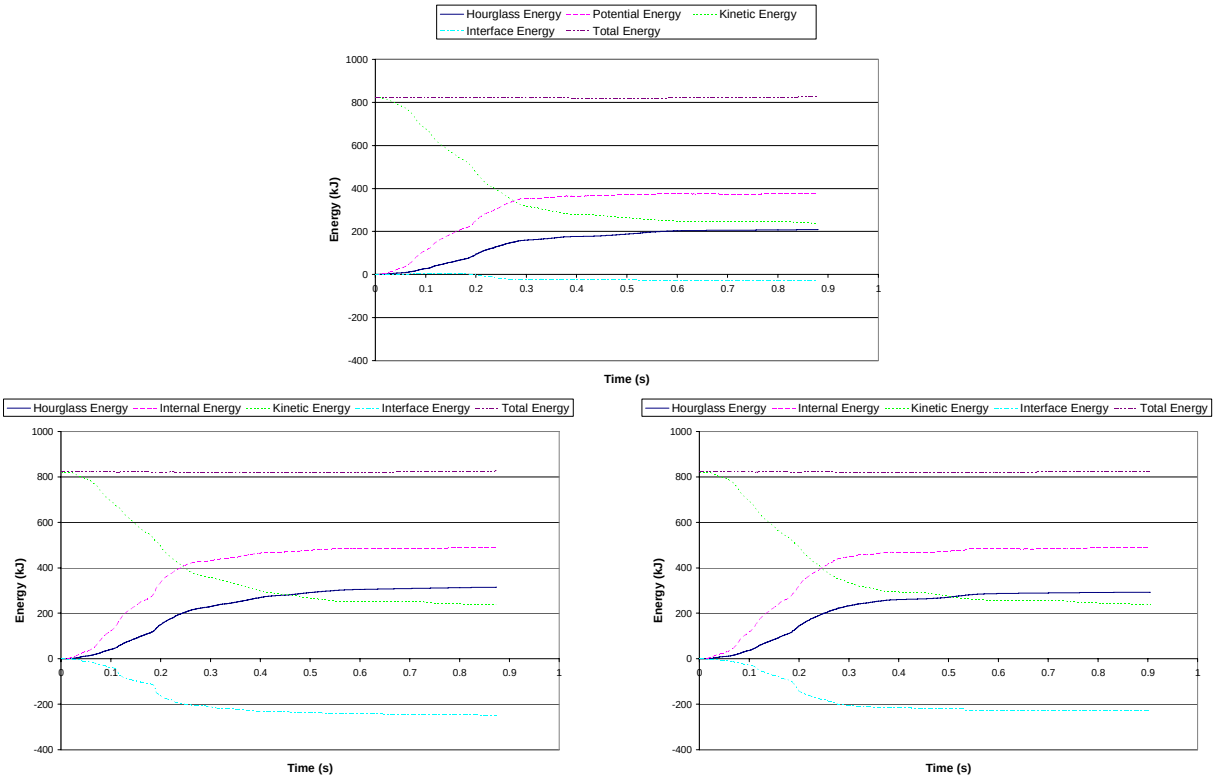

Figure 89: Energy balance for rail deflection only simulations. Undamaged simulation (top), 3 inches (bottom left), and 6 inches (bottom right).

6.4 Discussion

6.4.1 MGA Crash Test and Simulation

The results of the MGA crash test were successfully reproduced in the equivalent finite element model, although some artificial constraints were needed to match the post separation behavior in each of the two simulations. Both the crash test and the simulation resulted in the vehicle vaulting over the guardrail with rolling or pitching over. The acceleration values were within the acceptable limits, but the guardrail performance was still unacceptable due to the failure to redirect the vehicle away from the possible hazards behind it.

A major contributor to the vaulting of the vehicle in the MGA crash test was believed to be the failure of some of the posts to detach from the guardrail. While this may not have

appeared significant at first, it proved to be a major factor in the outcome of the simulation. In the real MGA crash test, post 13 failed to separate from the rail during impact. In a preliminary simulation of this crash, the post did separate, and the vehicle was successfully redirected. It was only when an artificial constraint was added to keep the post from separating that vaulting of the vehicle occurred. The failure of a post to separate from the rail during impact may be a major risk. However, it cannot be known beforehand whether a post will fail to separate.

6.4.2 Simulations of Rail and Post Deflection

In the simulations of the 3, 6, and 9 inches of rail and post deflection, it was found that minor rail and post deflection had a moderate effect on the simulation results. In particular, the vehicle pitch, longitudinal occupant impact velocity, and guardrail maximum dynamic deflection were the most affected. The longitudinal occupant impact velocity increased with increasing magnitude of rail and post deflection, from 7.5 m/s to 8.6 m/s for the simulation of 9 inches. However, all of the impact velocities were well under the limit of 12 m/s as specified by the NCHRP 350 test criteria.

Surprisingly, rail deflection only had little effect on the outcome of the crash tests. Vehicle exit kinematics and guardrail damage remained the similar even for as much as eleven inches of pre-existing deflection in the guardrail. These results also contribute to the theory that the posts in the strong-post guardrail systems, particularly whether the posts separate from the rails, were important contributors to the performance of the guardrail.

An interesting aspect of the second impact into the already damaged guardrail was that the position at which the maximum dynamic and static deflections occur was not the same point at which the pre-existing damage was located. The deflection might be higher for crashes where the second vehicle impact point was adjusted so that the points of maximum pre-existing damage

and maximum dynamic deflection are coincident. Even so, the pre-existing damage had a more profound effect than might be expected. For each additional 3 inches (0.08 meters) of deflection added to the simulated guardrail, the maximum dynamic deflection increased by ¾ to 1.25 inches (0.02 – 0.03 meters). The maximum increase, for the 9 inch deflection simulation, was 0.7 meters (roughly 10%) higher than observed in the undamaged simulation.

The vehicle itself did not become unstable for pre-damage up to 11 inches of pre-existing rail and post deflection. The accelerations, exit speed, and exit conditions varied widely but showed no discernable patterns. The only exception was the vehicle pitch, which decreased with increasing amounts of damage to the guardrail. However, the impact of this reduction was minimal since the pitch for the simulation of undamaged guardrail was already minimal (< 10 degrees).

All of the simulations of rail and post deflection were performed with a guardrail model using a stiff soil. If a softer soil model were to be used, the amount of expected deflection would greatly increase. However, models employing a softer soil were not implemented, due to a number of issues, including time constraints, problems with model stability, and difficulty in characterizing soil as a material. The greater deflection allowed by softer soils would imply that the threshold of acceptable limit should be much lower for soft soils.

6.4.3 Differences between the Simulations

The difference in simulation outcomes between the MGA simulations and the simulations of rail and post deflection was much larger than was expected. There were two major differences between the two simulations. As mentioned previously, there was a post that failed to separate from the rails in the MGA simulation. This phenomenon was not observed in any of the simulations of rail and post deflection. The other major difference was in the vehicle models.

The vehicle model for the MGA simulations was adapted to reflect the vehicle that was used in the real MGA crash tests (refer to Table 2). However, the simulations of lower rail and post deflection were performed with a vehicle with dimensions matching the vehicle used in TTI Crash test 405421-1. The front bumper height of the vehicle used in the MGA simulations was almost 50 mm higher than the vehicle used for the other simulations. Thus, the vehicle used in the MGA crash tests was always more likely to vault over the guardrail.

In the simulation of the second MGA crash test, the rail was pulled downward by the post that failed to release from the guardrail. This behavior was not observed for any of the other simulations. The height of the guardrail after the first impact but before the second impact was observed for all of the simulations, but no decrease in rail height was observed. This was expected since the height of guardrails with minor damage was maintained by the posts. Any small change in the height of the rails was countered by the increase in top height due to flattening that was concomitant with the deflection.

Since vaulting was attributed to the lowering of the rail during impact, the minimum height of the top of the rails was tabulated for the MGA and rail and post simulations. The resulting heights are shown in Table 29. For reference, the standard top height of the rails in newly installed guardrail is roughly 706 mm. There was no clear trend within the simulations of pre-existing damage for the rail height to decrease with increasing pre-damage. However, the rail height in the MGA simulation was far lower than any of the other simulations. The height of the rail appeared to be divergent, where the drop in rail height was minimal if the vehicle was successfully redirected, but if vaulting occurred there would be a massive drop in rail height.

The height of the rail after impact for the simulations of 0 – 11 inches of damage was dependent on many aspects of the crash, including the time at which the simulation ended and

the amount of twisting and flattening in the rails. The rail height for the 9 inch simulation was the highest both because it was the only simulation for which post 18 did not separate and there was a minimal amount of twisting in the rails. The 9 inch simulation also terminated much earlier than the other simulations (0.72s instead of 1.00s), which meant that the rail had less time to settle under the influence of gravity. The minimum height of the top of the rail in the 11 inch simulation was above that for the 6 inch simulation due to the large amount of flattening and limited twisting.

Table 29: Minimum rail heights after TL3 impact for rail and post deflection simulations

	Minimum Height of Bottom of Rails (mm)	Minimum Height of Top of Rails (mm)
Undamaged	221	600
3 Inches	241	647
6 Inches	217	572
9 Inches	275	670
11 Inches	205	591
MGA Test (14.5 Inches)	110	393

6.5 Recommendations for Rail and Post Deflection

The simulations conducted for this study indicate that the impacting vehicle did not become unstable for rail and post deflections up to 11 inches. In the MGA full-scale crash test, a second impact with a guardrail having 14 inches of pre-existing deflection resulted in the vehicle vaulting over the rails. However, the simulations of rail and post deflection were all performed using a very strong type of soil. If the guardrail was installed in a softer soil type, the deflection would be much higher, and the risks of vaulting would be greater. A conservative limit of 6 inches of combined rail and post deflection was recommended.

The presence of any amount of rail and post deflection in the guardrail was found to increase the amount of maximum dynamic deflection, so repairs to guardrail with hazardous

objects directly behind the guardrail should also be repaired quickly. Rail deflection only, up to 6 inches, had a minimal effect on the performance of the guardrail and the vehicle behavior. The repair of minor rail deflection would be low priority repairs. Since six inches was the maximum amount of rail only damage evaluated, the limit for rail only deflection was also set to 6 inches.

7. RAIL FLATTENING MODELS

7.1 Introduction

Rail flattening in strong-post w-beam guardrail was a damage mode of interest to many state agencies, ranking just below the various modes of rail and post deflection [5]. In the field, rail deflection is often associated caused by collisions at shallow angles or from pressure due to snowplows. Rail flattening was characterized by loss of depth in the w-beam rail element, which was often accompanied by rail deflection and post deflection. Concurrent with the loss of depth was an increase in the height of the guardrail, i.e. the upper edge of the guardrail extended higher while the lower edge moved closer to the ground.

Rail flattening was of concern for two reasons. First, the loss of depth in the rail reduced the spacing between the striking vehicle and the posts. Thus, an increased risk of snagging would be possible. Second, the flattening of the rail increases the maximum height and lowers the minimum height of the guardrail, changing the way in which the vehicle interacts with the guardrail system.

7.2 Methods

Rail flattening was one of the most difficult damage modes to reproduce in isolation. A new finite element model was developed to produce consistent flattening across a length of guardrail, shown in Figure 90. In this finite element model, all parts of the guardrail and the entire vehicle were removed, leaving only the rail elements. The center of all the rails were constrained from all motion (X, Y, and Z translation and rotation), so that the deformed rails could be easily incorporated into other finite element models.

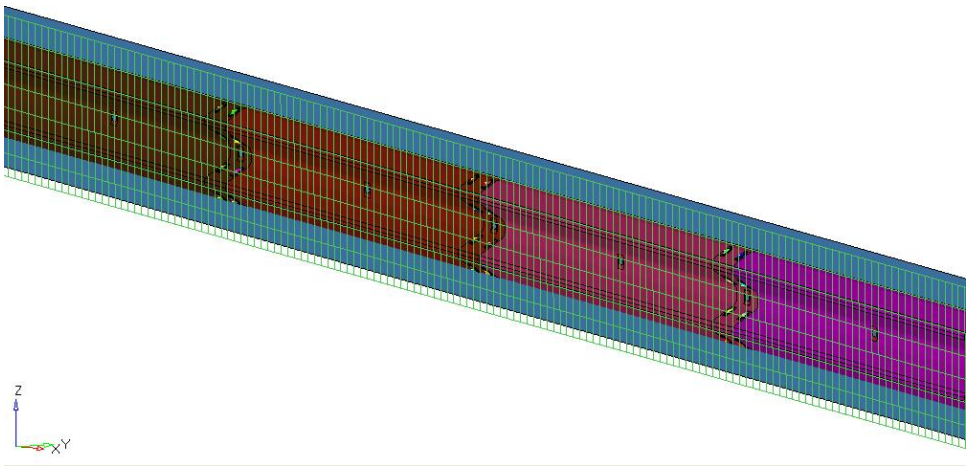

Figure 90: Finite element model to induce rail flattening

To induce flattening in the rails, two rigid plates were introduced into the finite element model. The first rigid plate was placed behind the rails and was fixed. The second plate was placed in front of the rails. A controlled displacement was added to move the second plate toward the rails, slowly flattening the rails. The rails continued to be flattened until the space between the two plates was so small that contact instabilities developed in the model, causing it to terminate. The simulation reached 95% flattening by the time it ended. The deformed geometry for the rails at 25%, 50%, and 75% were exported from the model incorporated later into a full-scale simulation. The reassembled full-scale models are shown below in Figure 91. Each simulation increased the amount of flattening by 25%, resulting in more rail height. It can also be seen that the bottom of the rail is closer to the ground as the amount of flattening increases.

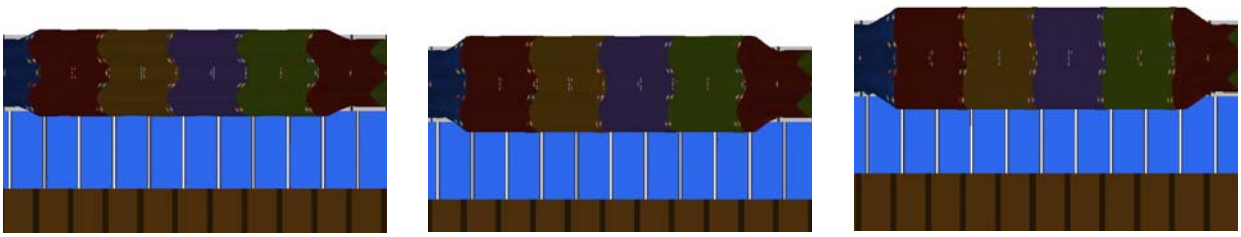

Figure 91: Rail flattening caused by two rigid plates. Flattening is 25% (left), 50% (middle), and 75% (right)

The simulation to produce rail flattening was unable to reproduce 100% flattening because of contact instabilities. In order to reproduce the maximum degree of flattening, the rails were manually flattened by translating and rotating the nodes of the rails in the pre-processing software. The resulting rails with ~100% flattening are shown below in Figure 92.

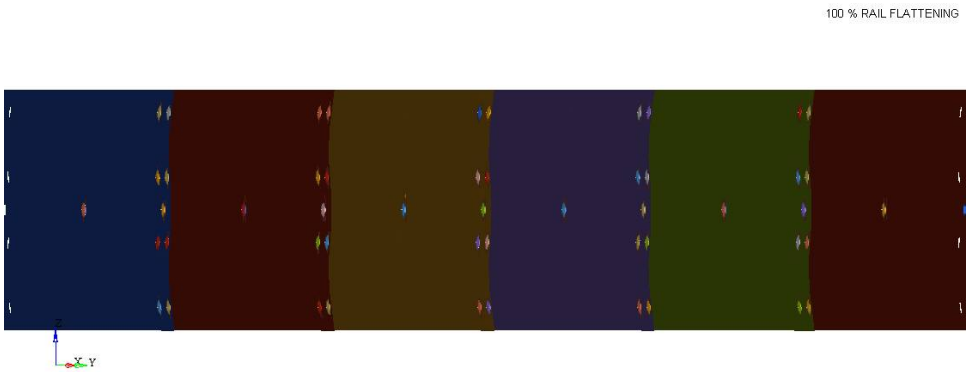

Figure 92: Rails flattened 100%

The final full-scale simulations of rail flattening were created by combining the flattened rail geometry with the undamaged guardrail simulation. First, the original rails were removed from the undamaged simulation. Next, the flattened rails were imported into the model and connected to the posts and adjacent rails. The complete set of finite element models covered all degrees of flattening between 25% and 100%, in increments of 25%. These simulations are shown in Figure 93.

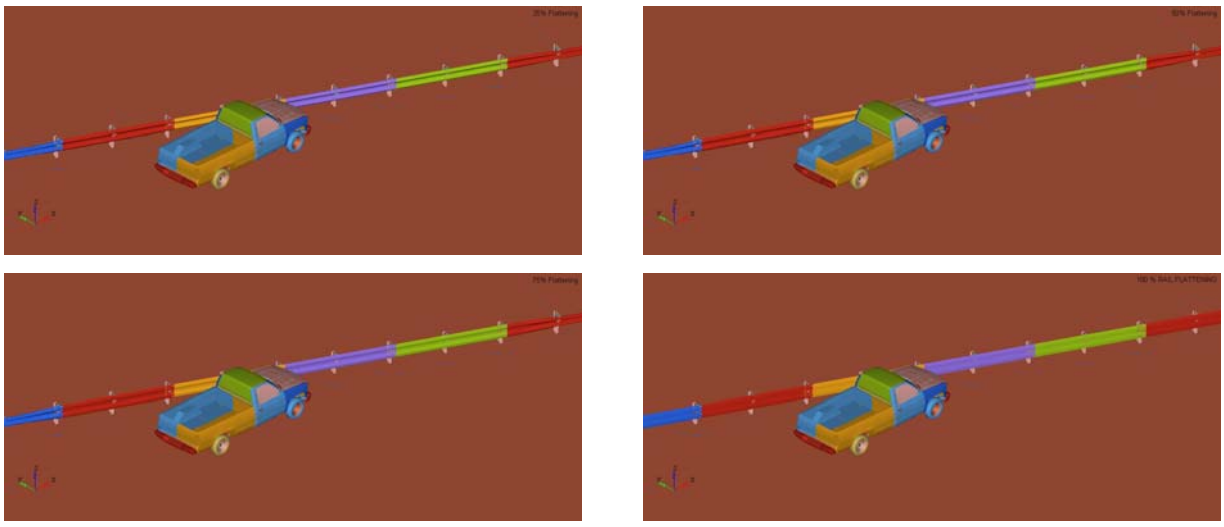

Figure 93: Rail flattening simulations before impact. 25% flattening (top left), 50% flattening (top right), 75% flattening (bottom left), and 100% flattening (bottom right)

7.3 Results

Each of the flattening simulations was run on the Inferno2 system using four processors. Each run required roughly 26 hours per simulation to complete. The results of the simulations at 700 ms are shown in Figure 94. The vehicle exit behavior became increasingly unstable as the rail was flattened by greater amounts. Both roll and pitch increased with the amount of flattening. However, the yaw and exit angle decreased with increasing flatness. At 100% flattening, the vehicle was unable to remain upright and rolled to the right after exiting the guardrail.

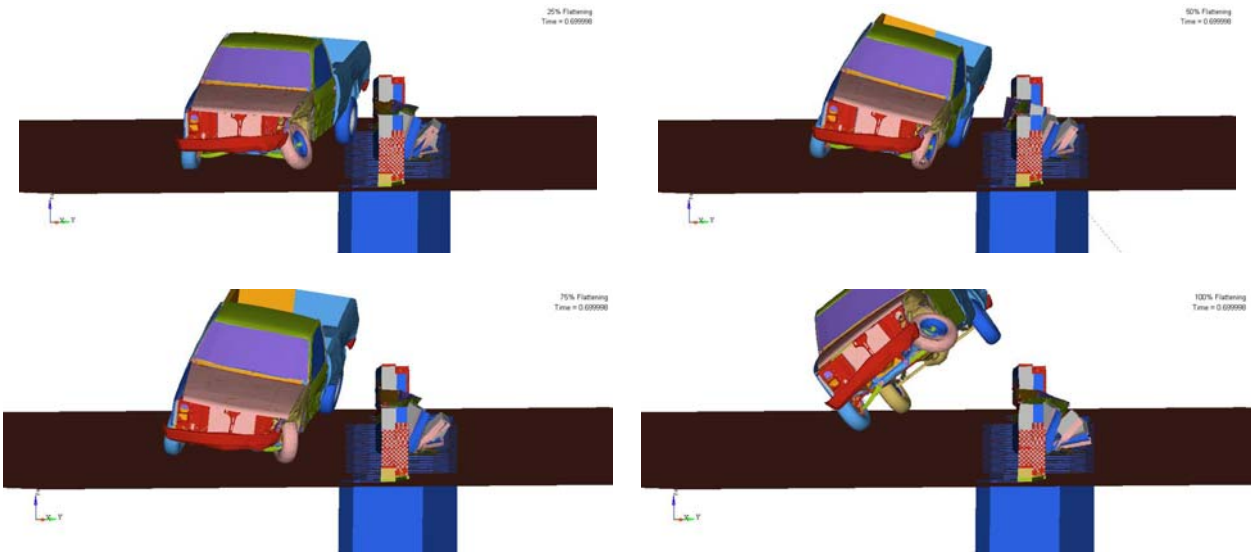

Figure 94: Flattening simulation results at t = 0.7s. 25% flattening (top left), 50% flattening (top right), 75% flattening (bottom left), and 100% flattening (bottom right).

In Table 30, the NCHRP 350 test criteria are shown for both the undamaged simulation and all of the flattening simulations. Table 31 presents the same data, but as the percent change from the values reported for the undamaged simulation. As observed in Figure 94, the roll and pitch were higher and the yaw was lower for all of the flattening simulations.

The degree of flattening in the guardrail had a strong effect on the exit speed and angle of the vehicle. The increase in exit speed was particularly pronounced at the highest levels of flatness, with a 13 kph (8.1 mph) increase in exit speed between 75% and 100% flattening. Exit angle showed the opposite behavior, i.e. it decreased with increasing flatness, from 14.5 degrees for the undamaged simulation to only 10 degrees for the 100 % flattened simulation.

Table 30: Results for rail flattening simulations

	Un-damaged	25% Flattening	50% Flattening	75% Flattening	100% Flattening
Impact Conditions					
Speed (kph)	100	100	100	100	100
Angle (deg)	25	25	25	25	25
Exit Conditions					
Speed (kph)	53	56	59	60	73
Angle (deg)	14.5	12.1	9.1	10.7	10.0
Occupant					
Impact Velocity X (m/s)	7.51	7.3	7.5	6.8	5.9
Impact Velocity Y (m/s)	5.54	5.5	5.7	5.7	5.7
Ridedown X (G)	-11.77	-14.7	-10.9	-14.1	-7.4
Ridedown Y (G)	-12.27	11.4	-11.6	-12.3	-11.4
50 ms Average X (G)	-6.68	-5.6	-6.0	-6.1	-5.4
50 ms Average Y (G)	-6.82	-6.6	-7.1	-6.9	-7.2
50 ms Average Z (G)	-3.85	3.3	-3.7	-4.1	2.6
Guardrail Deflections					
Dynamic (m)	0.69	0.74	0.75	0.75	0.80
Static (m)	0.55	0.57	0.44	0.43	0.62
Vehicle Rotations					
Max Roll (deg)	-14.4	-15.8	-16.7	15.2	Roll
Max Pitch (deg)	-9.9	-12.3	20.2	-20.7	> 18
Max Yaw (deg)	40.3	38.3	38.0	38.0	33.5

The occupant kinematics in the X direction were actually better for the flattened rails than for the undamaged simulation. The longitudinal occupant impact velocity decreased with each increase in rail flatness. The impact speed for 100% flattening was only 5.9 m/s, which represented a 21% decrease from the undamaged simulation impact speed. The lateral impact speed was consistent for all the simulations, ranging between 5.5 and 5.7 m/s.

The vehicle accelerations showed no discernable patterns. However, the 50ms average longitudinal acceleration was lower than that of the undamaged simulation for all of the flattening simulations. The deflection of the guardrail, particularly the maximum dynamic deflection, increased along with flattening. The maximum deflection increased by 15.5% for a

completely flattened rail, which was much lower than the missing post simulations which increased by 25 - 50%.

Table 31: Percent change for rail flattening simulations

		25% Flattening	50% Flattening	75% Flattening	100% Flattening
Impact Conditions					
	Speed (kph)	0.0%	0.0%	0.0%	0.0%
	Angle (deg)	0.0%	0.0%	0.0%	0.0%
Exit Conditions					
	Speed (kph)	5.7%	11.3%	13.2%	37.7%
	Angle (deg)	-16.2%	-37.2%	-26.5%	-30.9%
Occupant					
	Impact Velocity X (m/s)	-2.9%	-0.3%	-9.5%	-21.4%
	Impact Velocity Y (m/s)	-0.2%	2.9%	3.8%	2.8%
	Ridedown X (G)	25.1%	-7.7%	19.4%	-37.1%
	Ridedown Y (G)	-6.9%	-5.8%	-0.1%	-6.9%
	50 ms Average X (G)	-16.8%	-10.9%	-8.1%	-18.5%
	50 ms Average Y (G)	-3.7%	4.8%	0.7%	5.6%
	50 ms Average Z (G)	-13.6%	-4.1%	6.8%	-32.4%
Guardrail Deflections					
	Dynamic (m)	7.8%	9.0%	8.1%	15.5%
	Static (m)	3.6%	-20.8%	-21.1%	13.2%
Vehicle Rotations					
	Max Roll (deg)	9.7%	16.0%	5.6%	Roll
	Max Pitch (deg)	24.2%	104.0%	109.1%	> 81.8%
	Max Yaw (deg)	-5.0%	-5.7%	-5.7%	-16.9%

Figure 95 below shows the roll, pitch, and yaw vs. time curves for the undamaged simulation and all of the flattening simulations. As expected, the roll for the 100% flattening simulation was the largest. The yaw for all of the flattening simulations peaked in the range of 400 – 500 ms, after which it started to decline. As the yaw was directly related to the heading of the vehicle, this implied that the vehicle was turning back toward the guardrail after exiting. The opposite sign on the pitch for the 100% flattening simulation implied a possibility of vaulting.

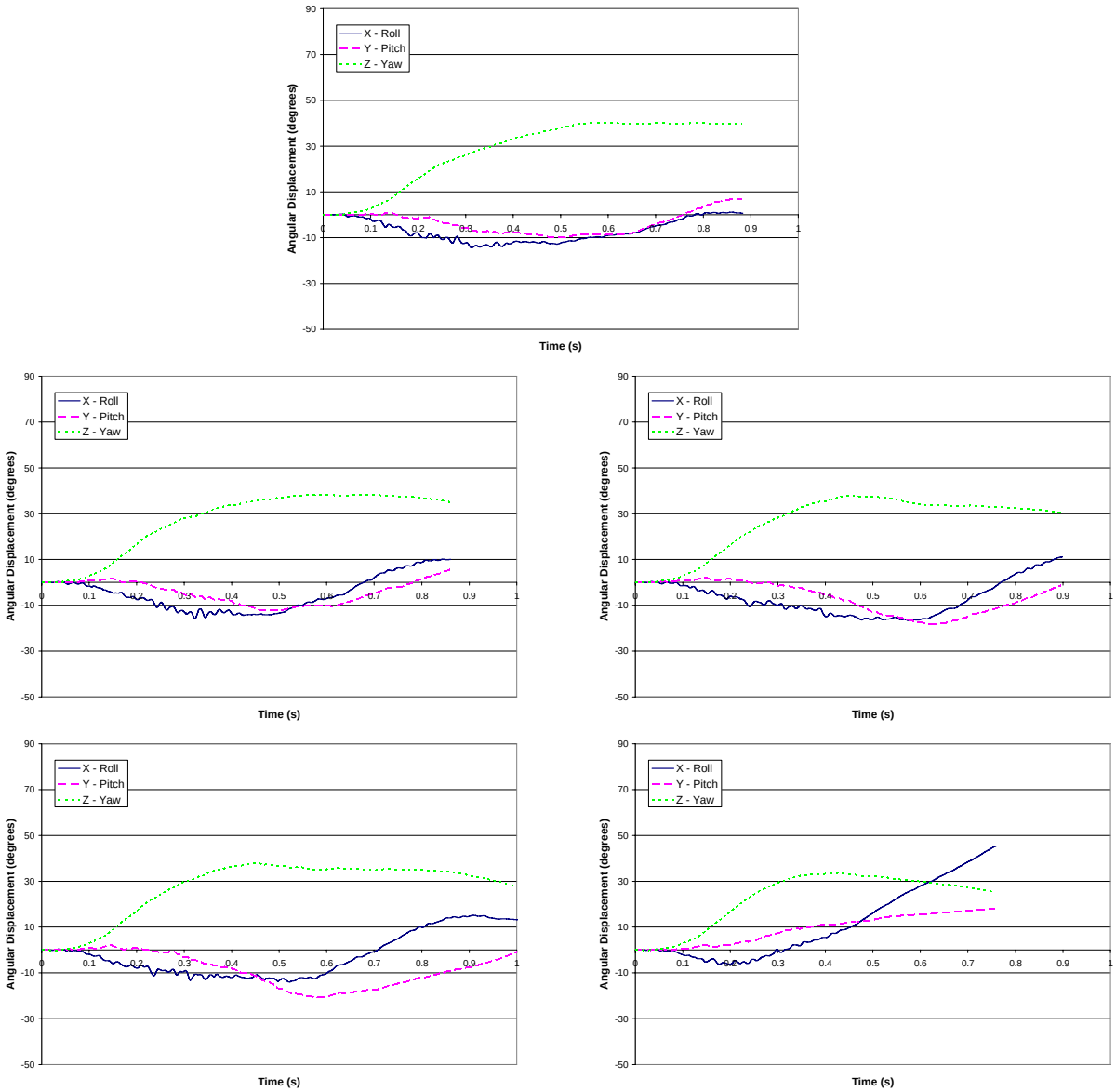

Figure 95: Roll, pitch, and yaw curves for flattening simulations. Undamaged (top), 25% flattening (middle left), 50% flattening (middle right), 75% flattening (lower left), and 100% flattening simulations (lower right)

Figure 96 shows the local vehicle CG velocities for the undamaged and all flattening simulations. All of the simulations showed stable exit velocities. The 50% and 75% simulations also showed a relatively large amount of lateral skidding and upward motion as the vehicle was exiting the guardrail. This skidding motion was caused by the edge of the vehicle bed catching on a fold in the guardrail near a post, which also contributed to the decrease in yaw.

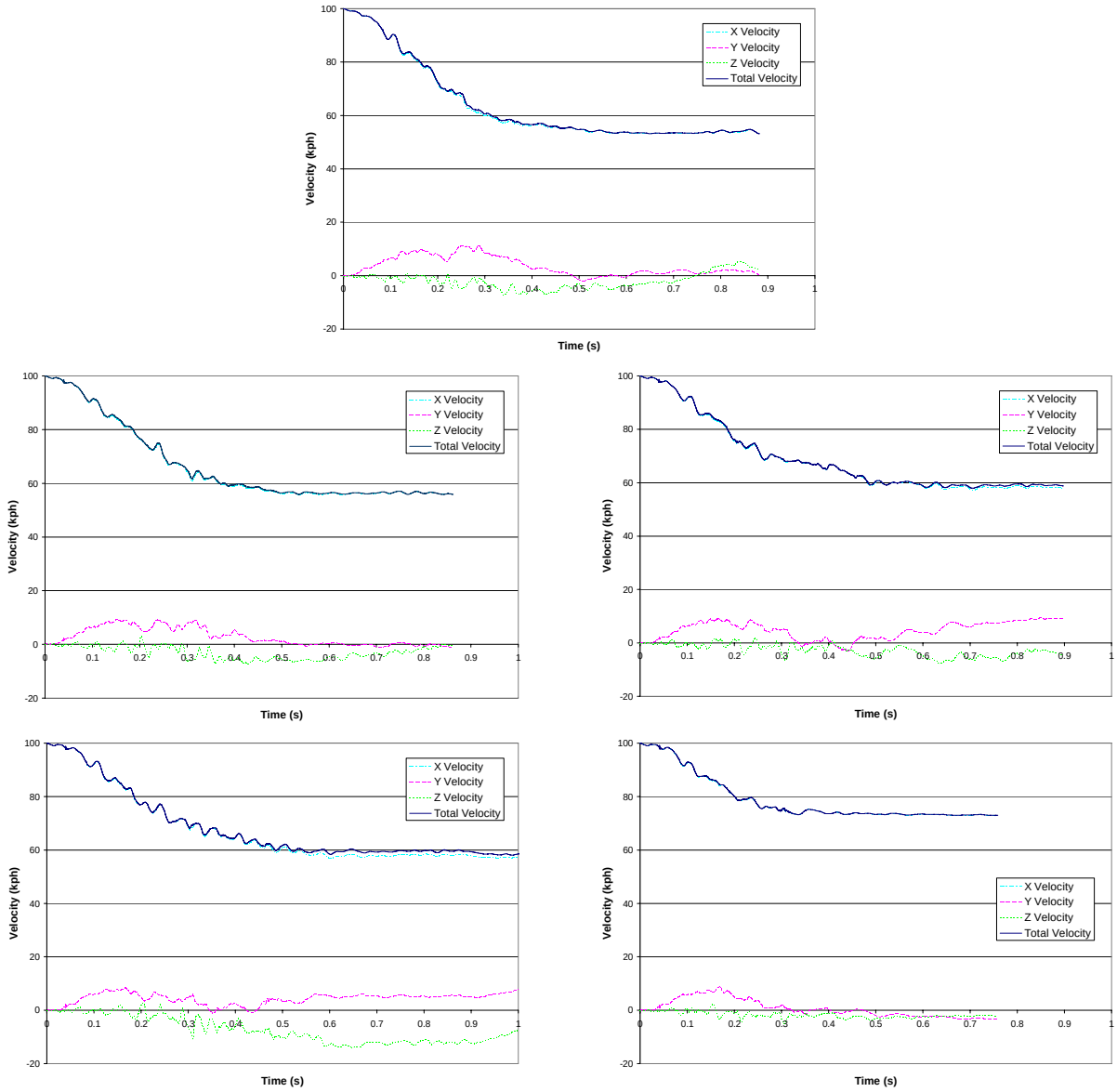

Figure 96: Velocity curves for flattening simulations. Undamaged (top), 25% flattening (middle left), 50% flattening (middle right), 75% flattening (lower left), and 100% flattening simulations (lower right)

In Figure 97, some coarse damage contours for the guardrail are shown. All of the damage contours were measured starting at post 9 (position = 0) up to post 21 (position = 22860 mm). For all simulations, except the 100% flattening simulation, the maximum dynamic deflection occurred at 165 ms. At this time, the vehicle was still moving into the guardrail and was just starting to be redirected. The static deflection contours for 25% - 75% flattening were

very uneven. This was due to vibrations induced in the rail when the vehicle bed slapped the guardrail.

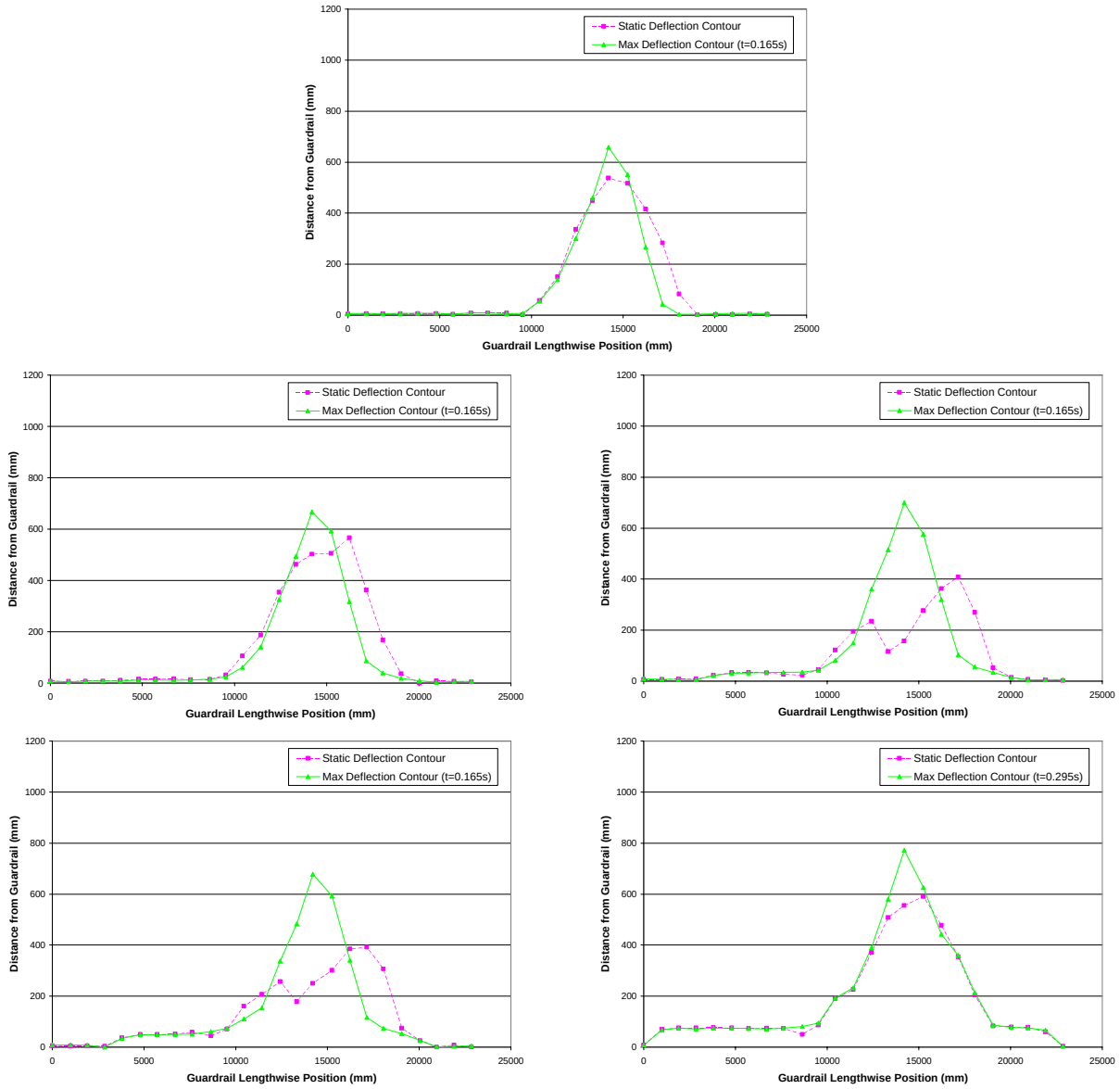

Figure 97: Guardrail damage contours for flattening simulations. Undamaged (top), 25% flattening (middle left), 50% flattening (middle right), 75% flattening (lower left), and 100% flattening simulations (lower right)

Figure 98 shows the energy balance over time for the undamaged and flattening simulations. For all of the simulations, the total energy was consistent (< 3% variation). The amount of energy remaining as kinetic energy varied greatly across the simulations, ranging from 29% for the undamaged simulation to 55.5% for the 100% flattening simulation. Potential

energy remained consistent throughout the simulations, but it is possible that the ratio of energy absorbed by the vehicle and the guardrail shifted as the degree of flattening increased.

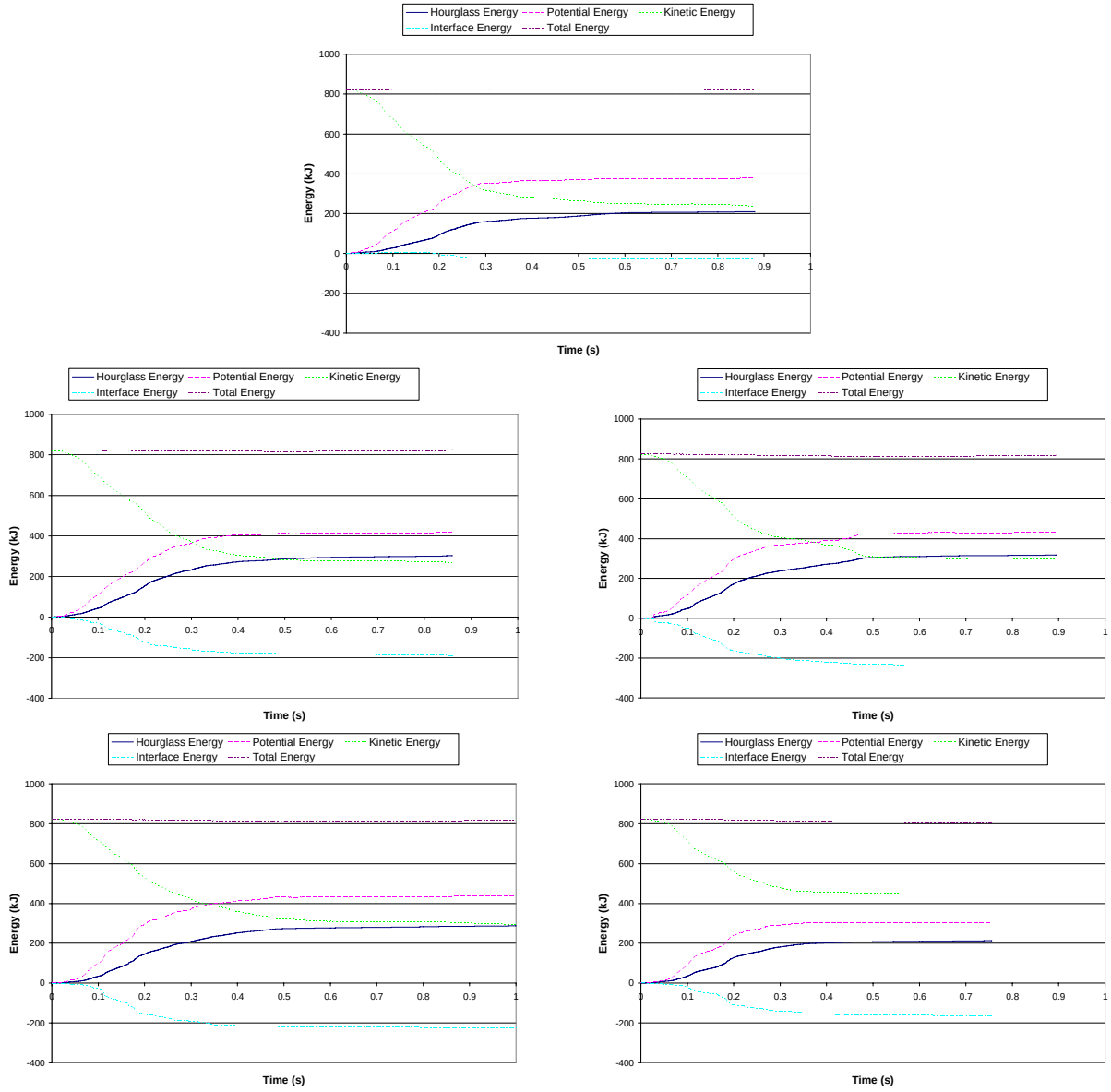

Figure 98: Energy balances for flattening simulations. Undamaged (top), 25% flattening (middle left), 50% flattening (middle right), 75% flattening (lower left), and 100% flattening simulations (lower right)

7.4 Discussion

A full series of simulations, with flattening ranging from 25 – 100%, were run to determine whether rail flattening posed a risk to vehicle and occupant safety. It was found that

the vehicle became unstable above 75% flattening. At 100% flattening, the vehicle rolled over as it exited the guardrail.

A key factor in the exit behavior of the vehicle was the motion of the front left tire. Figure 99 shows the vertical displacement of the center of the front left and rear left tires over time, relative to each tire's original position at the start of the simulation. The simulation of 100% flattening showed the greatest displacement of the tire, reaching over 1600 mm by the end of the simulation. Such a large change in the vertical position of the vehicle can be an indicator of vaulting. However, in this case the vehicle was redirected before this could occur. The undamaged simulation showed the lowest amount of vertical tire motion, which was an indicator of vehicle stability. In the plot of the front left tire displacement for the undamaged simulation, the time at which the wheel struck and rolled over a post can be easily discerned by the peaks in the displacement.

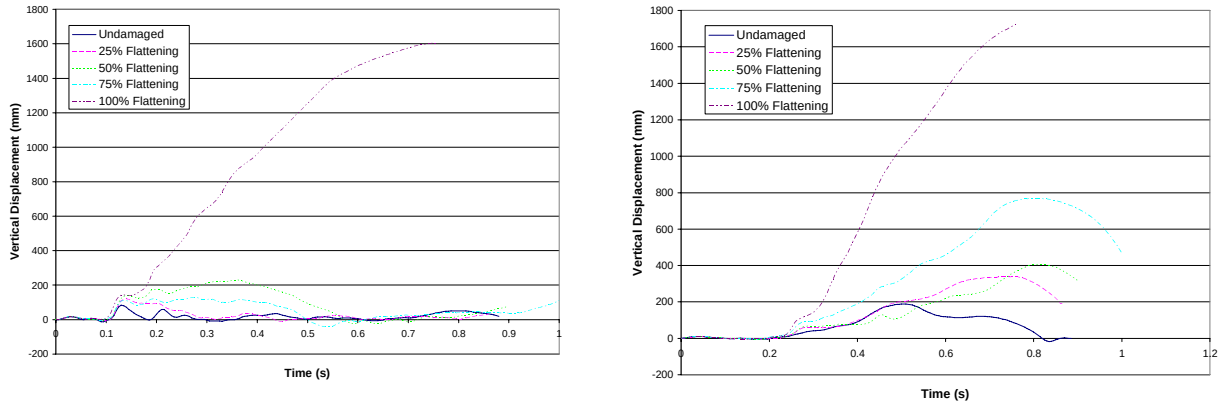

Figure 99: Displacement of vehicle tires for the flattening simulations. Front left tire (left) and rear left tire (right)

The vehicle instability at greater than 75% flattening was caused by the vehicle riding up the flattened rail. Both the flatness of the rail and the lower bottom height of the rail were contributors to the rollover. A shown in Figure 100, a maximally flattened rail extends both higher and lower than an undeformed rail would and also presented a much smoother surface.

In the undamaged simulation, the upward motion caused by the left tires hitting the post bases was counteracted by the downward force exerted by the rail. Because of the height of the rails, the collision force was concentrated on the front of the fender, leading to extensive crush on the front left corner of the vehicle. This deformation allowed the top half of the rail to penetrate the space above the front left tire. The presence of the rail above the tire provided a downward force that prevented the tire from moving upward.

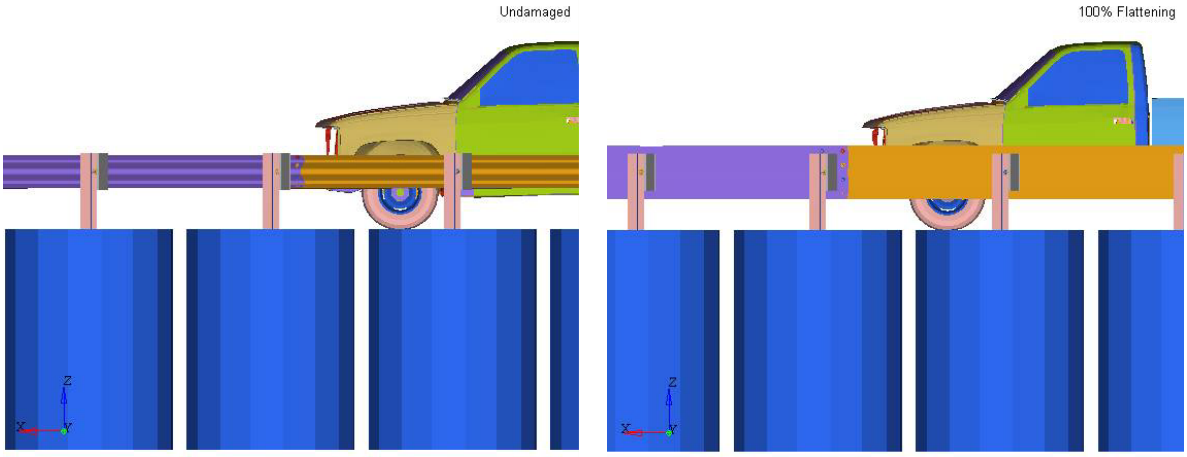

Figure 100: Height of the rails relative to the vehicle. Undamaged (left) and 100% flattening (right)

When the rail was 100% flattened, a different behavior was observed. Because of the higher top height of the rail and the flatness of the surface, the force of the collision was spread over a larger portion of the fender. These factors prevented the rail from penetrating the space above the tire. The lower bottom height of the rails also presented a problem. As the tire was forced upward by contact with the posts, the elevation of the tire increased so that the majority of the tire was on or above the rails. This, combined with a slight outward slope in the rail caused by the crash damage, provided a ramp for the tire to ride up. The increase in rail height, which was concentrated on the left side of the vehicle, imparted a rolling motion that the vehicle was unable to recover from.

The vehicle exit speed also varied by the degree of flattening. For the undamaged simulation the exit speed was 53 kph, whereas for the 100% flattening simulation the exit speed was 73 kph. It was believed that by flattening the rails before impact, the ability of the guardrail to absorb kinetic energy was being reduced. To check if this was the case, the energy absorbed by the vehicle and guardrail was broken down by components in Figure 101.

In the 100% flattening simulation, the guardrail absorbed roughly 40 kJ less than, or 83%, of the energy that was absorbed by the undamaged simulation. When broken down even further, it was found that the rails actually absorbed about 45 kJ less energy, but the other components of the guardrail absorbed 5 kJ more energy, resulting in the net drop in energy absorption of 40 kJ. The components of the guardrail that absorbed more energy were the posts and blockouts, as the flattening of the guardrail allowed the vehicle to engage these components more easily.

Figure 101 also showed the energy absorption of the vehicle for the two simulations. The rails mentioned in the legend are the rails between posts 9 and 21. The order of the rails, starting from post 9, was Rail, Rail 2, Rail 3, Rail 4, Rail 5, and Rail 6. There was a 40 kJ drop in energy absorption for the 100% flattening simulation. However, this time the energy drop was spread evenly among most of the parts of the vehicle in contact with the guardrail. The vehicle in the flattening simulation absorbed less energy because it spent less time in contact with the rail. This was due to the increase in vehicle height caused by the tire riding up the rail, pushing most of the vehicle body above the rail.

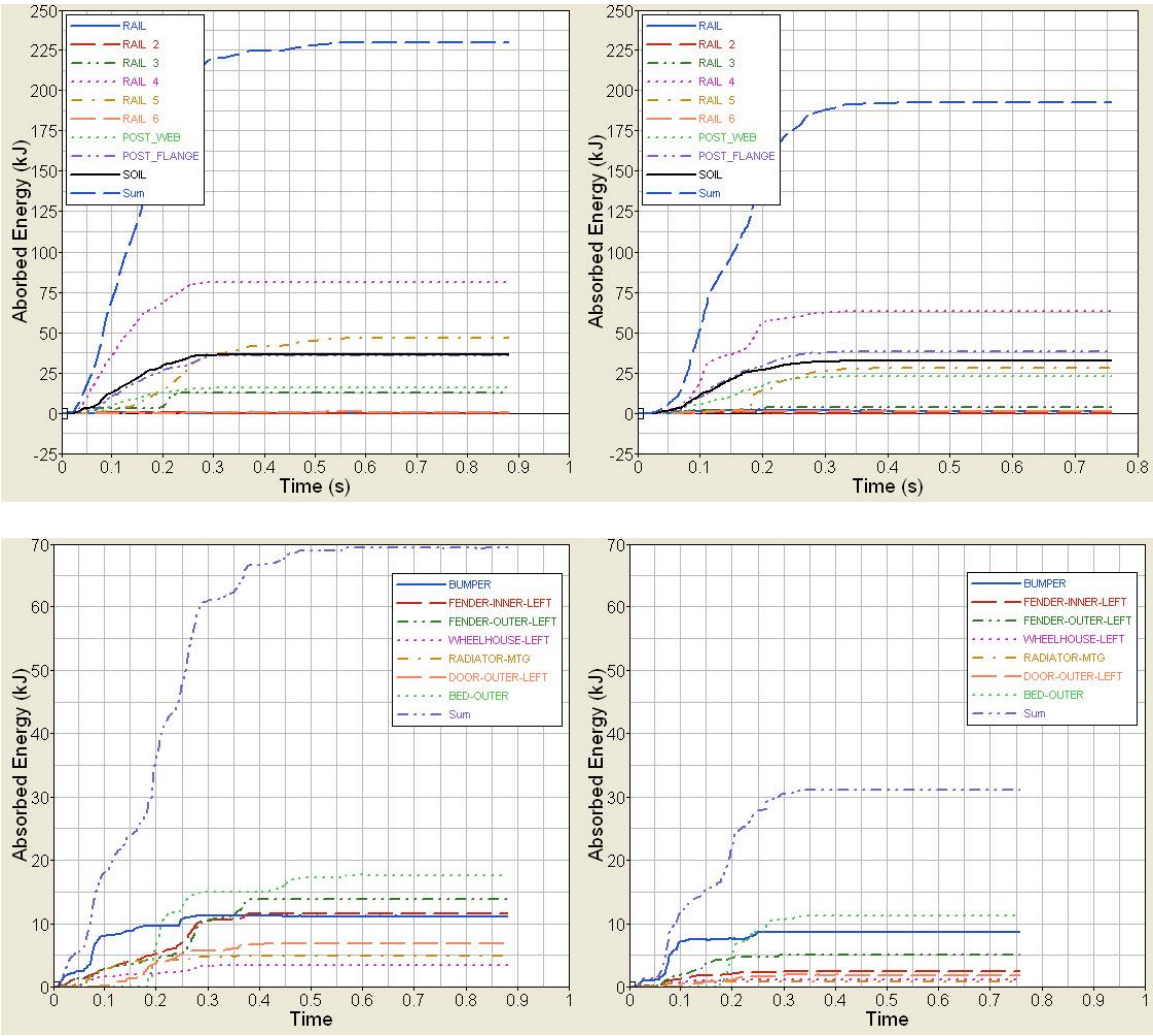

Figure 101: Energy absorbed by the guardrail components (top plots) and the vehicle (bottom plots). Undamaged (left) and 100% flattening (right)

Since it was believed that the flattened rails created a ramp-like surface, a supplementary simulation was performed to examine how the angle of the guardrail would affect the performance. The finite element model of 75% flattened rail was modified by bending the posts and rails in the area of contact backwards. This resulted in an 80 degree angle between the post and ground line rather than the standard 90 degrees, as shown in Figure 95. The slight incline in the rails was sufficient to cause the vehicle to both vault and roll. From these results, it was evident that the angle of the guardrail, whether caused by damage or pre-existing because of a sloped ground, could drastically alter the outcome of a crash. However, the same incline in an

otherwise undamaged guardrail had little effect on the outcome of the simulation. In the future, the full effect of combined incline and flattening may be examined in more detail.

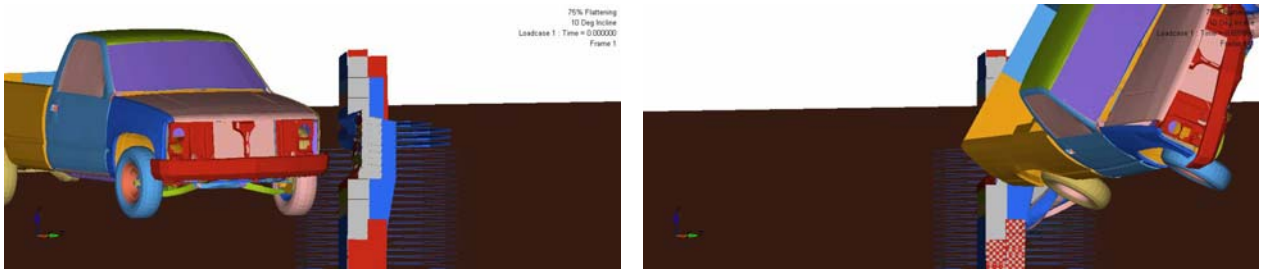

Figure 102: Simulation of 75% flattened guardrail leaning back by 10 degrees. Vehicle before impact on the left, and after the impact (t = 0.7s) on the right.

7.5 Conclusion

A series of simulations of impacts into flattened strong-post w-beam guardrail were run and compared to the performance of the undamaged guardrail simulation. The flattening in these simulations varied from 25% to 100%. Although vehicle roll and pitch increased with increasing degrees of flatness, the vehicle did not become unstable until the flattening was greater than 75%. At 100% flattening, the vehicle rolled as it exited from the guardrail.

The vehicle exit speed increased sharply with increasing flatness due to two reasons. First, the guardrail was not able to absorb as much energy because the rails were already flattened before impact. Second, the vehicle spent less time interacting with the guardrail, and therefore retained more of its initial energy, because the left tires tended to override the rails. This limited the energy loss due to crush to the vehicle body and friction losses.

Guardrail deflection increased with increasing flatness. The maximum deflection at 100% flattening was 0.8 meters, which was a 15.5% increase in deflection over the undamaged simulation. Even a small amount of flattening (25%) resulted in a 10% increase in deflection. While the increases to the maximum deflection were not as large as those observed for the

missing post simulations, there could be a significant risk if hazardous objects were placed directly behind the theoretical maximum deflection of the undamaged guardrail.

An aspect of rail flattening that was only briefly examined in this study was rail flattening concurrent with backwards slope of the guardrail. This type of combined damage increased the risk of vaulting, due to the creation of an inclined slope rather than a vertical face. The simulation of 75% flattening, which was marginal with completely upright posts and rails, failed by vaulting and roll when the rails and posts where angled backwards at an angle of 10 degrees. However, the same incline in the undamaged guardrail did not change the results for that simulation. Future work will be needed to more accurately determine the interplay of rail flattening and slope.

7.6 Recommendation for Rail Flattening

It is recommended that all guardrails for which there is 50% or greater flattening be repaired as soon as possible due to a greatly increased risk of vaulting and rollover. A more conservative limit of 50% was chosen over 75% because of the tendency of flattening to occur with other types of damage, as well as the extreme sensitivity of flattened guardrail to any deviation from a fully upright position. It should be noted, however, that this limit was defined for guardrails in which the flattened rail remained completely vertical. In the field, rail flattening can often occur with deflection. The resulting flattened and sloped rails increase the chance of the tires overriding the rail and the vehicle rolling and vaulting. For these conditions, a lower threshold for rail flattening should be considered. In any situations where there is a hazardous object directly behind the guardrail, the damage should be repaired immediately because even a

small amount of rail flattening increased the maximum deflection of the guardrail by roughly 10%.

8. POST SEPARATION FROM RAIL MODELS

8.1 Introduction

The final damage mode under consideration in this study was the separation of the post from the strong-post w-beam guardrail. This type of damage commonly occurs in combination with minor rail deflection, but in this study it was considered in isolation.

8.2 Methods

In order to test whether post and rail separation posed a significant risk to vehicle occupants, a way to create the initial damage was needed. The simulation used to create this damage is shown in Figure 103. In this simulation, the vehicle and rails were removed from the model, and a rigid cylinder was added. The cylinder was constrained from all rotation and vertical motion, and was given a controlled displacement to move it toward the posts. As the cylinder contacted the posts, it forced them to deflect backwards.

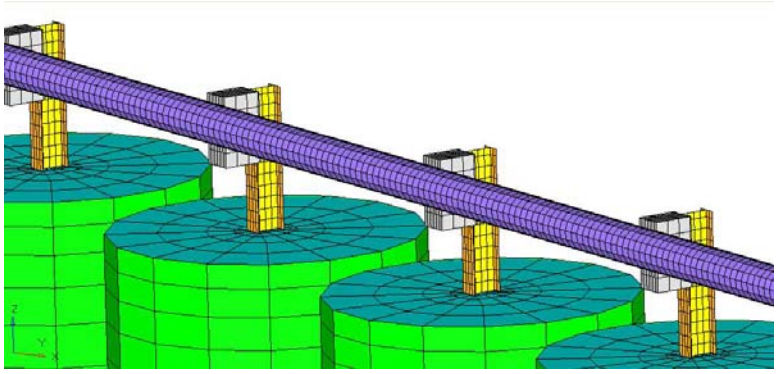

Figure 103: Simulation to cause rail and post separation

The damaged geometry from the simulation was exported at the time that corresponded to the desired level of post deflection, i.e. 3 inches. The damaged geometry was then imported into the finite element model of the undamaged guardrail system, with the deflected post replacing a previously undamaged one. The resulting models are in Figure 104. The vehicle was given the initial conditions specified by the NCHRP 350 test criteria. Thus, the vehicle initial velocity was 100 kph and the impact angle was 25 degrees.

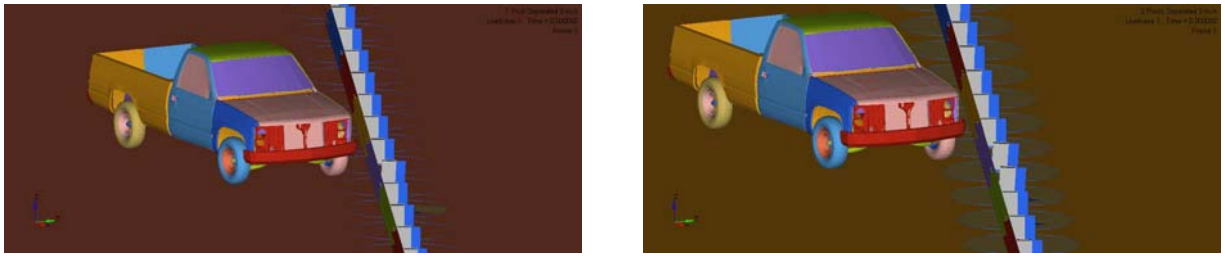

Figure 104: Simulations of the post separation from rail damage condition. 1 post separated by 3 inches (left) and 2 posts separated by 3 inches (right)

8.3 Results

The results of the rail and post separation simulations are summarized in Table 32. Many of the NCHRP 350 required criteria did not vary between the different simulations. The occupant impact velocity, occupant ridedown acceleration, and vehicle 50 ms moving average acceleration did not change between the undamaged and post-and-rail-separated simulations. The vehicle exit speed and angle were also unchanged.

The greatest changes between each of the simulations were observed in the vehicle rotation, particularly the roll and pitch. Both roll and pitch decreased as more posts were detached from the guardrail. However, lower values for roll and pitch were indicators of better vehicle stability.

There was also a small increase in the maximum amount of dynamic and static deflection in the guardrail system. However, the increases associated with the rail and post separation

damage mode were the smallest of all of the examined damage modes. The changes to the static deflection in particular may not have been significant as the maximum amount of static deflection actually decreased slightly between the 1 post separated 3 inches simulation and the 2 posts separated 3 inches simulation.

Table 32: Results for rail and post separation simulations

		Un-damaged	1 Post 3 Inches	2 Posts 3 Inches
Impact Conditions				
	Speed (kph)	100	100	100
	Angle (deg)	25	25	25
Exit Conditions				
	Speed (kph)	53	53	54
	Angle (deg)	14.5	14.8	14.8
Occupant				
	Impact Velocity X (m/s)	7.5	7.7	7.7
	Impact Velocity Y (m/s)	5.5	5.8	5.7
	Ridedown X (G)	-11.8	-13.1	-11.3
	Ridedown Y (G)	-12.3	-14.0	-12.0
	50 ms Average X (G)	-6.7	-7.3	-6.6
	50 ms Average Y (G)	-6.8	-7.2	-6.6
	50 ms Average Z (G)	-3.8	-2.6	-4.1
Guardrail Deflections				
	Dynamic (m)	0.69	0.70	0.73
	Static (m)	0.55	0.59	0.58
Vehicle Rotations				
	Max Roll (deg)	-14.4	-12.9	-10.0
	Max Pitch (deg)	-9.9	-8.8	4.6
	Max Yaw (deg)	40.3	40.8	41.0

Table 33 presents the results of the rail and post separation simulations as a percent change from the undamaged simulation, rather than as absolute values. The minimal change in test results caused by this damage mode is evident, as many fields have changed by less than 5% for both of the simulations. As mentioned previously, the greatest changes were observed for the vehicle roll and pitch, which decreased 30.6% and 53.5%, respectively.

Table 33: Percent change of rail and post separation simulations from undamaged simulation

		1 Post 3 Inches	2 Posts 3 Inches
Impact Conditions			
	Speed (kph)	0.0%	0.0%
	Angle (deg)	0.0%	0.0%
Exit Conditions			
	Speed (kph)	0.0%	1.9%
	Angle (deg)	1.9%	1.7%
Occupant			
	Impact Velocity X (m/s)	3.1%	2.8%
	Impact Velocity Y (m/s)	4.3%	2.5%
	Ridedown X (G)	11.0%	-4.4%
	Ridedown Y (G)	14.3%	-2.3%
	50 ms Average X (G)	9.5%	-1.2%
	50 ms Average Y (G)	5.1%	-2.7%
	50 ms Average Z (G)	-32.6%	7.7%
Guardrail Deflections			
	Dynamic (m)	1.6%	5.6%
	Static (m)	6.9%	4.2%
Vehicle Rotations			
	Max Roll (deg)	-10.4%	-30.6%
	Max Pitch (deg)	-11.1%	-53.5%
	Max Yaw (deg)	1.2%	1.7%

In Figure 105, the vehicle rotations (roll, pitch, and yaw) are shown. All of the simulations showed the same trends. As mentioned earlier though, the simulation of two posts separated by 3 inches showed that the minor damage to the guardrail improved the vehicle stability by lowering both the roll and pitch. As a consequence, the vehicle also returned to the neutral position at roughly 600 ms, which was faster than for the other two simulations which reached the neutral position at roughly 750 ms. The yaw did not vary between the three simulations.

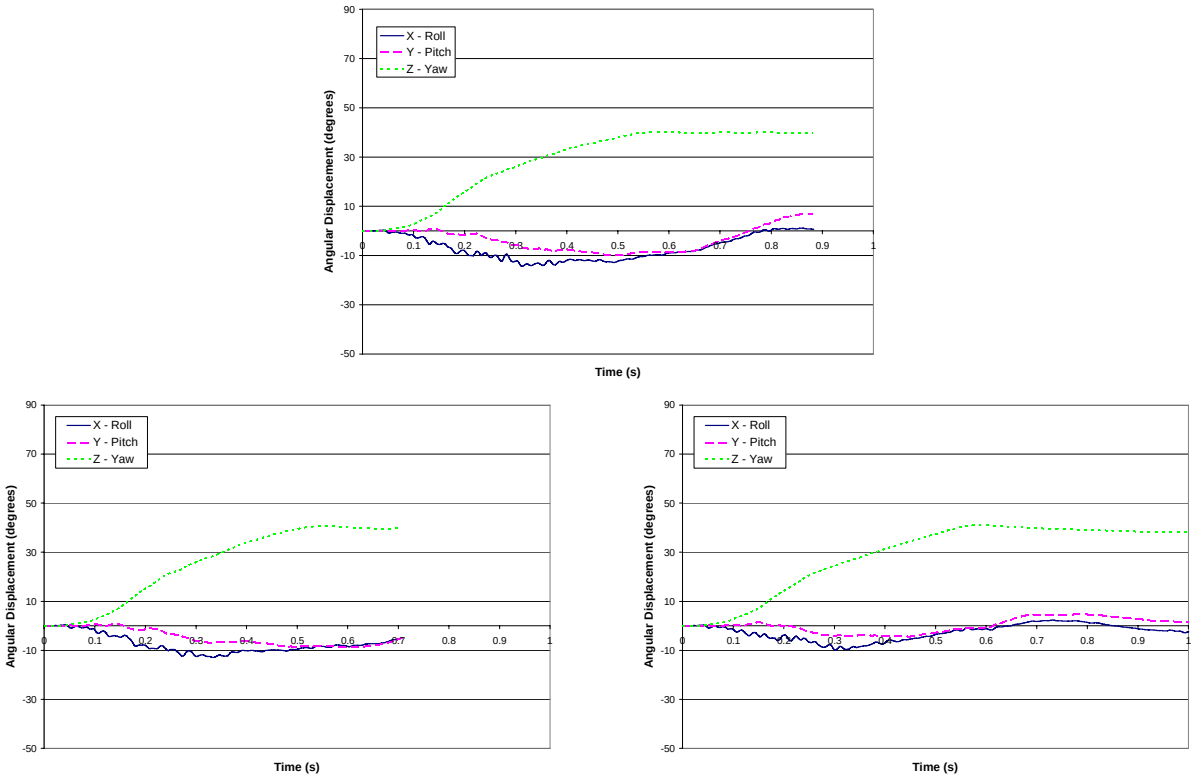

Figure 105: Roll, pitch, and yaw for post and rail separation simulations

The vehicle velocities, shown in Figure 106, were also very similar between all three simulations. There was a noticeable amount of lateral skidding during the impact (in the range of 50 – 400 ms) that died out as the vehicle began to exit the guardrail. The exit speed for the vehicle was completely unaffected by the minor damage and ranged between 53 and 54 kph.

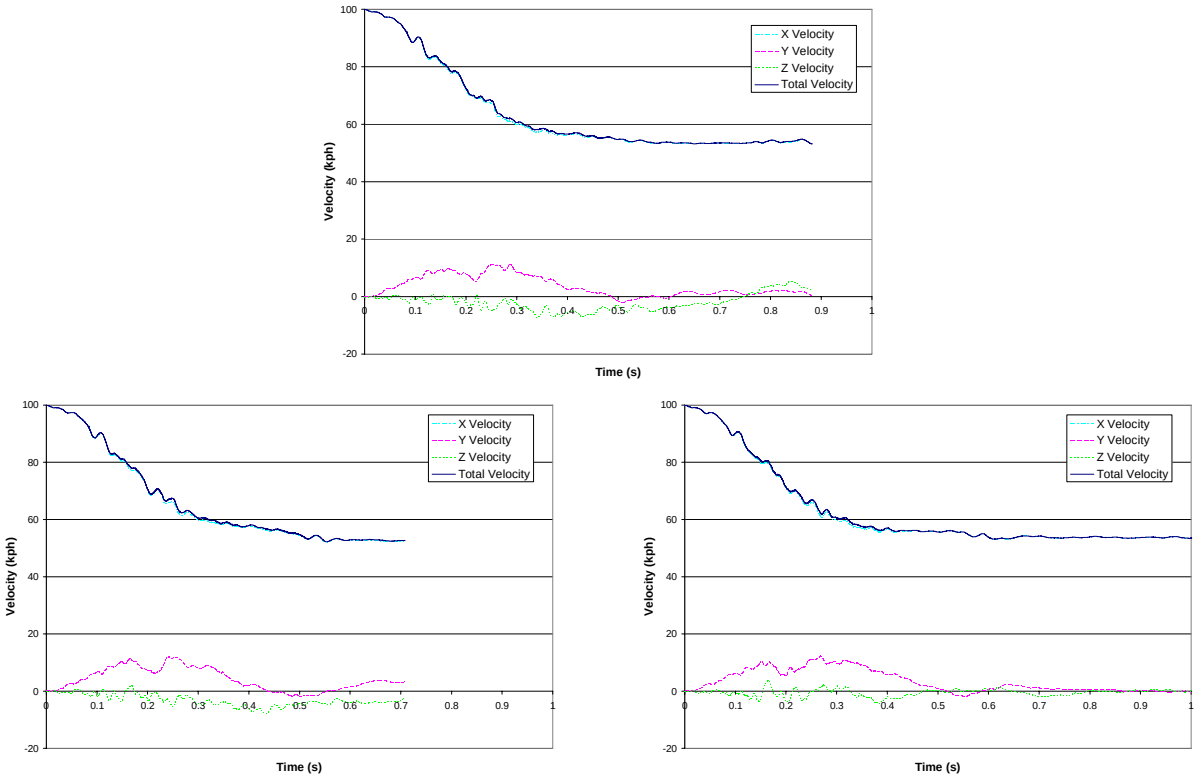

Figure 106: Vehicle velocities for post and rail separation simulations

The guardrail deflection did not vary much between the simulations of post and rail separation and the undamaged simulation. As shown in Figure 107, all of the simulations resulted in a maximum dynamic deflection of roughly 0.7 meters and maximum static deflections around 0.55 meters.

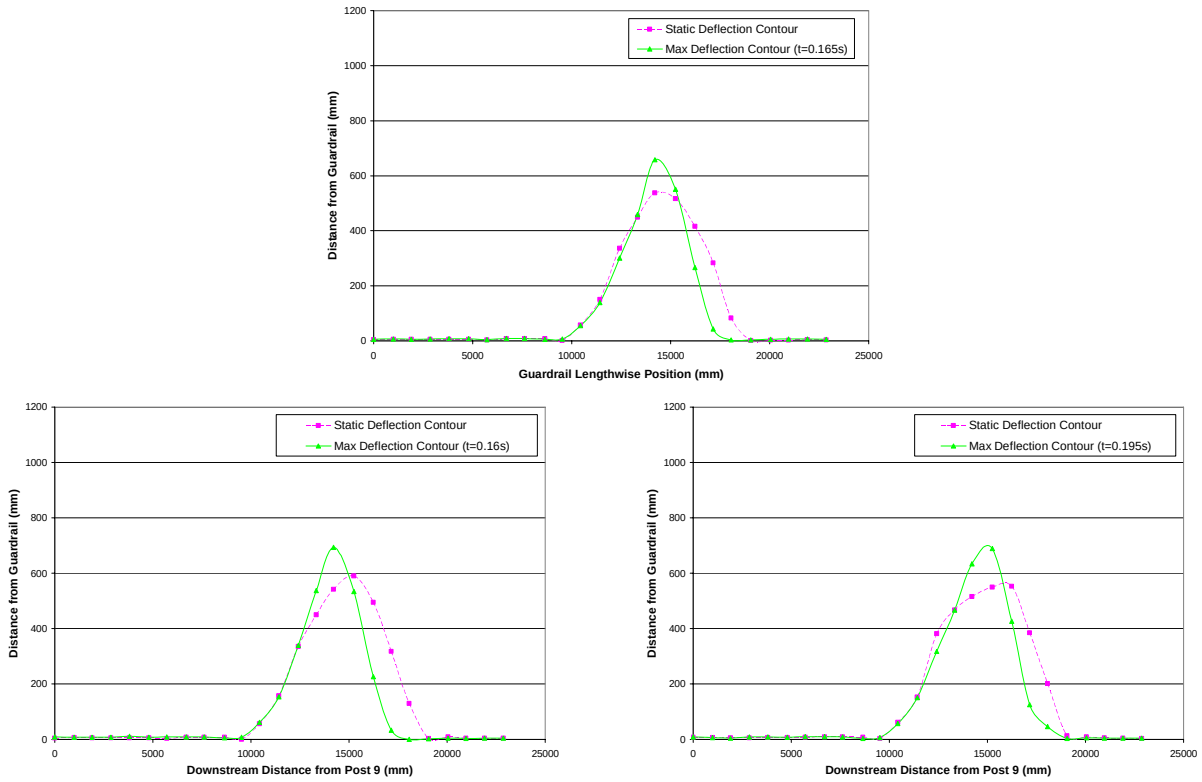

Figure 107: Guardrail damage contours for post and rail separation simulations

Figure 108 shows the balance of energy over time for each simulation. All of the simulations showed very little variability in the total amount of energy in the simulation. The difference between the energy at the beginning (t = 0 ms) and the end was less than 1% for all three simulations. While the kinetic energy was the same for all three simulations, there were variations in the interface, hourglass, and potential energies between the 1 post and 2 post separation simulations. As more energy was absorbed by the interfaces, the amount of energy stored in hourglassed elements and deformed elements increased. The parts contributing the most to these changes were the two rails in contact with the vehicle and the front-left tire rim.

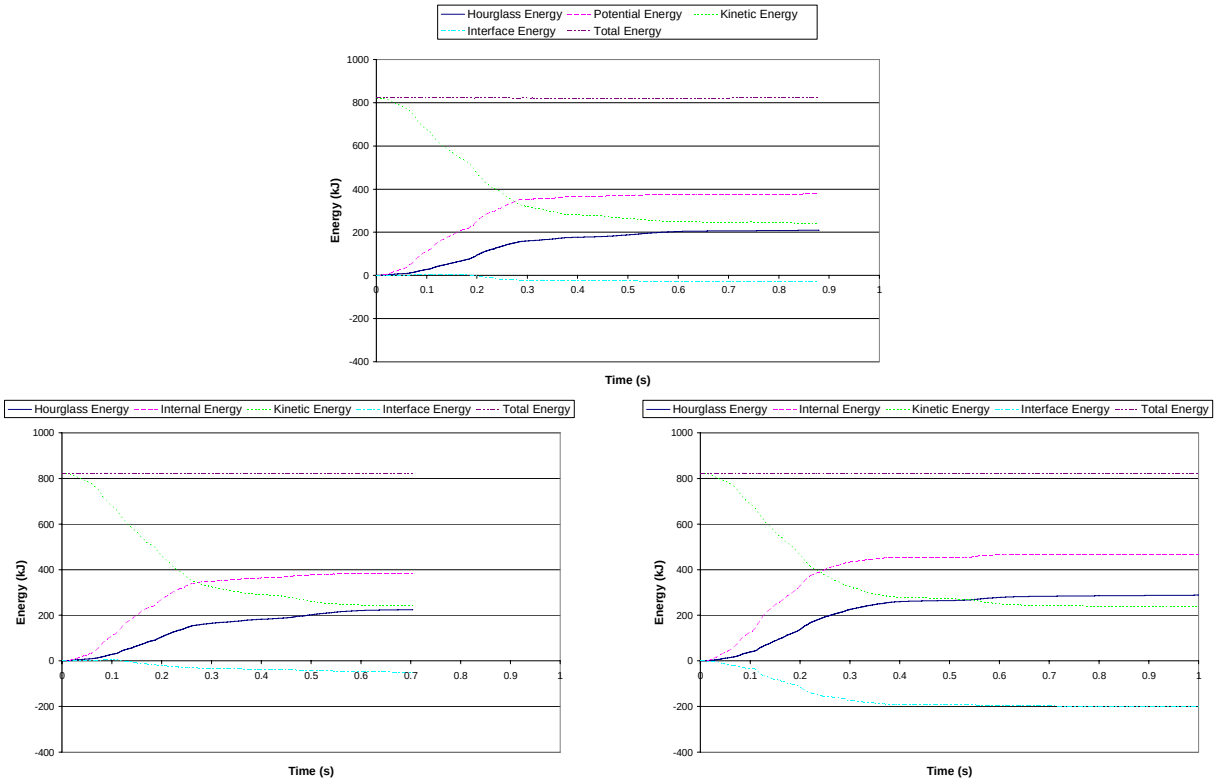

Figure 108: Energy balances for rail and post separation simulations

8.4 Discussion

Two simulations were run to evaluate the effect of a specific minor damage mode: post and rail separation. The first simulation modeled the effect of one post separated by 3 inches and the second simulation modeled two posts separated by 3 inches. Intuitively, it was expected that the introduction of damage into the guardrail would worsen the overall performance. However, this damage mode was found to have little effect, and possibly even some benefit, to the safety of the vehicle and its occupant.

The reason that the existence of rail and post separation could possibly be construed as beneficial was the resulting reduction in the vehicle roll and pitch. For the simulation including two separated posts, the pitch dropped by approximately 50%. However, it should be noted that the roll and pitch of the vehicle in the undamaged simulation were already relatively small (10

degrees or less). In absolute terms, the 50% decrease in pitch was actually a decrease of 5 degrees in the vehicle pitch, i.e. the pitch was 10 and dropped to 5 degrees. The vehicle yaw was not affected by the pre-existing damage, resulting in vehicle exit conditions that were nearly identical for all of the simulation.

The maximum deflection of the guardrail itself did not change greatly as more posts were separated from the rail. The most severe damage condition modeled, which was two posts separated by 3 inches, resulted in a 5.6% increase in maximum dynamic deflection. The increases associated with rail and post separation were smaller than those of the missing post, rail and post deflection, and rail flattening damage conditions. It was interesting that the increase in maximum dynamic deflection for the simulation of one separated post increased by 0.1 meters, which was roughly the same amount by which the damage post was deflected (3 inches ≈ 0.012 cm).

The minimal effect of rail and post separation on the crash simulation results appeared reasonable. By design, the posts and rails in strong-post systems are supposed to separate during impact. By allowing separation, the posts and rails can deform by large amounts without the rails being pulled down toward the ground. Because the posts were not connected to the rails, the posts could deform more freely and reduce the risk of the vehicle snagging on the posts. The posts were still able to provide a significant amount of lateral resistance to deflection even though they were not attached to the rail. Because of these factors, the ability of the guardrail to redirect the vehicle and absorb crash energy was not significantly reduced.

8.5 Recommendation for Rail and Post Separation

The simulations conducted for this study indicate that the separation of up to two adjacent posts from the rails of the guardrail did not pose a risk to the vehicle or occupant. Indeed, it was found that there was minimal effect on the crash performance from this damage mode. For maintenance and repair of guardrails, this particular damage condition would be the lowest priority.

9. CONCLUSIONS

Strong-post w-beam guardrails are currently used extensively throughout the country to protect vehicles and their occupants from roadside hazards. All guardrail installations on highways are tested under the NCHRP 350 test level 3 protocols to demonstrate that the guardrail installations themselves pose minimal risk. Testing is often performed with a pickup truck such as the Chevrolet 2500, with the initial conditions for the vehicle being a 25 degree angle of impact at 100 kph. These tests are evaluated for both guardrail and vehicle performance.

A limitation of the crash testing process is that the guardrails that are tested are always newly installed, undamaged guardrail. Once installed alongside roadways, the guardrail may be impacted numerous times in its lifespan, ranging from minor to catastrophic damage. While the dangers of leaving extensive damage to the guardrail unaddressed are understood, there is relatively little known about the effects of minor damage on the guardrail performance.

This study was developed to examine the effects of minor damage modes on the performance of strong-post w-beam guardrail and the safety of the vehicle occupants. The damage modes under consideration were missing posts, rail and post deflection, rail flattening, and post and rail separation. Each of these damage modes was considered in isolation to better ascertain how each type of damage affected the crash test results, even though the types of damage typically occur together in the field. The evaluation of combined damage modes would be an excellent area for future study.

Because real, full-scale crash tests are expensive and time consuming, the finite element approach was used. Basic finite element models of a Chevrolet 2500 and a strong-post w-beam guardrail were obtained from the NCAC finite element library and modified to represent a crash test of the desired minor damage mode. The vehicle model was adapted to match the dimensions of vehicles used in the crash tests obtain for validation purposes.

To demonstrate that the finite element model was capable of accurately predicting the results of a crash test, a real crash test was needed. The crash test TTI 405431-1, in which a Chevrolet 2500 pickup truck impacted an undamaged strong-post w-beam guardrail at test level 3 conditions, was chosen as the validation test. The finite element simulation was able to reproduce the outcome of the crash test as well as similar values for the NCHRP 350 test criteria. However, the finite element model of the guardrail was stiffer than the real guardrail and the resulting deflection was lower. An alternative means of evaluating the guardrail deflection was developed: the percentage change between the simulation of a minor damage mode and the undamaged guardrail simulation would be used to compare the guardrail performance rather than the absolute value of the deflection. The maximum observed rail tension for the undamaged simulation was 237 kN.

To demonstrate that the finite element approach could be used to predict the effect of missing posts, a crash test of a long-span system was used for validation. The simulation of the same crash test was matched to the simulation results. Following this, a series of simulations with one, two, and three posts missing were developed. Two impact points were considered. The removal of posts greatly increased the vehicle pitch and tire snagging. The point of impact relative to the nearest downstream post also had a strong effect on the test outcome and potential

for snagging. Because of these results, it was recommended to not allow any missing post damage to persist in a guardrail.

Rail rupture was a major concern in guardrails with missing posts. In many real crash tests, this concern was so great that nesting of rails was used to improve the rail tensile capacity. The tension carried by the rails in the simulation, which were not nested, was tabulated to determine if rupture was more likely. For the one, two, and three post missing simulations, the rail tension peaked at 268 kN, 299 kN, and 353 kN respectively. From these tension results, it was believed that the removal of posts from the guardrail represents an increased risk of rail rupture. However, the finite element solver used for these simulations was not well suited for predicting whether rupture would have occurred.

Rail and post deflection, which was the most common type of damage in guardrails, was also considered. To demonstrate that the finite element approach was suitable to predicting the crash test results for these guardrails, the MGA Research Corporation was contracted to perform a crash test into damaged guardrail. This crash test consisted of a first impact resulting in 14.5 inches of rail and post deflection followed by a second impact that resulted in the vehicle vaulting over the guardrail. Simulations for both of these impacts were developed and the outcome of the real crash test was successfully reproduced using finite element simulations.

To identify the limit of acceptable rail and post deflection, a series of simulations was developed to evaluate guardrails with less than 14.5 inches of deflection. Simulations were developed for rail and post deflection of 3, 6, 9, and 11 inches and for rail only deflection of 3 and 6 inches. The rail only deflection simulations showed little change in vehicle and occupant response compared to the undamaged simulation. The simulations of rail and post deflection predicted successful redirection of the vehicle despite the minor damage in the guardrail, even

for the most severe case considered which was 11 inches. Increases in the maximum amount of dynamic deflection were observed, reaching 13% higher for the 11 inch simulation. Although not as severe as the increases observed when the guardrail was missing posts, pre-existing deflection still represents a risk of interaction with objects behind the guardrail.

To better understand why there was such a difference in the outcomes between the 11 inch simulation and MGA simulation (14.5 inches), the post separations and rail heights were observed. The failure of a post in the area of contact to detach from the rail was believed to a major factor in the outcome of the MGA crash test. In the remaining simulations, all of the posts in the area of contact separated during the full-scale impact. The post that remained attached in the MGA test was observed to pull the rail downward, enabling the vehicle to vault over the guardrail. The minimum height of the rails after the second impacts were tabulated for all simulations and was found to be far lower in the MGA simulation than for any other. The vehicle bumper height was the other major factor, as the vehicle used for the MGA crash test and simulation was nearly 50 mm higher than the bumper height of the vehicle used in the remaining simulations.

Isolated rail flattening was examined in increments of 25%, ranging from 25% to 100% flattening. Flattening was found to be dangerous only for the highest degrees of flattening. Although the stability of the vehicle worsened as the amount of flattening in the rail increased, the vehicle did not roll over until the flattening in the rails exceeded 75%. The rail flattening and increased vertical motion of the vehicle lowered the amount of kinetic energy absorbed in the crash. As a result, the exit speed of the vehicle was noticeably higher for the flattened guardrails, with the exit speed peaking at 73 kph for 100% flattening. The maximum guardrail deflection also increased by 15% for 100% flattening.

The primary mode of failure for flattening damage was found to be rollover due to the vehicle overriding the rails. Although override implied a risk for vaulting, none was observed as the flattened guardrails were still capable of redirecting the vehicle. However, there was significant vertical motion, particularly in the impact side of the vehicle, which contributed to the roll of the vehicle. Some additional simulations were performed that indicated that the outcome of crashes into flattened rails were extremely sensitive to deviations from a completely vertical orientation of the rails and posts.

Separation of posts and rails proved to be less risky than the other damage modes. The roll and pitch of the vehicle actually decreased slightly as more posts were detached from the rail by a slight amount. The maximum deflection also increased by roughly 5% for the most severe damage simulation, in which 2 posts were separated by 3 inches. The remaining test criteria were virtually unchanged between the simulations of post and rail separation and the simulation of the undamaged guardrail. However, strong-post guardrail is supposed to allow the posts and rails to separate during impact by design. Thus, this damage mode was not as severe as might initially be thought.

9.1 Recommendations

Based on the results, a set of recommendations were developed for which damage modes need to be repaired and how such repairs should be prioritized. These repair recommendations are shown in Table 34. Post and rail deflection over 6", rail flattening over 50%, and missing posts were the most dangerous of all the damage modes simulated and therefore are the highest priority to repair. Because all of these damage modes result in significant increases in maximum

guardrail deflection, priority within this group of damage modes would be given to any guardrail with a hazardous object directly behind the guardrail.

Table 34: Recommendations for guardrail repair

Damage Type	Damage Extent	Repair Recommendations
Post and Rail Deflection	Up to 6", lateral	When convenient
	Over 6", lateral	Immediately
Rail Deflection Only	Up to 6", lateral	When convenient
Rail Flattening	Up to 50% of section width	When convenient
	Over 50% of section width	Immediately
Post Detached from Rail	Up to 2 posts, 3" separation	None
Missing Posts	1 or more missing posts	Immediately

Rail and post deflection up to 6", rail deflection only, and rail flattening up to 50% were all damage modes that showed some degradation in the performance of the guardrail. Because of this, all of these damage modes would be lower priority repairs than the other damage modes. Although the increases in maximum guardrail deflection were not as large as for the higher priority damage modes, there were still noticeable increases in the deflection. Repair within this group of damage modes should be similarly prioritized if objects are present behind the guardrail.

The post separation damage mode was the least dangerous of all of the damage modes considered in this study. While there were small increases in the maximum deflection of the guardrail, there was also an improvement in the vehicle stability, particularly in roll and pitch. This improvement was due to the ease with which the separated posts can deform freely. However, these results should not be extended to situations in which larger numbers of posts are separated, due to the increased chance for rail sag.

10. REFERENCES

1. H. E. Ross, D. L. Sicking, and R. A. Zimmer, *National Cooperative Highway Research Program Report 350 Recommended Procedures for the Safety Evaluation of Highway Features*, Transportation Research Board, National Academy Press, Washington D.C., 1993.
2. NCHRP, *National Cooperative Highway Research Program Report 230 Recommended Procedures for the Safety Performance Evaluation of Highway Appurtenances*, Transportation Research Board, National Research Council, Washington D.C, 1981.
3. D. L. Bullard, W. L. Menges, and D. C. Alberson, *NCHRP 350 Compliance Test 3-11 of the Modified G4(1S) Guardrail with Timber Blockouts*, TTI 405421-1, FHWA-RD-96-175, Texas Transportation Institute, College Station, TX, September 1996.
4. AASHTO-AGC-ARTBA Joint Committee, *A Guide to Standardized Highway Barrier Hardware*, http://aashtotf13.tamu.edu/index.htm.
5. H. C. Gabler, D. J. Gabauer, and W. Wu, *Criteria for Restoration of Longitudinal Barriers*, Interim Report for NCHRP 22-23, August 2007.
6. NCAC, *NCAC Finite Element Archive*, http://www.ncac.gwu.edu/vml/models.html, Accessed 2/12/2009.
7. NCAC, *Finite Element Model of C1500 Pickup Truck*, http://www.ncac.gwu.edu/vml/archive/ncac/vehicle/c2500pickup-0.7.pdf, Accessed 3/2/2009.

8. D. Marzougui, P. Mohan, C. Kan, *Evaluation of Rail Height Effects on the Safety Performance of W-Beam Barriers*, 6th European LS-DYNA User's Conference, Gothenberg, May 2007
9. LSTC, *LS-DYNA Keyword User's Manual Version 970*, Livermore Software Technology Corporation, April 2003.
10. R. P. Bligh, et. al., *Dynamic Response of Guardrail Systems Encased in Pavement Mow Strips*, FHWA/TX-04/0-4162-2, Texas Transportation Institute, January 2004.
11. M. H. Ray, C. A. Plaxico, and K. Engstrand, *Performance of W-Beam Splices*, Transportation Research Record 1743, Transportation Research Board, pp. 120-125, 2001.
12. K. A. Polivka, et. al., *Development of a 7.62-m Long Span Guardrail System*, Transportation Research Report No. TRP-03-72-99, Midwest Roadside Safety Facility, University of Nebraska-Lincoln, April 1999.
13. K. A. Polivka, et. al., *Development of a 7.62-m Long Span Guardrail System – Phase II*, Transportation Research Report No. TRP-03-88-99, Midwest Roadside Safety Facility, University of Nebraska-Lincoln, August 1999.
14. C. E. Buth, D. L. Bullard, and W. L. Menges, *NCHRP Report 350 Test 3-11 of the Long-Span Guardrail with 5.7 m Clearance Span and Nested W-Beams over 11.4 m*, TTI 405160-1-1, July 2006.
15. D. J. Gabauer and H. C. Gabler, *Evaluation of Current Repair Criteria for Longitudinal Barrier with Crash Damage*, Journal of Transportation Engineering, Vol. 135, No. 4, pp. 225-234, 2009.

16. MGA Research Corporation, *1997 Chevrolet 2500 Pickup Impact with the Strong Steel Post W-Beam Guardrail – Part 1*, MGA Reference No. C08C3-027.1, August 2008.

17. MGA Research Corporation, *1997 Chevrolet 2500 Pickup Impact with the Strong Steel Post W-Beam Guardrail – Part 2*, MGA Reference No. C08C3-027.2, August 2008.

APPENDIX A: MATERIAL PROPERTIES OF RAIL STEEL

Introduction

In finite element models, the behavior of any object under loading is dependent upon many different parameters. One of the most important is the material definition that defines the stress-strain relationship for each of the components in the finite element model. Due to the variations in material properties and testing procedures, it is possible to have several different material definitions for a sample specimen. It can be difficult then to decide which of the many material definitions available should be used.

During the development of the finite element guardrail model for use in NCHRP 22-23, three different material definitions were found for the steel used to make the w-beam rail sections. All of these materials utilized the LS-DYNA piecewise linear plastic material model (MAT_024). The first material definition, published by Wright (1), was generated via coupon testing of guardrail steel. The second material definition was obtained from the NCAC finite element guardrail model. The ultimate source data used to create this material definition is unknown. The third and final material definition, developed by Reid and Sicker (2), was also obtained from coupon testing. The goal of this study is to determine which of these materials was best suited for use in a full-scale simulation of a guardrail collision.

Methods

A finite element model of a pendulum test was developed to test the accuracy of each of the three material definitions. This pendulum model is shown below in Figure 109. This model contains the pendulum, w-beam, posts, and steel cables used in the real NCHRP 22-23 pendulum

tests. There was one splice in the model, held together by spotwelds (4 welds in each splice hole). The post bolts were explicitly modeled as rigid materials, with the nut and bolt held together by a spring. As the objective was to select a material model, only the material definition for the w-beam sections was changed between simulations. All other aspects of the model remained the same.

An additional way in which the w-beam material model could be validated would be to compare the results to a real pendulum impact, such as a test performed as part of NCHRP 22-23 at the FOIL testing facilities (3). The pendulum setup is shown below in Figure 110. In these tests, a 2000 kg pendulum impacts a small section of guardrail. This guardrail was supported by two posts and was tensioned on the ends by steel cables connected to two large fixed bodies on either side. Due to the constrained space, only one splice joint was used. Each post was embedded in a stiff soil representative of the highly compacted soil specified by NCHRP 350. After the pendulum test, the deformation to the guardrail steel can be measured and used to validate a material model.

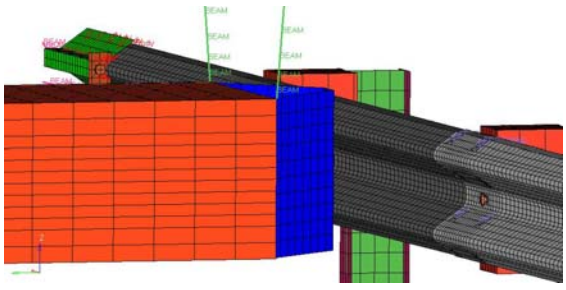

Figure 109: Pendulum finite element model

Figure 110: FOIL 2000 kg pendulum

Three different sets of elastic-plastic material definitions for the guardrail steel were evaluated for the rails. Each of the material models under consideration is shown below in Table

35. The first material, referred to as the NCAC material, came with the pre-made guardrail model that was available from the NCAC finite element archive. The second material came from a series of coupon tests published by Wright (1). The third material was also created from coupon testing performed by Reid and Sicking (2). While the density and modulus were fairly consistent between all the different materials, the yield stress and Poisson's ratio varied.

Table 35: Material Definitions

	NCAC Properties		**WPI Properties (1)**		**TTI Properties (2)**	
Material Type	MAT24		MAT24		MAT24	
Density (Mg/mm^3)	$7.89E^{-9}$		$7.86E^{-9}$		$7.86E^{-9}$	
Modulus (MPa)	200,000		200,000		200,000	
Poisson's Ratio	0.30		0.33		0.28	
Yield Stress (MPa)	298		415		450	
Failure Strain	$1.10E^{8}$		0.66		None	
Strain Hardening	Yes (C=90, P=4.5)		No		No	
	Strain	**Stress**	**Strain**	**Stress**	**Strain**	**Stress**
Stress-Strain Pt. 1	0.00	298	0.00	415	0	450
Stress-Strain Pt. 2	0.02	340	0.02	415	0.025	508
Stress-Strain Pt. 3	0.04	370	0.08	548	0.049	560
Stress-Strain Pt. 4	0.08	415	0.165	575	0.072	591
Stress-Strain Pt. 5	0.16	480	0.33	585	0.095	613
Stress-Strain Pt. 6	0.32	575	0.49	595	0.140	643
Stress-Strain Pt. 7	0.64	810	0.66	600	0.182	668
Stress-Strain Pt. 8			1.00	0	0.750	840

The greatest differences in the three material models were observed in the stress-strain curve that defines the plastic stress-strain region of the steel. To illustrate, a graph of the three material curves is shown in Figure 111. The were large differences at all of the strains for which data was collected.

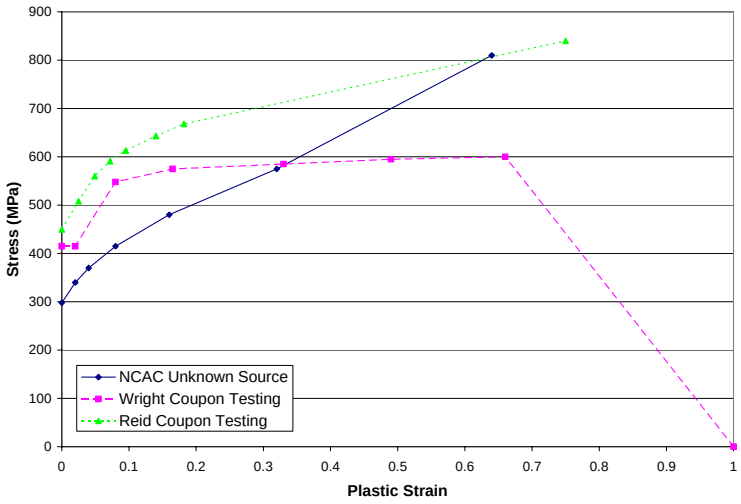

Figure 111: Plastic region stress-strain curves

Each of the three materials was evaluated in a pendulum simulation. The simulations were run for 500ms, which was a sufficient time to capture the entirety of the first pendulum impact. For each model, the maximum deflection of the rails was recorded by observing the displacement of a selected node relative to its original position.

Results

The results of the simulations are shown below in Figure 112 - Figure 114. Each figure shows the pendulum finite element model at the time of maximum deflection. On the right side of each figure is the plot of nodal displacement for node 86892. This node is the node located on the highest point on the rail section, and is precisely aligned with the nose of the pendulum. Deflection peaked in all the models between 0.12 and 0.13 seconds.

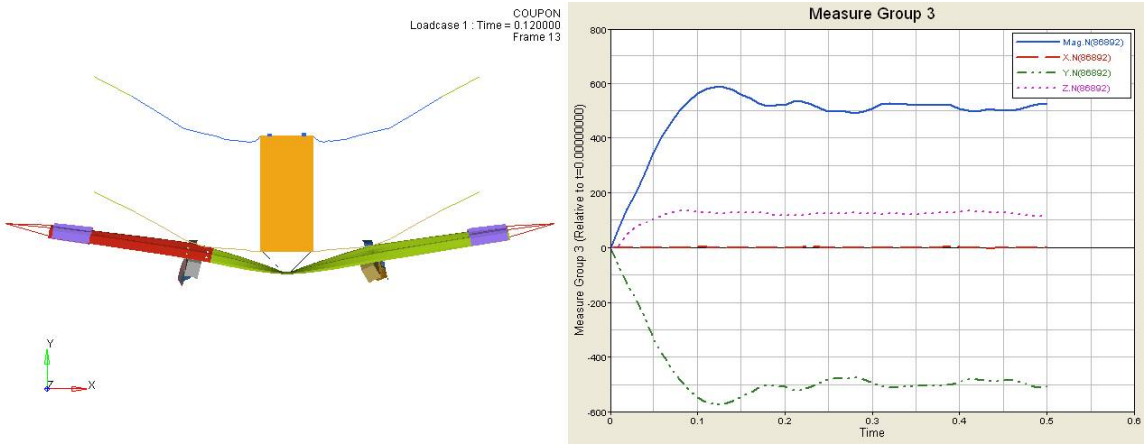

Figure 112: Pendulum Model with coupon test material

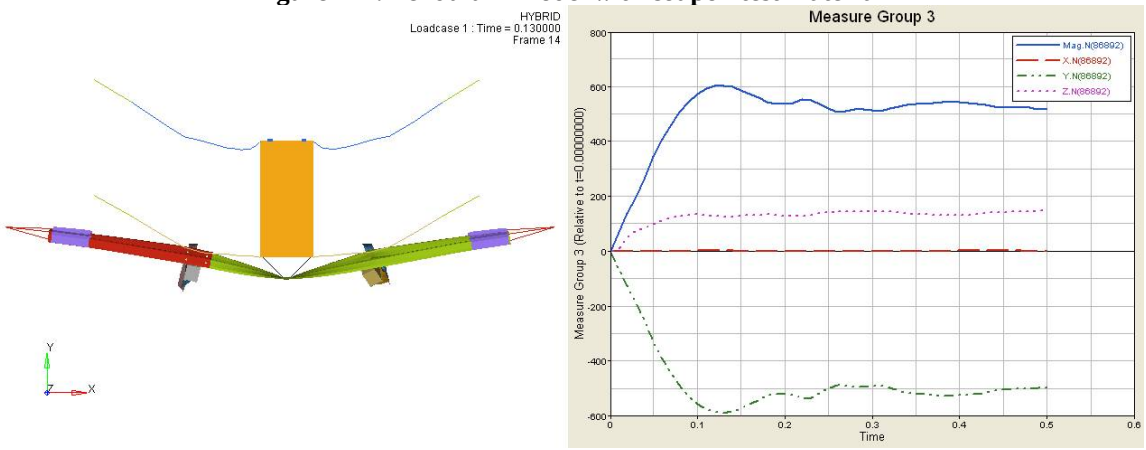

Figure 113: Pendulum model with hybridized material

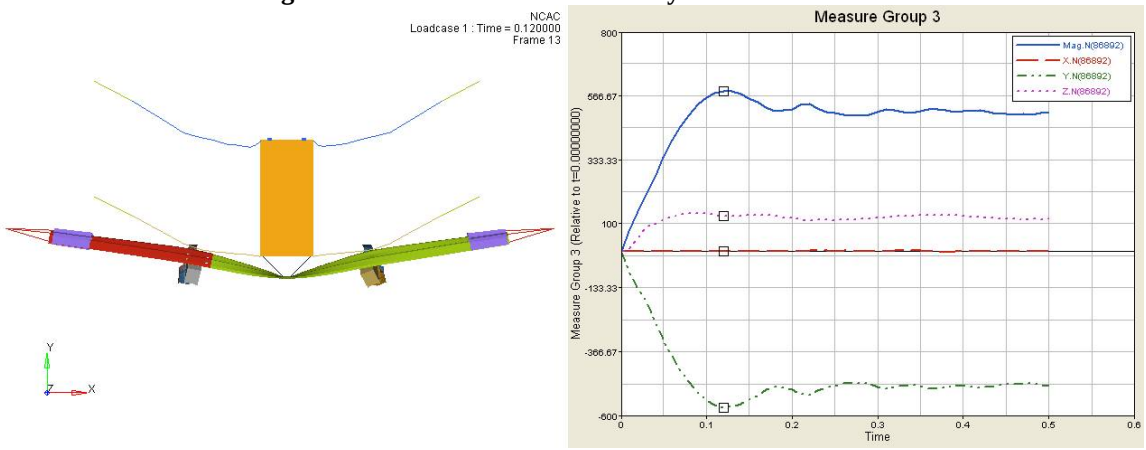

Figure 114: Pendulum model with NCAC material

Table 36 shows the deflection values for the aforementioned node at the time of maximum deflection and after the impact. Despite the large differences in certain material properties (notably: failure strain and yield strain) there was only a 3% difference between the

maximum deflections of the coupon material and hybrid material. The difference in static deflection between these same materials was only ~1%. The maximum deflection for the coupon material model and the NCAC material differed by less than 1%; the static deflections were different by only 3%.

Table 36: Comparison of Pendulum Deflections

		Coupon Material	Hybrid Material	NCAC Material
Max Deflection				
	Magnitude (in)	23.07	23.77	22.99
	X (in)	0.04	0.05	0.01
	Y (in)	22.54	23.25	22.43
	Z (in)	4.95	4.95	5.07
	Time (s)	0.120	0.130	0.120
Static Deflection				
	Magnitude (in)	20.55	20.39	19.94
	X (in)	.04	0.02	0.04
	Y (in)	20.05	19.56	19.40
	Z (in)	4.52	5.76	4.60

Discussion

Despite the seemingly large differences between the various material models, the measured maximum deflections did not vary much. The largest differences observed were a 3% difference between the dynamic deflection of the hybrid material and other materials. There was also maximum 3% difference between the static deflection of the coupon and NCAC materials. The similarity between each of the deflection curves is readily apparent in Figure 115.

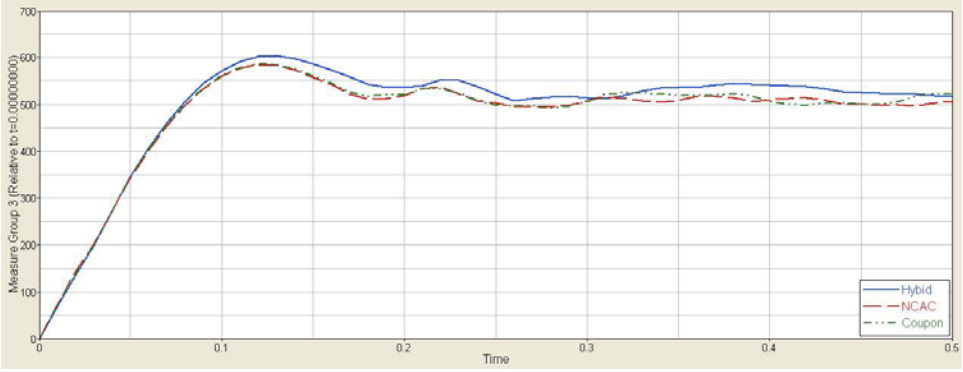

Figure 115: Selected node deflections for each material model

Preliminary models of the full-scale w-beam strong-post guardrail with the original NCAC material model for the guardrail steel have resulted in system deflections lower than those reported in real crash tests. However, we could find no references to the source of the material parameters. Although the hybridized material yielded the highest deflection of all the models, there is again no existing literature or experimental data supporting this material. The coupon material published by Wright resulted in a deflection only 3% lower than the hybridized material and is backed by experimental data. Thus, the material of choice for future simulations would be the NCAC material.

References

1. Wright, Amy and Ray, Malcolm H. *Characterizing Roadside Hardware Materials for LS-DYNA3D Simulations*, Report FHWA-RD-96-108, US Department of Transportation, Washington, DC, 1997.
2. Reid, John and Sicking, Dean, *Design and Simulation of a Sequential Kinking Guardrail Terminal*, International Journal of Impact Engineering, Volume 21(9), pp. 761-772, 1998.
3. Wang, Q., Gabauer, D., Hampton, C., Gabler, H. C. *Validation of a Strong-Post W-Beam Finite Element Model with Minor Damage through Pendulum Testing*, Submitted to TRB August 1, 2008.

APPENDIX B: MATERIAL PROPERTIES OF POST STEEL

Introduction

The assembly of typical w-beam guardrails requires the use of wood or steel strong posts to provide lateral stiffness to the barrier. Along most highways, steel posts are widely used. The behavior of the posts is of great importance to the performance of the overall system due to the risks of vehicle tires getting caught on the posts. However, in a full system it can be difficult to isolate the contributions of the post from those of the rails and soil.

The cost of running full scale tests and multiple tests of subcomponents is typically quite large. Thus, it is often preferred to perform only a small number of tests and then use finite element simulations to predict the response under variation of key properties. In a finite element model, the most important property is the material definition, which defines how the part carries a load.

As part of the preparation for a full-scale model of a strong-post w-beam guardrail, a small finite element model of a steel post embedded in soil was developed. The strength of the post material can greatly influence its behavior and can be the difference between post yield or post rotation. Because there are several material definitions available for post steel, the goal is to use finite element simulation to determine which of the materials results in the most realistic post behavior.

Methods

To reduce the computational time needed, as well as eliminate confounding factors, the full finite element model of the NCAC steel strong-post w-beam guardrail system was reduced to

a single post embedded in a soil bucket. This eliminated any influences from the rails, bolts, and blockouts. The post used was the designation PWE01, meaning the total post height was 1830 mm and the embedment depth was 1100 mm. The beam type is W150x13.5. Further details on the post dimensions can be found in Appendix A.

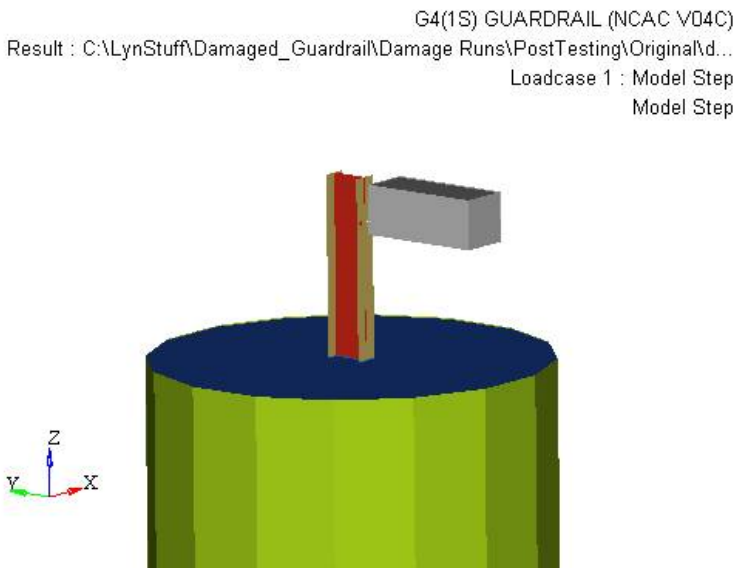

Figure 116: Finite element model of post embedded in soil and striking mass

To determine which of the material definitions represents the best match for the full-scale performance, the simulation would be run three times. Each time, a different material definition was used for the post while all other aspects of the model remained the same. The three different material models are shown below in Table 37. The largest differences between the three material definitions were the stress-strain curves. The WPI coupon tested material was the weakest while the NCAC material was the strongest.

Table 37: Post material definitions

	NCAC Post Material		**WPI Coupon Test Post Material**		**TTI Post Material**	
Material Type	MAT24		MAT24		MAT24	
Density (Mg/mm^3)	$7.89E^{-9}$		$7.86E^{-9}$		$7.86E^{-9}$	
Modulus (MPa)	200,000		200,000		200,000	
Poisson's Ratio	0.30		0.33		.290	
Yield Stress (MPa)	298		315		336	
Failure Strain	$1.10E^{8}$		0.625		No	
Strain Hardening	Yes (C=90, P=4.5)		No		No	
	Strain	**Stress**	**Strain**	**Stress**	**Strain**	**Stress**
Stress-Strain Pt. 1	0.00	298	0.00	315.0	0.00	336
Stress-Strain Pt. 2	0.02	340	0.019	315.0	0.024	336.7
Stress-Strain Pt. 3	0.04	370	0.05	427.0	0.042	401.2
Stress-Strain Pt. 4	0.08	415	0.165	500.8	0.050	434.3
Stress-Strain Pt. 5	0.16	480	0.33	504.3	0.141	537.2
Stress-Strain Pt. 6	0.32	575	0.495	506.5	0.213	589.6
Stress-Strain Pt. 7	0.64	810	0.625	400.0	0.250	675.0
Stress-Strain Pt. 8			1.00	0	0.259	677.0

Figure 117 shows the stress-plastic strain curves detailed in Table 37 in a visual form. The material definitions were very divergent after 0.2 plastic strain. Whether this could cause problems was dependent on the maximum strain experienced by the post during impact. The WPI coupon test material was the only material to define a failure strain; the other materials would extrapolate a new stress value as the plastic strain exceeded the specified data points.

In Figure 118, a zoomed in view of the stress-strain curve shown in Figure 117 is available. The most interesting feature of the zoomed in curve is that the WPI material is actually stronger than the NCAC material and nearly as strong as the TTI material in this narrow range of plastic strains. Therefore, the post material model that incorporates the largest amount of deflection may vary based on the expected range of plastic strain occurring in the finite element model.

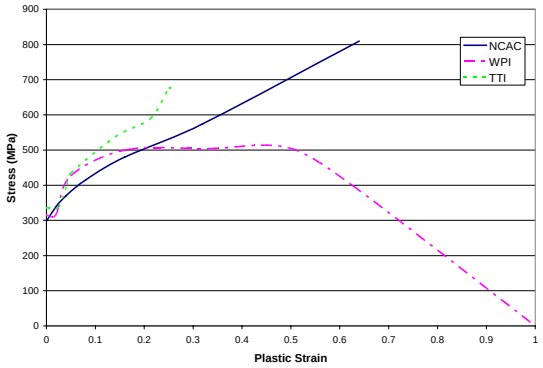

Figure 117: Stress-plastic strain curves for each of the three material definitions.

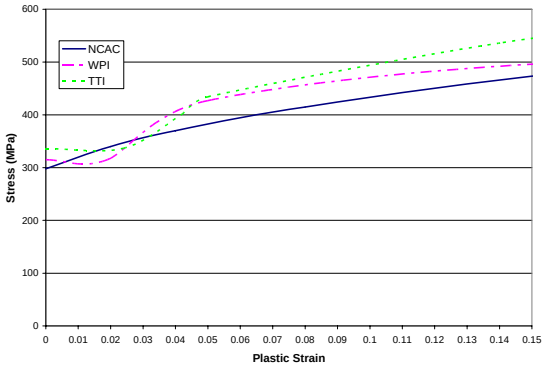

Figure 118: View of stress-strain curves at low plastic strain values (≤ 0.15).

Deflection of the post at various heights was measured by taking the displacement of selected nodes making up the posts. The magnitude and global axis components of the displacement were measured to provide a more accurate glimpse of the post behavior, as posts rarely deflect on one axis even when struck directly on the front face. All of the deflections were measured using a node on the center of the front flange.

Results

Due to the small size of the finite element model, each simulation required only 15 minutes of wall time to complete. The results of each of the models are shown in Figure 119 - Figure 121. Each figure also includes a plot of the deflection of the post at the ground level and at the top of the post (Note that the Y-axis scales are different between the figures).

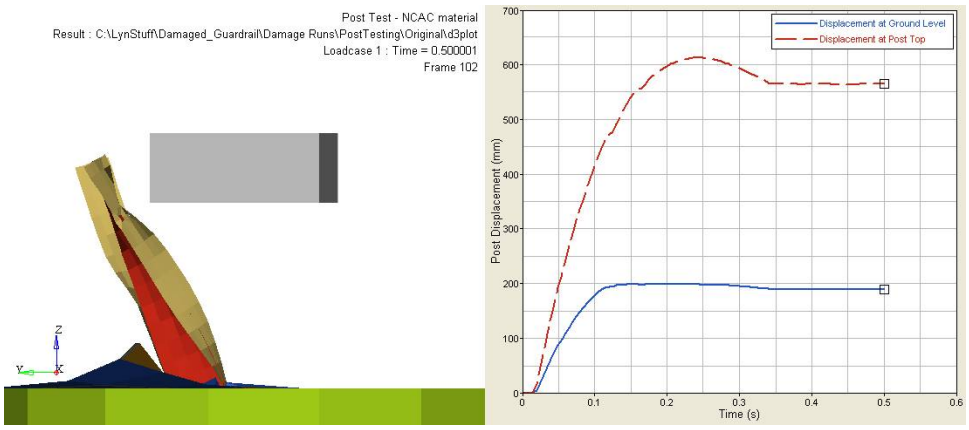

Figure 119: Post Response using the NCAC material definition

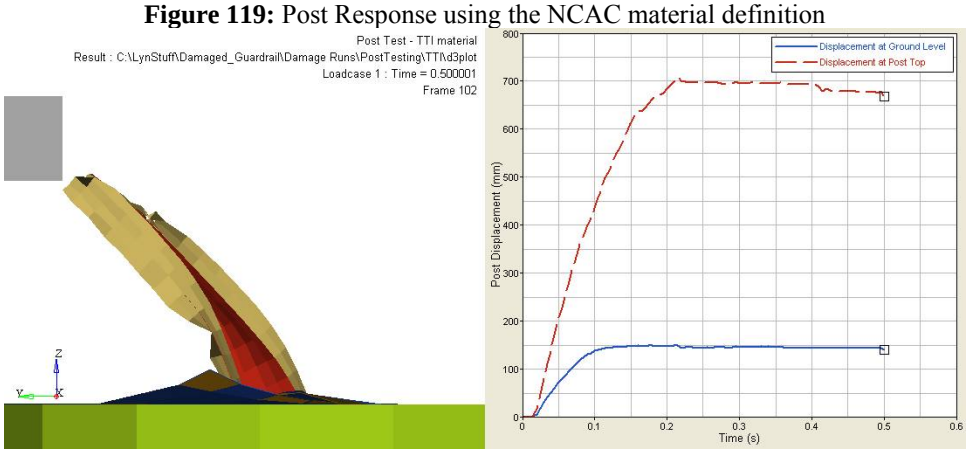

Figure 120: Post Response using the TTI material definition

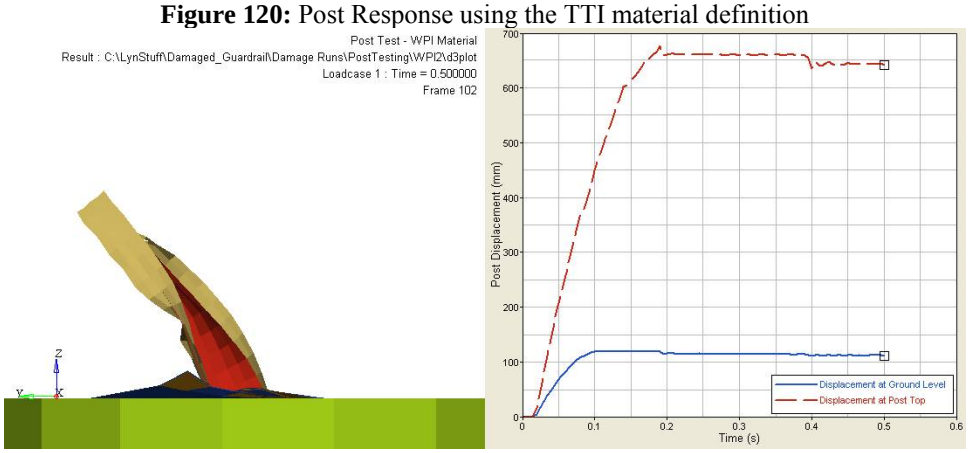

Figure 121: Post Response using the WPI material definition

Plots of the deflection of the post at various levels are shown in Figure 122 - Figure 125. As would be expected from the above figures, the largest deflection occurred in the model using the TTI material definition, while the NCAC model showed the lowest. The NCAC model also showed the greatest amount of elastic deflection recovery.

All of the finite element models showed twisting of the posts during impact. Although all of the posts rotated roughly the same amount (~90 degrees), the direction of rotation varied. The NCAC post rotated in the clockwise direction while both the TTI and WPI post rotated counterclockwise.

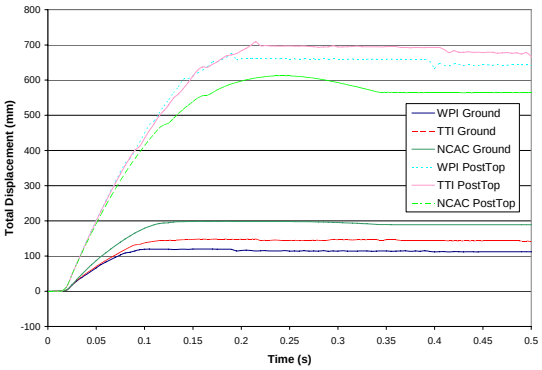

Figure 122: Total displacement of post

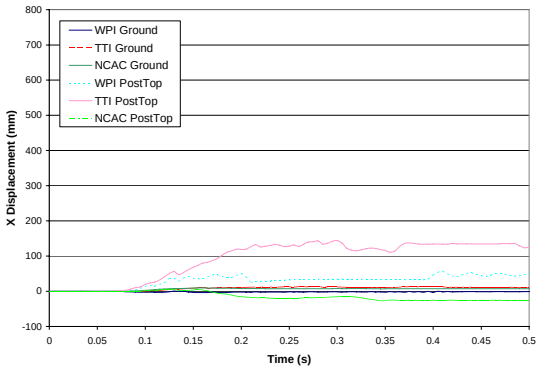

Figure 123: X-axis displacement of post

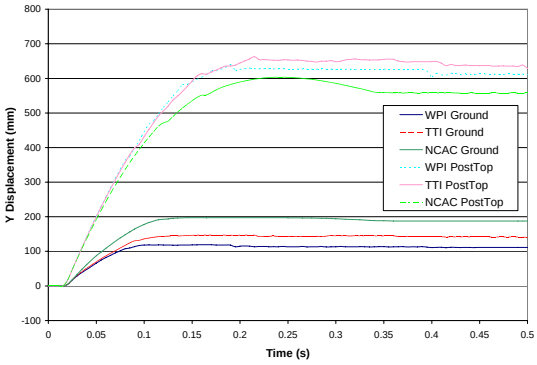

Figure 124: Y-axis displacement of post

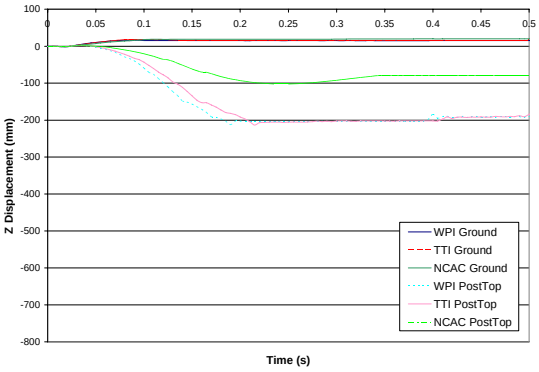

Figure 125: Z-axis displacement of post

In Figure 126, the movement of the base of the post, which was embedded in the soil is shown. Surprisingly, the results were the complete opposite of what was observed at the top of the post. The NCAC material model showed the largest displacement at the bottom of the post. The cause of this odd disagreement was pinned down to the yielding the post.

Referring back to Figure 119 - Figure 121, there is a marked difference in the straightness of the posts. When the post used the NCAC material definition, the deflected post was still relatively straight, implying that the energy from the impact was readily transferred to the soil

and motion of the post bottom. However, the posts modeled with the TTI and WPI materials yielded, resulting in noticeable bends in each post above the ground level. The post yield resulted in large deflection at the post top, which in turn minimized the deflection below ground.

Another point of interest was why the post using the NCAC material model was the only post that did not yield. Referring back to Table 37, there are not any properties for the NCAC material that are significantly larger or smaller than other two materials. Thus, the difference in performance was most likely due to the strain hardening parameters defined for the post steel. When the NCAC post was run again without the strain hardening effects, the post yielded in the same manner as the other posts (not shown).

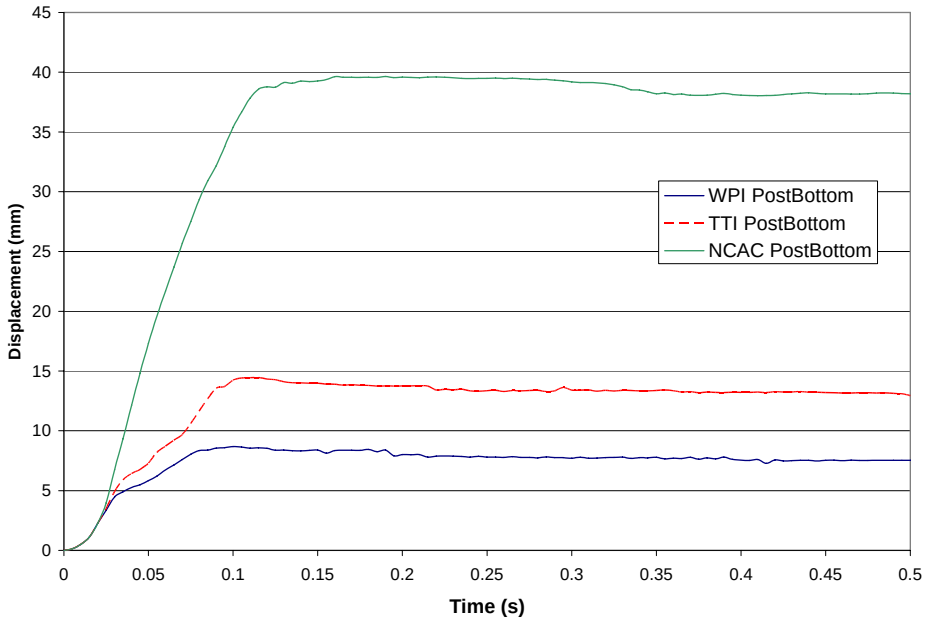

Figure 126: Total displacement of bottom corner of post

Discussion

The results observed after running each of the three post materials in finite element model were rather unexpected. The greatest influence on the post deflection turned out to be the ability of the post to resist yielding under impact. Posts that yielded had very large deflections at the

top of the post, with minimal deflection at and below the ground level. On the other hand, the post that did not yield showed less deflection at the post top, but the deflection at the ground and below was larger. All of the materials defined stress-strain values to at least 0.25. However, the strains observed in the finite element models were well under this amount. Even for the yielding posts, strains rarely exceeded 0.10.

The ability of a post to avoid yielding is important for the performance of the overall system. Posts that yielded were unable to contain all of the energy from the striking mass. Posts that yield easily also have the potential to exert a downward force on the supported rail sections, increasing the change of a catastrophic override. Additionally, it was noted in the finite element simulations that the yielding posts also showed the lowest amount of deflection at the ground line. The lack of ground level motion, combined with the excessive deflection at the post top, represents a situation in which interactions between the vehicle tire and post are likely.

The NCAC post material was the only material to include strain hardening values, and was also the only material that did not result in post yield. Additional modeling showed that it was this strain hardening behavior, and not the stress-strain curve, that prevented yield from occurring. The NCAC material also showed the largest spring-back effect, with roughly 50 mm of deflection being recovered after the impact. The NCAC material also showed only 5 mm of lateral deflection.

Both the TTI and WPI materials resulted in post yield, and the final deflection values were surprisingly similar. The difference between these two materials was initially expected to be far larger, as Figure 117 showed that the stress-strain curves were divergent for higher strains. However, the strain experienced by the post never entered this range, and at the lower strains the curves were quite similar. The larger overall deflection of the TTI material in the figures was

mostly due to the 144 mm lateral deflection, which was almost three times as large as the 56 mm lateral deflection of the WPI material.

Conclusions

A series of finite element models were used to determine the performance of three different post materials. These materials originated from the NCAC strong-post guardrail model, the TTI strong-post guardrail model with mow strip, and coupon experiments performed by WPI on post steel. Each model was closely examined to quantify the deflection at the top, bottom, and ground level, as well as whether the post yielded.

Based on the results, it currently appears that the NCAC material model would be the best suited for a full-scale guardrail model. This was due to this material being the only definition that did not result in post yield. Additionally, this post material showed the largest amount of ground level deflection, which is often observed in real impacts where the soil is not as tightly controlled.

References

1. A. E. Wright and M. H. Ray, *Characterizing Roadside Hardware Materials for LS-DYNA3D Simulations*, FHWA-RD-96-108, February 1997.
2. NCAC Finite Element Model Archive, *W-Beam Guardrail*, Posted Jan 20 2007. Accessed Sept 10 2008. http://www.ncac.gwu.edu/vml/models.html
3. Texas Transportation Institute, *Guardrail System in Mow-Strip*, Posted Jan 20 2007, Accessed Sept 10 2008. http://www.ncac.gwu.edu/vml/models.html

APPENDIX C: MATERIAL PROPERTIES OF SOIL

Introduction

As part of the NCHRP 22-23 project, a number of finite element models have been developed to simulate the impact of a 2000 kg pickup truck into a strong-post w-beam guardrail. In order to save time on model development, the strong-post guardrail model available from the NCAC finite element library [1] was used. The NCAC guardrail model uses 1.6m diameter soil "buckets" to model the soil around each post. Questions about the modeling of the soil were raised. In particular, there were concerns that the relatively small diameter of the soil buckets was not sufficient to allow the posts to move as they would in a real test. There was also a concern over whether the motion of a post would exert some effect on the adjacent posts.

At the same time, a new finite element model of the Chevrolet C2500 pickup truck was released to the finite element library. This new vehicle model was far more detailed than the reduced C2500 model that was currently being used in the project. In addition, the response of the new detailed vehicle suspension system was validated against test data.

Objective

1. Compare the performance of the guardrail when using the soil buckets to the performance when using the much larger soil trough.
2. To decide whether the reduced vehicle model was sufficiently detailed to accurately capture vehicle response.

Methodology

Modeling a vehicle crash into a guardrail requires two basic subcomponents: the vehicle model and the guardrail model. However, for each of these subcomponents, two different models were available. Thus, it was necessary to run a series of simulations to determine which of the vehicle and guardrail models should be used to run future simulations.

Vehicle Model

There are two vehicle finite element models under consideration for this research. Both of these models are representations of the Chevrolet C2500 pickup truck available from the NCAC finite element library [1]. The first model, the NCAC reduced Chevrolet C2500, was the most simple and least demanding of pickup truck models available. The second model was the NCAC detailed model of a 1994 Chevrolet C2500 pickup truck. This model was designed to be more accurate and detailed than the reduced model, but the computational requirements are much higher. The exact increase in computational time required was determined in the course of this study.

The NCAC reduced Chevrolet C2500, shown in Figure 127, was created as a fast-running model. The coarse mesh used to model the body panels decreased the computational requirements to simulate the vehicle at the expense of accuracy. Some interior components such as the seats, fuel tank, and batteries were completely omitted. This reduced detail model also possessed a simplified suspension system in which many of the interior components were modeled as rigid bodies to further reduce the computational requirements. Because of this minimal approach, the abilities of the reduced model to accurately represent suspension response and extensive deformation have been called into question.

The alternative vehicle model available was the NCAC detailed 1994 Chevrolet C2500 pickup truck, shown in Figure 128. This detailed model was designed to maximize accuracy at the cost of greatly increased computational requirements. The detailed mesh more accurately represented the finer geometric details of the vehicle body, and the vehicle parts that were omitted in the reduced version are present in the detailed version. Also, the suspension was more detailed and was validated against real world test data [2].

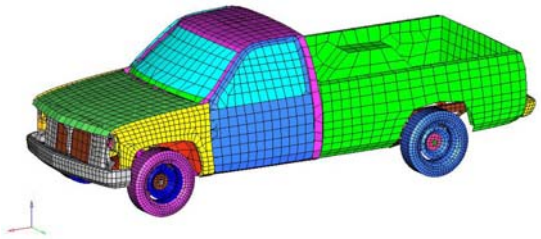

Figure 127: NCAC reduced Chevrolet C2500 Pickup v9

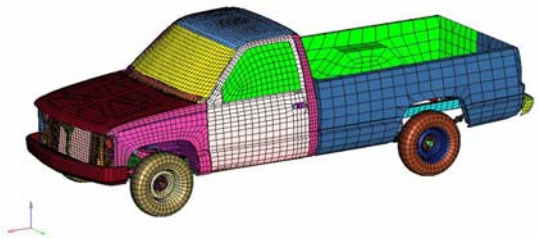

Figure 128: NCAC detailed 1994 Chevrolet C2500 Pickup v0.7

Guardrail Model

Strong-post W-beam guardrail is a relatively complex structure that provides stiffness by distributing impact loads across both the rails and posts. NCAC provides a publicly available model of strong-post w-beam, available from the NCAC finite element library [1]. This model includes explicitly modeled splice bolts, post bolts, and soil, and was validated against a test performed at the Texas Transportation Institute (TTI) [3]. The test used to validate the models was believed to be TTI 405421-1. The unmodified guardrail model is shown in Figure 129 and Figure 131.

In the NCAC technical report [3], the size of the soil buckets, each of which held one post in position, was set to 2.7 meters diameter. However, the version of the guardrail model available from the finite element library contains soil buckets that are roughly 1.6 meters in diameter. This raised the question about whether the smaller volume of soil modeled was

causing an artificial restriction on the motion of the posts. To test this idea, a modified version of the guardrail was developed. The soil in the area of impact was remeshed as a single block of soil that was 2.7 meters in width and 7.7 meters long. This trough of soil contained four posts. The guardrail with new soil is shown in Figure 130 and Figure 132. In addition to providing more room in which posts can move, this approach also allows the soil stresses from adjacent posts to influence each other.

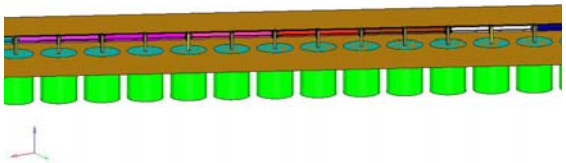

Figure 129: NCAC strong-post W-beam guardrail

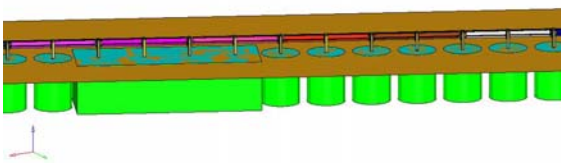

Figure 130: NCAC strong-post W-beam guardrail with soil modified to be a continuous trough

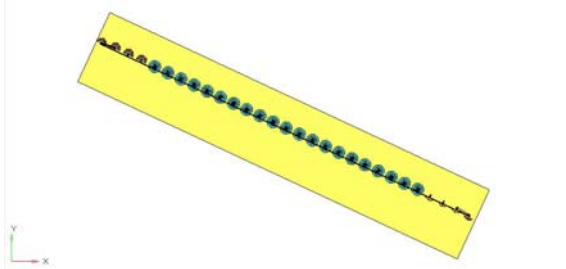

Figure 131: NCAC strong-post W-Beam guardrail, overhead view

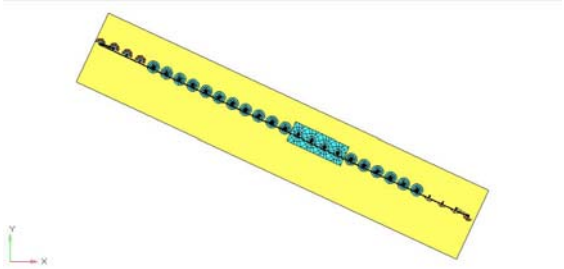

Figure 132: NCAC strong-post W-Beam guardrail with modified soil, overhead view

Simulation Settings

Because there were two models available for both the vehicle and the guardrail, a total of four simulations were needed to cover all the possible combinations. The list of simulations to be run is shown in Table 38. All simulations were set up to run to 1000 ms of simulated time with all data being output at the same frequency. The initial speed of the vehicle was 100 kph (60 mph) at 25 degrees, which corresponds to the NCHRP 350 test conditions for pickup trucks. Contact definitions were identical between the two simulations using the reduced vehicle. Similarly, the contacts were identical for the two simulations using the detailed vehicle.

Table 38: Planned simulations

	Vehicle Model	Guardrail Model
Simulation 1	Reduced C2500	Original Soil Buckets
Simulation 2	Detailed C2500	Original Soil Buckets
Simulation 3	Reduced C2500	Soil Trough
Simulation 4	Detailed C2500	Soil Trough

Contact Definitions

The interfaces defined between the vehicle and guardrail in each simulation varied slightly due to the differences between the two vehicle models. The interfaces used to define the contacts between the vehicle and guardrail are shown below in Table 39 and Table 40. The reduced C2500 model had one additional interface that prevented the front left tire from moving through the body panels nearby.

Table 39: Interfaces defining contact between reduced C2500 and guardrail

ID	Contact Type	Soft	Master	Slave
1	Auto Surface to Surface	2	Vehicle Body (excluding front left tire)	Guardrail
2	Nodes to surface	0	Guardrail	Vehicle Body (excluding front left tire)
3	Auto Surface to Surface	2	Front left tire	Guardrail
4	Nodes to surface	0	Guardrail	Front left tire
5	Auto Surface to Surface	1	Guardrail	Front left tire
6	Auto Surface to Surface	2	Front left wheel well	Front left tire

There were also two other changes made in interfaces that were shared between both vehicle models. Contact 1, defined between the vehicle body and the guardrail, was different for the reduced C2500, where the thickness of the master components was overridden and set to be 2.0 mm. The other change was due to the difference in tire thickness between the two vehicle models. The tire thickness of the reduced C2500 was 5 mm, while the thickness of the detailed C2500 tires was only 3 mm. To make the thicknesses the same, the master components

thickness for the detailed C2500 contact three was set to 5 mm, making the tire the same thickness as in the reduced C2500.

Table 40: Interfaces defining contact between detailed C2500 and guardrail

ID	Contact Type	Soft	Master	Slave
1	Auto Surface to Surface	2	Vehicle Body (excluding front left tire)	Guardrail
2	Nodes to surface	0	Guardrail	Vehicle Body (excluding front left tire)
3	Auto Surface to Surface	2	Front left tire	Guardrail
4	Nodes to surface	0	Guardrail	Front left tire
5	Auto Surface to Surface	1	Guardrail	Front left tire

The soft parameter mentioned in the two tables refers to the method by which LS-DYNA applies contact forces. A value of zero was the default value for the soft option, which means that the contact forces are generated via the penalty method. Soft = 1 changes the way in which the contact forces were generated to the constraint method. This method offers more stability when the contact was between a soft object (like a tire) and a stiff object (like steel). Soft = 2 was a variation on the default contact method that was better suited to situations where penetration of components was likely.

Validation

All of the simulations planned are models of a vehicle hitting an undamaged guardrail at NCHRP 350 conditions. Therefore, there was a large selection of crash tests that could be used to validate the finite element model results. The TTI test 405421-1 [4] was selected, both because it was a successful test and because this was the test used in the NCAC technical report.

Results

All of the simulations were successfully run and the results tabulated. Table 41 below shows the amount of real runtime needed to run each of the simulations. However, each simulation ran for a different amount of simulated time. All of the simulations ended early because of instabilities caused by damage to the front left tire. The full runtimes needed to simulate 1 second were calculated by extrapolating the runtime needed to complete most of the simulation.

Table 41: Runtime needed to complete simulations

	Vehicle Type	Soil Type	Runtime	Time Simulated	Full Runtime
Simulation 1	Reduced	Original	15 hr 12 min	0.754 sec	20 hr 10 min
Simulation 2	Detailed	Original	25 hr 0 min	0.980 sec	25 hr 31 min
Simulation 3	Reduced	Soil Trough	20 hr 21 min	0.995 sec	20 hr 27 min
Simulation 4	Detailed	Soil Trough	23 hr 14 min	0.881 sec	26 hr 22 min

Even with the runtime for one of the simulations missing, it was evident that the use of the detailed finite element vehicle model of the C2500 required roughly five hours more of runtime. The remeshing of the soil, which increased the total number of elements by only 24, resulted in a 50 minute increase in runtime. This was most likely due to the increased volume of soil modeled rather than a change in the number of elements.

In Table 42, the raw numerical values for all of the NCHRP 350 test criteria are presented, along with additional data such as vehicle rotations and damage lengths. Table 43 was intended to compliment Table 42 by providing the percent difference between each of the simulation results and the TTI crash test.

The results observed from the four simulations did not clearly identify one particular model that was superior to the others. Rather, each model seemed to have some test criteria at it performed better while also having other criteria that performed worse.

The detailed C2500 vehicle model offered improved performance with respect to exit speed, occupant longitudinal impact velocity, 50 ms average longitudinal acceleration, and maximum vehicle pitch. However, the reduced vehicle predicted ridedown accelerations, 50 ms average lateral acceleration, maximum vehicle roll, and guardrail deflection better.

Table 42: NCHRP 350 Test Results

		TTI 405421-1	Reduced / Original Soil	Detailed / Original Soil	Reduced / Soil Trough	Detailed / Soil Trough
Impact Conditions						
	Speed (kph)	101.5	100	100	100	100
	Angle (deg)	25.5	25	25	25	25
Exit Conditions						
	Speed (kph)	55	49	53	52	53
	Angle (deg)	16	17.53	14.52	20.23	11.33
Occupant						
	Impact X (m/s)	7.1	8.69	7.51	8.18	7.42
	Impact Y (m/s)	4.4	5.39	5.54	5.40	5.60
	Ridedown X (G)	-7.9	-10.08	-11.77	-8.04	-11.53
	Ridedown Y (G)	8.4	-10.20	-12.27	-11.53	-13.20
	50 ms Avg X (G)	-5.3	-7.65	-6.68	-7.69	-6.95
	50 ms Avg Y (G)	4.3	-6.04	-6.82	-5.88	-7.00
	50 ms Avg Z (G)	-4.8	3.18	-3.85	-2.49	-3.76
Guardrail Deflection						
	Dynamic (m)	1.0	0.76	0.69	0.77	0.71
	Static (m)	0.7	0.57	0.55	0.60	0.58
Damage Length						
	Length (m)	5.8	6.15	7.6	6.33	7.23
Vehicle Rotation						
	Max Roll (deg)	-10	-7.1	-14.4	-9.0	-14.6
	Max Pitch (deg)	-4	-10.8	-9.9	-16.2	-7.6
	Max Yaw (deg)	42	44.4	40.3	45.4	37.2

The design of the soil bucket had less of an effect than expected. The only fields that were influenced by the soil design were the maximum dynamic and static deflections. Using the larger, continuous soil resulted in a small (10-20 mm) increase in dynamic deflection. This was far less significant that the variation induced by the vehicle model, which was surprising. The effect on the static deflection was a bit stronger (~ 30 mm increase).

Table 43: Percent Deviations of FE Models from TTI Test 405421-1

	Reduced / Original Soil	Detailed / Original Soil	Reduced / Soil Trough	Detailed / Soil Trough
Impact Conditions				
Speed (kph)	-1.5%	-1.5%	-1.5%	-1.5%
Angle (deg)	-2.0%	-2.0%	-2.0%	-2.0%
Exit Conditions				
Speed (kph)	-10.9%	-3.6%	-5.5%	-4.2%
Angle (deg)	9.6%	-9.2%	26.4%	-29.2%
Occupant				
Impact X (m/s)	22.3%	5.8%	15.3%	4.5%
Impact Y (m/s)	22.6%	25.9%	22.8%	27.2%
Ridedown X (G)	27.5%	49.0%	1.8%	46.0%
Ridedown Y (G)	21.4%	46.1%	37.3%	57.1%
50 ms Avg X (G)	44.4%	26.1%	45.0%	31.1%
50 ms Avg Y (G)	40.4%	58.7%	36.8%	62.8%
50 ms Avg Z (G)	-33.8%	-19.8%	-48.1%	-21.8%
Guardrail Deflection				
Dynamic (m)	-24.1%	-31.1%	-23.0%	-29.4%
Static (m)	-18.7%	-21.1%	-13.7%	-17.8%
Damage Length				
Length (m)	6.0%	31.0%	9.1%	24.7%
Vehicle Rotation				
Max Roll (deg)	-29.0%	44.0%	-10.0%	46.0%
Max Pitch (deg)	170.0%	147.5%	305.0%	90.0%
Max Yaw (deg)	5.71%	-4.1%	8.1%	-11.4%

For all of the simulations, the guardrail deformation was lower than expected and the vehicle accelerations and occupant impact velocities were higher than expected. This was indicative of a guardrail system that was stiffer than would be observed in the real crash test. There were no consistent patterns observed in the exit angle, Z-axis acceleration, or the vehicle yaw.

Recommendations

Based on the results of these four simulations, our recommendation is to use the soil buckets provided in the original NCAC guardrail model. The use of the extended soil trough did

not significantly improve any of the NCHRP 350 test values. Future simulations will most likely be run with the detailed C2500 vehicle model. Although using the detailed vehicle increased the required time for a simulation by five hours, the accuracy in some of the key NCHRP 350 values (Exit speed, impact X, 50 ms average X) were improved.

References

1. NCAC, *Finite Element Archive*, Accessed November 19, 2008. http://www.ncac.gwu.edu/vml/models.html
2. D. Marzougui, M. Zink, A. Zaouk, C. D. Khan, N. E. Bedewi, *Development and Validation of a Vehicle Suspension Finite Element Model for Use in Crash Simulations*, International Journal of Crashworthiness, Vol. 9(6), pp. 565-576, 2004.
3. *Development of a Finite Element Model for W-Beam Guardrails*, NCAC Technical Summary NCAC 2007-T-004, November 2007.
4. D. Bullard, W. Menges, and D. Alberson, *NCHRP Report 350 Compliance Test 3-11 of the Modified G4(1S) Guardrail with Timber Blockouts*, Texas Transportation Institute, 1996.

APPENDIX D: DEVELOPMENT OF RAIL FLATTENING METRIC

Introduction

Everyday, there are traffic accidents occurring across the entire United States, and a fraction of these accidents involve damage to the various types of guardrail systems. Although there are many types of barriers employed, the most common is the w-beam guardrail, an example of which is shown below in Figure 133. When any guardrail is hit, the damage to the rail can usually be classified in many ways, including deformation and flattening. It seems intuitive that a guardrail presenting damage that impairs its own functionality should be replaced, but there are currently no quantitative measures to qualify when a guardrail has lost enough of its integrity to pose a risk.

Figure 133: An example of w-beam guardrail that has been flattened by an impact from a large van.

The objective of this study is to find a quick, simple method to quantify the flattening of a w-beam rail. W-beam guardrail is capable of flattening and deforming to absorb crash energy as it redirects the striking vehicle away from any roadside hazards. However, there is no established process for measuring the degree to which a guardrail has been flattened. A novel method of relating the flattening of the rail to the change in the height of the guardrail is

developed in this paper. This new method will be both descriptive of the damage done by flattening and readily accessible to personnel working in the field.

The geometry of a w-beam rail is well-defined, with numerous documents available detailing the dimensions and angles that characterize each part of the whole system. The rail, which is the part of interest in this study, is characterized by its unique W-like shape as shown in Figure 134. A more detailed drawing of a w-beam rail cross-section is available at the end of this appendix in Figure 139. The w-beam rail is 2.67 mm in thickness and is made of galvanized steel. The rails are overlapped end-to-end to form the roadside barriers that can be observed on the sides on most highways.

When examining samples of real-world damaged guardrail, it was noted that most sections of rail showing signs of flattening also showed signs of have an increase in height. This is expected for material that is compressed in one direction while being allowed to move freely in others. Using this information, it is hypothesized that there is an equation that can link a quantifiable change in the height of a rail to the change in the depth of the rail, i.e. flattening. This paper discusses the development and evaluation of this method.

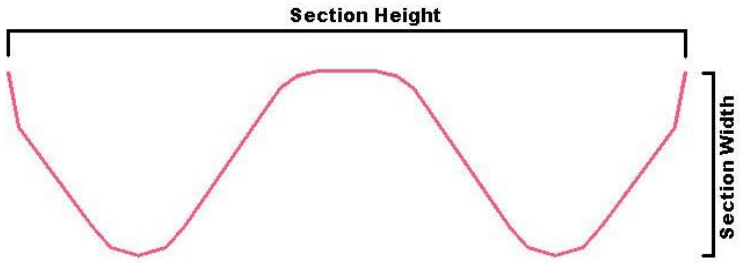

Figure 134: A cross-section of an undeformed w-beam guardrail. In application, the rail would be mounted on posts so that the section height is vertical rather than horizontal.

Methods

Full scale testing of w-beam rail sections can be expensive, in terms of both time and funding. In lieu of this, it was elected to use the finite element code LS-DYNA to determine the

response of the guardrail to a flattening load. This form of testing offers a highly controllable and repeatable method of deform the rails and measuring the deformed geometry of the rail.

Figure 135 shows the model that was used to conduct this study. A small section of guardrail was modeled using thin shell elements, all of which were constrained from moving in the lateral direction to represent the presence of the full length of the rail. The flat panels above and below the rail are modeled as rigid surfaces, limiting the deformation to the rail only. The rail itself is made of deformable thin shells with a uniform thickness of 2.67 mm. It is five elements wide and 30 elements tall, leading to a total of 150 elements making up the small section of guardrail. The size of each element varies, with the largest appearing in sections of the rail that are relatively flat.

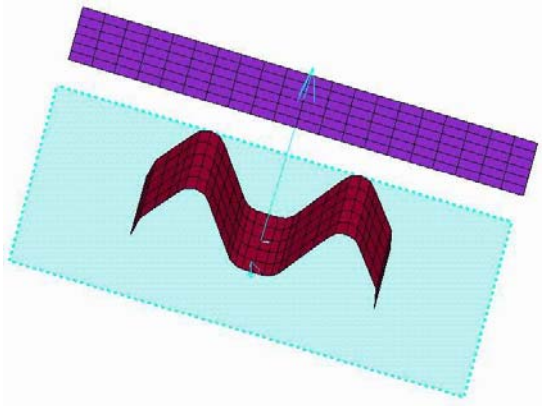

Figure 135: The undeformed mesh of a section of guardrail. The section of rail rests on a rigid surface (light blue) and is deformed by the rigid mesh (purple).

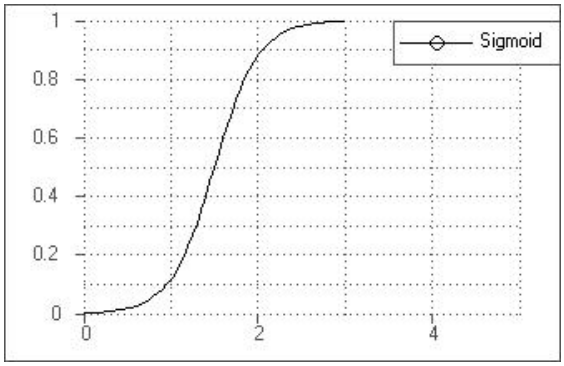

Figure 136: The loading curve used to specify the motion of the meshed rigid plane. The independent variable is time in seconds and the y-axis represents the fraction of the full load that is applied.

Loading of the w-beam segment was accomplished using a sigmoid curve, such as the one shown in Figure 136. The shape of the sigmoid curve is well-suited to starting and stopping the loading process without inducing abrupt vibrations and instabilities. This curve controlled the displacement of the meshed rigid panel shown in Figure 135. The duration of the motion was the same in all tests, while the magnitude of the displacement was adjusted.

As the rigid panel moves, it contacts and deforms the rail section. At the end of the simulation, the rail can be examined to determine how its dimensions have changed. For this study, the change in section depth was measured and correlated to the increase in height of the guardrail. The change in section depth was measured by taking the maximum distance between the back and front of the rail after deformation. The new section height was measured by the maximum distance between the top and bottom edges of the rail.

Results

There were a total of 12 different displacement conditions applied to the finite element representation of the guardrail. It is important to note that there is a spacing of 13.7 mm between the undeformed guardrail and the moving plate, such that a displacement of 20 cm will not represent a loss of section depth of 20 cm. The results for all of the test conditions are summarized below in Table 44. This table contains the post-deformation measurements of the height and depth as well as the percent increase in height and percent decrease in depth. Note that the theoretical maximum for flattening of the rail without any stretching results in an increase of 56.1% in rail height.

Figure 137 shows a graphical representation of the numerical data. The data follows a rather linear trend up until it reaches a 25% increase in the section height. After this point, the data no longer behaves linearly but instead closely follows an exponential pattern. An attempt to fit a single exponential curve to the full data set yielded a curve with an R^2 value of 0.985.

Table 44: The results for each of the controlled displacement conditions

Displacement (mm)	Section Height (mm)	Section Depth (mm)	% Inc Height	% Dec Depth
0	321.7	87.9	0.0%	0.0%
20	346.9	81.8	7.8%	7.0%
25	366.6	76.8	14.0%	12.6%
30	386.8	71.8	20.2%	18.3%
35	405.7	66.8	26.1%	24.0%
40	418.9	61.8	30.2%	29.7%
45	432.3	56.9	34.4%	35.3%
50	442.4	51.8	37.5%	41.0%
60	461.9	41.7	43.6%	52.5%
70	477.2	31.3	48.3%	63.8%
80	483.6	22.1	50.3%	74.8%
90	491.2	12.2	52.7%	86.1%

However a much better fit was obtained by allowing the data to be split into two distinct sets. By fitting a linear curve to all data below 30 mm displacement and an exponential curve to all data above 30 mm, a superior curve fit was obtained. The R^2 value for the linear portion was > 0.999 while the exponential curve has a R^2 value of > 0.99. At the datum point for 35 mm displacement, the difference between the two curves is less than 0.3%.

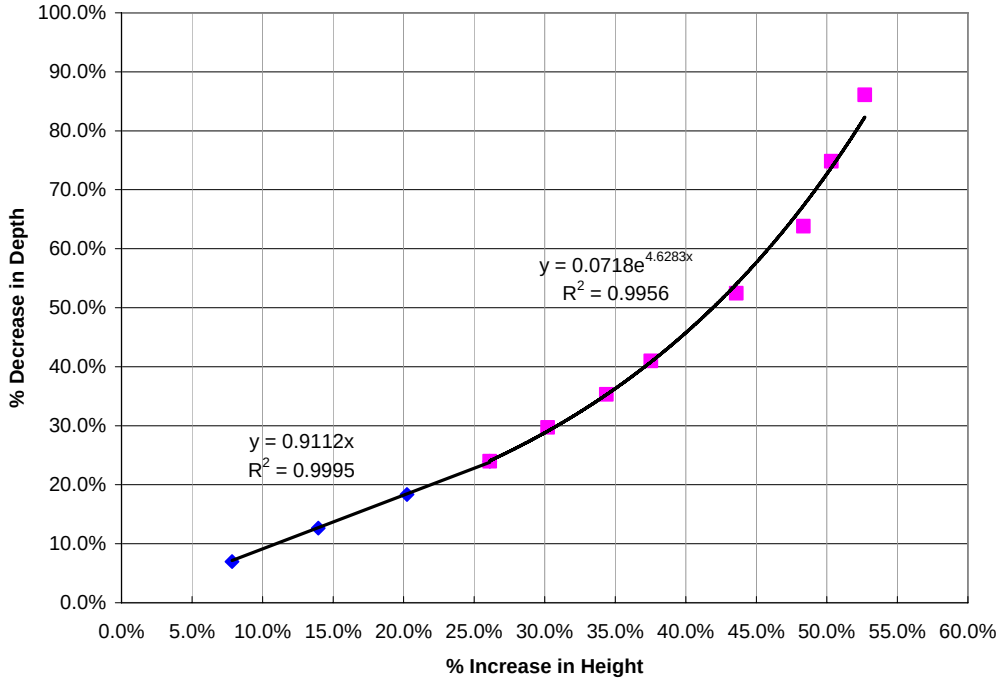

Figure 137: The % decrease in section depth as a function of the increase in the section height. Curve fits with the correlation factors also shown.

The curves fit to the data in the finite element tests was used to create a relatively simple formula using the increase in rail height to approximate the loss in section depth of the rail. Although splitting the data points into two curve fits represents an increase in the complexity of computation, the increases in accuracy should be worthwhile. The final proposed equations are shown below in Table 45.

Table 45: Proposed correlation between the deformed rail height and depth

If the rail height is …	Use this formula for % flattening …
Below 400 mm	$0.9112 \cdot X$
At or above 400 mm	$0.0718 \cdot e^{4.6283 \cdot X}$

Discussion

The correlation between the rail height and depth is of interest primarily because of the difficulty of measuring the depth in the field. The rail height is a far easier measurement to make and requires only a short tape measure or long ruler to make. In the field, the deformation of the

guardrail will generally result in a far more complicated profile than those of the controlled conditions used in this test. One of the greatest benefits of this approach is that it easily accounts for both uneven damage and rotation of the plane of the guardrail.

Because the finite element simulations made use of under-integrated shell elements, it was desirable to prove that the results were comparable to the more accurate but expensive fully integrated shells. The models with 70, 80, and 90mm were run with the element formulation of the rails set to fully integrated shells, and the results were compared to the original results. These test conditions were chosen due to the significant visibility of hourglassing in these simulations, representing as much as 50% of the total energy in the simulation. There were no significant differences observed with regards to the rails post-deformation measurements. Therefore, all of the results presented in this paper are from the faster reduced shells.

Unlike the rail flattening, the energy absorbed in the rail appeared to follow a roughly exponential fit at all times. Figure 138 shows the energy absorbed by the rail for each displacement condition. All of the data points shown are from models using the faster, reduced integration shells. The exponential nature of the curve would lend support to the belief that slightly deformed guardrail may still retain enough of its functionality to remain in service.

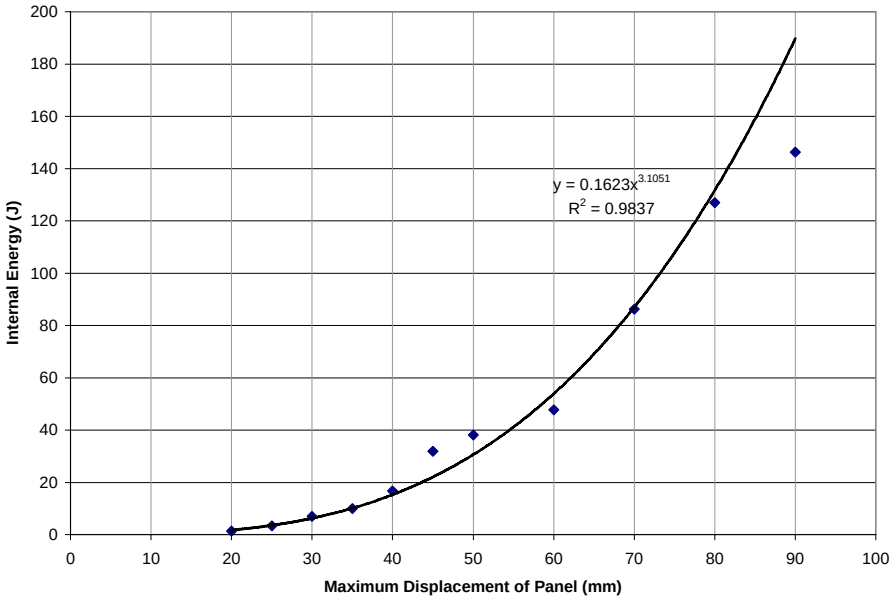

Figure 138: Internal energy of the rail as a function of the controlled displacement

The total energy absorbed by the rail in this simulation is not related to the capacity of true guardrail to absorb energy, so no conclusions should be made related to this value. In particular, it was noted that the absorption of energy through deformation was very strongly influenced by the shell formulation employed in the model. Using a fully integrated formulation resulted in 3-4 times the amount of energy absorbed. Additionally, the controlled displacement conditions used to load the guardrail are not as useful in the measurement of energy absorption.

Since the rail is question is increasing in length, it was desirable to examine how much of the height increase was due to flattening and how much was due to stretching effects. Selected finite element models were re-run to generate information on the thickness of the shell elements during the deformation. It was found that the elements thinned by less than 0.03 mm from their original thickness of 2.67 mm, which is only a 1% loss in the thickness. Additionally, the length of deformed rail contour was measured and did not show any significant changes in total length for any test conditions. Stretching along the length of the guardrail was not measured, but any

stretching in this direction would not affect the height of the guardrail, and therefore would not have influenced the results of methods used in this paper.

One limitation of this analysis is that this method generates only a single value for the entire height of the rail. This approach does not differentiate between the symmetric deformation observed in the finite element experiments and the less symmetric damage in the field. The exponential nature of the curve in Figure 138 implies that the energy to fully flatten half of the rail is not the same amount of energy needed to flatten the whole rail by 50%. Additionally, there may be twisting and lengthwise stretching involved for some cases. However, there is no easy way to consider these effects without compromising the simplicity of the calculation.

Using the equations that were determined through the finite element analysis, it is possible to generate a table of values for in field use. This table, shown at the end of this paper in Table 46, allows for a quick conversion of rail height to approximate rail flattening. It may be useful for times when field measurements are necessary but there are no electronic devices nearby.

Conclusions

The goal of this study was to find a simple and reliable way to measure the percentage of flattening in the guardrail. This was accomplished by using finite element analysis to relate the change in the rail height to the loss of rail depth. The relationship was found to be linear for low deformations and exponential for higher deformations, with the change occurring when the rail height increases by approximately 25%. By splitting the curve into two pieces, it was possible to fit the curves with an R^2 value greater than 0.99.

There are some limitations of the approach detailed in this paper. These include an inability to account for localized damage, as well as the energy absorbed in twisting of the guardrail. The effects of stretching were examined and were found to be insignificant. However, attempting to account for localized damage would compromise the simplicity of estimating the rail flattening.

References

1. AASHTO-AGC-ARTBA Joint Committee, "A Guide to Standardized Highway Barrier Hardware," http://aashtotf13.tamu.edu/index.htm Accessed: 6/12/07
2. LSTC, "LS-DYNA Keyword User's Manual: Version 970," Livermore Software Technology Corporation, April 2003.

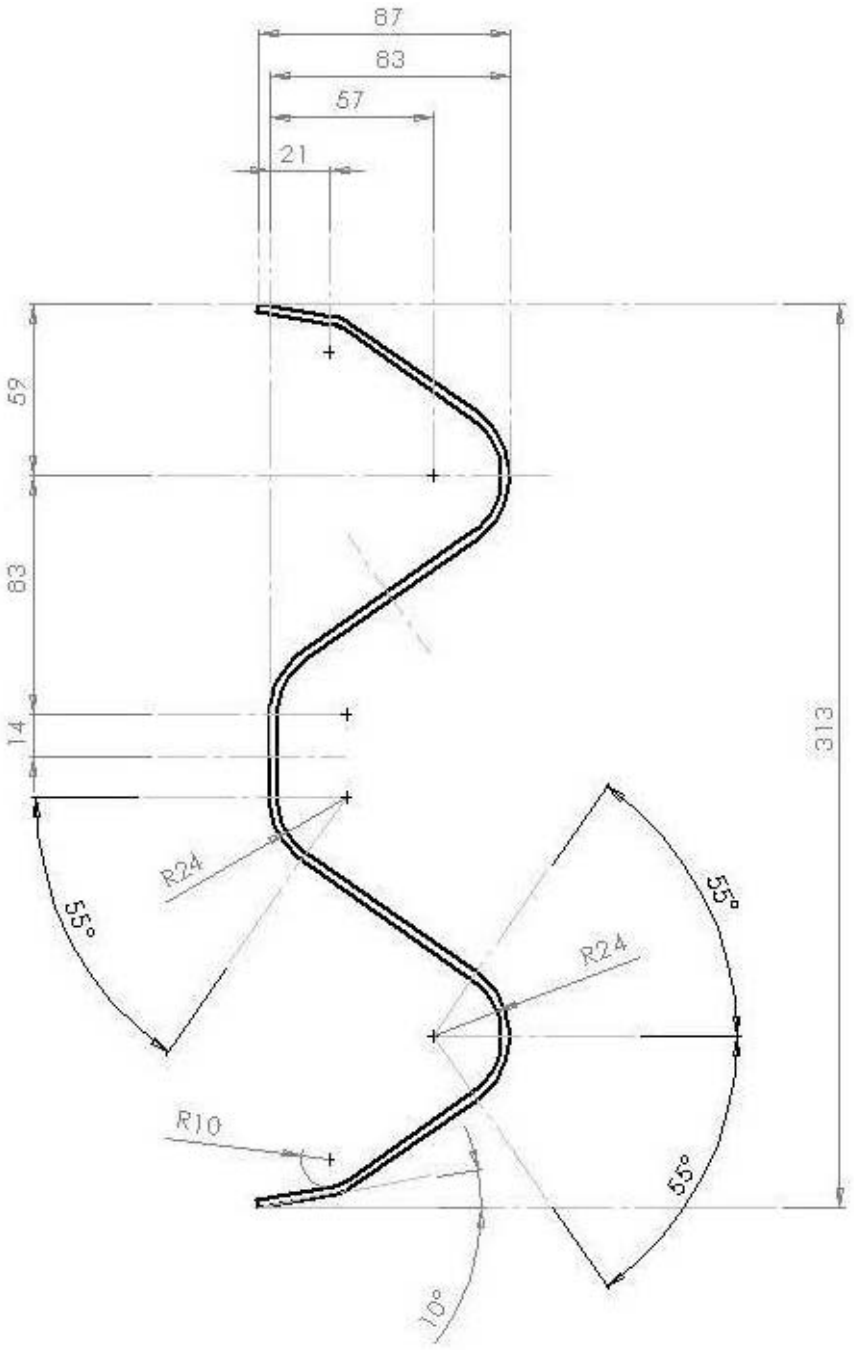

Figure 139: Dimensions of a W-beam guardrail. Dimensions are shown in both English and metric units. Thickness is 2.67 mm. Drawing from AASHTO-AGC-ARTBA.

Table 46: W-beam rail – height flattening resource

Rail Height (mm)	Predicted Flattening (%)	
322	0.1%	
327	1.5%	
332	2.9%	
337	4.3%	
342	5.7%	
347	7.2%	
352	8.6%	
357	10.0%	
362	11.4%	
367	12.8%	
372	14.2%	
377	15.7%	
382	17.1%	
387	18.5%	
392	19.9%	
397	21.3%	21.2%
400	22.2%	22.1%
402	22.7%	22.8%
407		24.5%
412		26.3%
417		28.3%
422		30.4%
427		32.7%
432		35.1%
437		37.7%
442		40.5%
447		43.6%
452		46.8%
457		50.3%
462		54.0%
467		58.1%
472		62.4%
477		67.1%
482		72.1%
487		77.4%
492		83.2%
497		89.4%
502		96.1%